New Phenomenology from Asymmetric Dark Matter

Robert Lasenby

Merton College

University of Oxford

A thesis submitted for the degree of

Doctor of Philosophy

Hilary Term 2015

New Phenomenology from Asymmetric Dark Matter

Robert Lasenby, Merton College, University of Oxford

A thesis submitted for the degree of Doctor of Philosophy, Hilary Term 2015

Abstract

The properties of dark matter — its microphysical form, and its cosmological origin and history — are one of the most important mysteries in fundamental physics. So far, evidence for matter beyond the Standard Model comes entirely from gravitational effects. However, other experiments are reaching the point where the 'simplest' models of dark matter are coming into tension with data, and may be strongly constrained by medium-term observations. This, along with theoretical considerations, motivates the exploration of other possibilities for the history and composition of dark matter, especially those with the possibility of new, generic observational signatures. In this thesis, we explore some different classes of new dark matter models, focussing on regimes in which they may display approximately model-independent phenomenology.

Firstly, we look at a class of dark matter models featuring large-number, stable composite states, and investigate how these may be synthesised in the early universe. As the example of Standard Model nuclear physics and Big Bang Nucleosynthesis demonstrates, the properties of small-number composite states in strongly-coupled theories may be complicated, and sensitive to the precise details of the theory. However, it may reasonably be expected that the properties of large enough composite states will obey simple geometrical scaling laws. In this case, if large enough states are synthesised in the early universe, the overall results of the synthesis process may become broadly independent of the detailed parameters of the model, and of initial conditions. We model 'dark nucleosynthesis' in such a regime, and find that the late-time number distribution takes on one of two characteristic forms, in both cases with weak dependence on small-number initial conditions and behaviour.

Following on from this, we consider the scattering phenomenology that would result from dark matter being made up of such large composite states. This includes the coherent enhancement of scattering rates — for example, at direct detection experiments — compared to e.g. collider production processes. The spatially extended nature of composite dark matter states could also lead to characteristic momentum-dependent form factors in scattering processes, which may be identifiable in direct detection experiments. In addition, inelastic interactions between dark matter states may be important in astrophysical settings.

Illustrating the effects of dark-sector energy injections, we present calculations for dark matter halo modifications through velocity kicks. As an example application, we discuss a different class of asymmetric dark matter models, in which late-time decays of part of the dark matter can re-populate a symmetric component, giving annihilation signals in galactic halos. The velocity kicks arising from the decay process may modify the spatial profile of such signals, to the extent to eliminating them almost completely from low-escape-velocity systems such as dwarf galaxies.

Acknowledgements

I am very grateful to my DPhil supervisor, John March-Russell, for his help and advice over the past four years. His breadth of knowledge and enthusiasm, within physics and beyond, have been a great resource and an inspiration.

In addition, I would like to thank my other co-authors — Edward Hardy, Stephen West, and James Unwin — along with the many people at Oxford and elsewhere who I have had the privilege of learning from.

I gratefully acknowledge financial support from an STFC studentship, and from the Buckee Scholarship at Merton College. Thanks also go to the CERN theory group, the Stanford Institute for Theoretical Physics, and the Perimeter Institute for Theoretical Physics for hospitality, and to the organisers and participants of the Cargèse 2014 Summer School.

Special thanks are reserved for my parents, whose support and advice have been consistent and much-appreciated.

Statement of Originality

This thesis is based on original research as described below, and contains no material that has been accepted or is currently being submitted for any degree, diploma or certificate or other qualification at the University of Oxford or elsewhere.

Chapter 1 contains a brief overview of aspects of Dark Matter theory, and was prepared solely for this thesis.

Chapter 2 is based on `arXiv:1411.3739` (manuscript submitted to *JHEP*), work done in collaboration with Edward Hardy, John March-Russell, and Stephen West. Chapter 3 is based on a manuscript being prepared for submission to *JHEP*, in collaboration with Edward Hardy, John March-Russell, and Stephen West. Chapter 4 is based on *JHEP* 1407 (2014) 049, work done in collaboration with Edward Hardy and James Unwin. For each of these papers, I originated many of the ideas, performed the majority of the writing, and wrote the code used to obtain numerical results.

Contents

1 Dark Matter — a brief overview 1

1.1 Evidence for dark matter 2
1.1.1 Dynamics of galaxies and clusters 2
1.1.2 Gravitational lensing 3
1.1.3 History and evolution of the universe 4
1.1.4 Properties of dark matter 6
1.1.5 Problems with Λ-CDM cosmology 12
1.2 Dark matter models 14
1.2.1 Dark matter stability 14
1.2.2 Dark matter production 17
1.2.3 Thermal dark matter, asymmetric dark matter, and baryogenesis 18
1.3 Thesis outline 22

2 Big Bang Synthesis of Nuclear Dark Matter 24

2.1 Basics of dark nucleosynthesis 28
2.1.1 Freeze-out of fusions 29
2.1.2 Bottlenecks, and comparison to BBN 32
2.2 Aggregation process 33
2.2.1 Scaling regime 35
2.2.2 (In-)Dependence on initial conditions 37
2.2.3 Real-time behaviour 39
2.2.4 Bottlenecked regime 41
2.3 Aspects of dark sector phenomenology 45
2.3.1 Post-nucleosynthesis energetics in the dark sector 46
2.3.2 Light dark sector states 49
2.4 Summary 51

3 Signatures of Large Composite Dark Matter States 53

3.1 Modifications to elastic scattering and direct detection 55
3.1.1 Dark sector form factors 55
3.1.2 Direct detection recap 57
3.1.3 Coherent enhancement of scattering rates 59
3.1.4 Recoil spectrum from size distribution 61
3.1.5 Dependence on DM velocity distribution 62
3.1.6 Detectability of a rising energy recoil spectrum 64
3.2 Low-energy excitations & inelastic scattering 66

3.2.1 Properties of low-energy excitations 66
3.2.2 Inelastic scattering form factors 69
3.2.3 Inelastic recoil spectra 70
3.3 Astrophysical capture 72
3.3.1 Self-interactions of captured dark matter 74
3.3.1.1 Dissipative collisions 75
3.3.1.2 Fusions 77
3.4 Summary 78

4 Dark matter distributions after velocity kicks & decaying ADM 80
4.1 Effect of velocity kick on DM distribution 81
4.2 Annihilation signals from ADM 84
4.2.1 Regeneration of symmetric component from models with two dark asymmetric species 87
4.2.2 General constraints and signals 90
4.2.3 B'-L' mass splitting and $\overline{L'}$ distribution 93
4.2.4 Direct and indirect detection 96
4.2.5 Annihilation via $L'\overline{L'} \to VV$ 99
4.2.6 Annihilation via $L'\overline{L'} \to \phi \to$ SM 101
4.2.7 Tentative signals and morphology 102
4.3 Summary 105

5 Conclusions 107

A Appendices 115
A.1 Transition from equilibrium to aggregation 115
A.2 Matrix elements for inelastic scattering 117
A.3 High-momentum scattering from large composite states 119
A.3.1 Coherent scattering 119
A.3.2 Incoherent scattering 120
A.4 Statistical identification of rising distributions 121
A.5 Solar capture of heavy WIMPS 124
A.6 Effect of approximations to DM halo distributions 125
A.7 Rates of B' and L' violating processes 127
A.8 B'-L' mass splitting and $\overline{L'}$ injection velocity 130
A.9 Model-building the B',L' splitting 132

Bibliography 136

CHAPTER 1

Dark Matter — a brief overview

The Standard Model (SM) of particle physics is an amazingly successful theory. Since its construction 40 years ago, its predictions have been verified to ever greater accuracy by successive generations of experiments, culminating with the discovery of the Higgs boson, the final until-then unobserved SM state, at the LHC in 2012. At the present time, no significant deviations have been observed between SM predictions and laboratory experiments (where such predictions can be reliably calculated), and it is theoretically plausible that its predictions will continue to hold up to energy scales orders of magnitude higher than can currently be probed.

Despite all this, we know that the SM cannot be a full description of Nature. Part of this is that the theory itself is incomplete — it predicts its own breakdown at scales where gravity becomes as strong as the other forces (around the Planck scale), and needs to be extended to an as-yet-unrealised theory of quantum gravity in that regime. This length scale is enormously smaller than those we have access to experimentally, and new effects from an eventual theory of quantum gravity are only expected to be relevant in very extreme regimes.

However, there are also more direct observational reasons why the SM must be incomplete. In trying to construct a consistent cosmological model that accounts for the behaviour and evolution of the universe, it turns out that attempts to do this using only the particles and fields present in the SM fail. The most clearcut problem is that of ‘Dark Matter’ (DM). As discussed in this Chapter, this refers to a set of observations that cannot be explained within the SM, but do fit together neatly (with some caveats, discussed in Sections 1.1.4 and 1.1.5) under the assumption that there is some extra non-SM matter in the universe, whose gravitational effects are being observed.[1]

This Chapter gives a very brief overview of the evidence for dark matter, and the constraints that can be placed upon its properties. There are many reviews treating these topics in more depth. A comprehensive and reasonably recent review of dark matter is [1]. For an overview of modern cosmology, good textbooks include [2] and [3], while Daniel Baumann’s Cambridge Part III course notes [4] are an excellent shorter account. This Chapter assumes a knowledge of the standard cosmological history described in these references. One semantic point is that, in accordance with usual cosmological terminology, we use ‘baryonic matter’ to refer to both SM baryons and leptons.

1.1 Evidence for dark matter

1.1.1 Dynamics of galaxies and clusters

Historically, the first robust evidence for dark matter came from comparing the rotation curves (orbital velocity versus radius) of galaxies with their distributions of luminous matter.[2] In Newtonian gravity, the velocity of a circular orbit in a spherically symmetric system is $v(r) = \sqrt{GM(r)/r}$, where $M(r)$ is the mass contained within a radius r. Observed galactic rotation curves have $v(r)$ approximately constant beyond a certain radius, implying a mass distribution with $\rho \sim 1/r^2$, whereas the distribution of luminous matter drops off much more steeply

---

[1] There are also other cosmological ‘problems’, including the homogeneity and isotropy of the universe (up to small perturbations on large scales), cosmic acceleration, and baryon asymmetry. These are not disallowed within the SM, but are certainly unexplained, requiring unexpected, surprising tunings of parameters or initial conditions.

[2] Earlier measurements, including Zwicky’s observations of clusters, were interpreted as being due to dark matter, but are claimed to have been dominated by systematic errors [5].

than this. While the real-world situation is clearly more complicated than these simplistic assumptions of circular orbits and spherical symmetry, the same basic conclusions are found to hold — the velocity distributions of stars in galaxies can only be accounted for under the assumption that the galaxy is embedded in a roughly-spherical halo of non-luminous matter, with density falling roughly as $1/r^2$ [6].

As well as this evidence from the orbital velocities near the edges of galaxies, analysis of other motions on galactic scales also shows a need for extra non-luminous matter:

- Analysing the velocity dispersions of stars in dwarf galaxies shows that, unlike many larger galaxies (where stellar motions near the centre are reasonably well accounted for by the gravitational influence of luminous matter), the gravitational potential must be dominantly due to non-luminous matter [7, 8].

- The velocity dispersion of dwarf galaxies around their host galaxies requires a large DM contribution [9], as does the velocity dispersion of galaxies orbiting in clusters [10].

- The baryonic mass of galaxy clusters is dominated by hot gas, which we observe through its X-ray emission. The inferred temperature is high enough that, in order for the gas to be gravitationally bound in the observed distribution, there must be a large DM contribution [11].

1.1.2 Gravitational lensing

A more direct way to infer the presence of gravitating mass is through its effect on light — the ‘gravitational lensing’ predicted by General Relativity. This is confirmed on Solar System and smaller scales by many experiments (see e.g. [12]), but on galactic and larger scales it suggests the existence of more matter than is observed through EM emission / absorption.

The most convincing evidence of this kind comes from systems such as the Bullet Cluster, a pair of galaxy clusters that recently underwent a head-on collision [13]. While the gas from each of the clusters shows clear signs of having been slowed by the collision, the mass density inferred from gravitational lensing shows two well-separated clumps, matching the location of the clusters' galaxies (which mostly pass through without colliding). This clearly-motivated separation between the luminous and gravitational densities is compelling evidence in favour of the dark matter picture, and against some kind of systematic error in describing the gravitational effects of luminous matter.

Less spectacularly, but still very usefully, lensing measurements of the mass in different systems can be compared to their luminous matter content. The lensing-based results generally agree [10] with those obtained from the velocity-based approaches described in the previous section, and so indicate the presence of much more matter than is visible.

1.1.3 History and evolution of the universe

While there is convincing evidence, from dynamics and from gravitational lensing, for more matter than can be accounted for by straightforward observations, there are a number of compact, relatively dark forms that Standard Model matter can take — black holes, neutron stars, brown dwarfs, rocks — which, under the collective name of MACHOs (Massive Astrophysical Compact Halo Objects), were seriously considered as a candidate for dark matter. However, in attempting to reconstruct the history and evolution of the universe, we find that the gravitational influence of more matter than is inferred to be present in SM states is again required, even in the very early universe. Unless very dense SM states somehow formed and persisted through the very hot thermal bath in the early universe (which might be possible in the case of e.g. black holes), these deviations require some new form of matter.

The earliest stage of the universe's history that we can accurately reconstruct is the epoch of Big Bang Nucleosynthesis (BBN). Calculations of the nucleosynthesis process, taking as input basically only the number density of baryons when the universe was at high temperatures ($\sim 1\,\mathrm{MeV}$), accurately predict the observationally-reconstructed primordial abundances of light elements [14, 15]. Since the universe was, in the standard cosmological model, radiation-dominated during this era, the gravitational influence of baryonic matter, and of today's quantity of dark matter, were not significant, so BBN does not constrain the influence of dark matter directly. However, it does pin down the early-time baryon density rather precisely.

The next epoch that provides significant information is the immediate pre-recombination era, when the photon-baryon fluid undergoes acoustic oscillations, the density fluctuations from which leave their imprint on the Cosmic Microwave Background (CMB). Since, unlike baryons, the hypothetical DM states are not strongly coupled to photons, they affect the expansion rate (as the universe is transitioning from radiation-dominated to matter-dominated around this time) without changing the properties of the plasma. Thus, it is possible to separate out the effects of dark matter and baryonic matter on the CMB fluctuations [16] — the most recent measurements, from the Planck satellite, determine the average densities (projected forwards to today) of dark matter and baryonic matter to be 0.26 and 0.05 respectively of the universe's critical density [17]. This density of baryonic matter agrees very well with the BBN value. The remaining 0.69 of the present-day energy density comes, in the standard cosmological model, from a vacuum energy density. This standard picture of the universe is referred to as 'Λ-CDM', after its two dominant components — the vacuum energy Λ, and the Cold Dark Matter ('cold' in that it must be moving slowly, as we discuss below).

The history of structure formation in the universe also requires dark matter for a viable explanation. In particular, it requires dark matter to be moving at sufficiently low velocities at early times. Being at low speeds, and not strongly coupled to photons, the DM can start gravitationally collapsing before recombination, providing 'seed' fluctuations for the baryonic matter to fall into. Without these seeds, the initial stages of structure formation would be much slower than observed — we would require significant perturbations to the baryon density beyond those associated with the radiation perturbations observed in the CMB, and these are are ruled out by the full set of CMB measurements.[3] Modelling the evolution of the universe (which requires large numerical simulations) it is found that, except for some issues (generally at sub-galactic scales) that we discuss in Section 1.1.5, the results predicted from starting with the CMB-derived proportions of CDM and baryons, with both having purely adiabatic perturbations, are in excellent statistical agreement with the observed structure of the universe (e.g. [18, 19]).

1.1.4 Properties of dark matter

As reviewed above, the combination of dynamical, lensing, and early universe evidence is well-explained by some form of non-SM matter, which is dark (weakly interacting with photons) and approximately non-collisional, with there being around 5 times as much of this matter as there is SM matter in total. Summarising the inferred properties of this hypothetical matter more quantitatively:

- As mentioned in the previous section, structure formation, as well as CMB constraints, require 'Cold Dark Matter' (CDM), i.e. for the dark matter to be at low velocities at early times. Constraints from observations of high-redshift structure, e.g. [20], mean that a thermal relic from the SM bath would need a mass $\gtrsim 4\,\mathrm{keV}$. Roughly, this corresponds to massive DM particles being non-relativistic ($v \lesssim 0.3c$) when the temperature is $T_{\mathrm{SM}} \sim 100\,\mathrm{eV}$ (note that this is a rough approximation, and that a non-thermal DM velocity distribution would affect the derived constraints to some degree).

- On sub-galactic scales, the clumpiness of the DM distribution is rather poorly

---

[3] In addition to determining the overall densities of CDM and SM matter, CMB data also constrains the fluctuations in their densities, with the 'isocurvature' perturbations in both — that is, the perturbations beyond the 'adiabatic' fluctuations that correspond with the photon perturbations visible as the primary CMB fluctuations themselves — inferred to be less than 10% of the amplitude of the adiabatic fluctuations [17].

constrained. Clumps of physical size comparable to or smaller than stars must have masses $\lesssim 2 \times 10^{-9} M_\odot = 2 \times 10^{48}\,\mathrm{GeV}$, as constrained by a combination of micro-lensing and stellar motion observations ([21] and references therein). At the other end of the scale, the wavelength of the DM states must be small enough to permit clustering on galactic scales. For bosonic states, this means that the wavelength must be smaller than the scales of dwarf galaxies, around 1 kpc, so $m \gtrsim 3 \times 10^{-22}\,\mathrm{eV}$. For fermionic states, degeneracy pressure would prevent dwarf-galaxy level DM densities for $m \lesssim 1\,\mathrm{keV}$ [22]. In particular, this rules out SM neutrinos, which have masses less than 1 eV, as the primary component of dark matter.

- The dark matter must, on astrophysical scales, be 'basically collisionless'. This statement does not mean that the states constituting the dark matter cannot have strong interactions among themselves — for example, stars in galaxies are basically collisionless (the average time between collisions between them is longer than the age of the universe), since the matter making them up is in a compact configuration, and the collisional cross section saturates to its geometric value. Additionally, the reason why SM gas collapses to form structures much more compact than DM halos is that is it able to dissipate energy through photons — *elastic* DM self-interactions would have a more subtle effect on halo structure.

  Different astrophysical systems give constraints on DM self-interaction cross sections over a range of collisional velocities. Observations of colliding galaxy clusters, such as the Bullet Cluster, give $\sigma/m \lesssim 1\,\mathrm{barn/\,GeV}$ for high relative velocities $v \sim 10^{-2}c$ [23, 24]. Galactic halos, with orbital velocities $\sim 10^{-3}c$, again give a constraint of the order of $\sigma/m \lesssim 1\,\mathrm{barn/\,GeV}$ (see e.g. [25]). At lower velocites, i.e. in dwarf galaxies, the uncertainty surrounding the exact DM density profiles means that much larger self-interaction cross sections, $\sigma/m \sim 80\,\mathrm{barn/\,GeV}$ for $v \lesssim 40\,\mathrm{km\,sec^{-1}}$, still seem to be viable, e.g. [26].

Note that these bounds only apply to those states which make up the bulk of the DM density — it is perfectly possible for a sub-component ($\lesssim 10\%$) of DM to have large, dissipative self-interactions, as explored in a number of models [27, 28].

- Couplings to SM states: these must be small enough for us not to have detected the astrophysical population of dark matter non-gravitationally, and also for it not to be produced in detectable quantities in SM collisions, either astrophysically or in collider experiments. The production constraints apply only to sufficiently light DM states, from LHC energies of a few hundred GeV downwards, but are often the most constraining for very light DM candidates.

There are an enormous array of constraints on the ways in which different DM candidates could couple to SM states. Here, we simply present a few examples, illustrating the form that specific such constraints may take — in Chapter 5, we will review more extensively the status of current experiments. Figure 1.1 shows the rough limits on the coupling of 'heavy' DM to SM nucleons (protons and neutrons) — since, for masses larger than a few GeV, these come from detecting the scatterings of astrophysical DM particles, the constraints are generally of the form $\sigma/m_{\rm DM} <$ const. due to the lower number density of higher-mass DM states. For comparison, the interaction cross section between SM nucleons is around $1\,\mathrm{barn} = 10^{-24}\,\mathrm{cm}^2$. As the figure illustrates, comparable DM-SM scattering cross sections are ruled out up to very high masses, $\sim 10^{17}\,\mathrm{GeV}$. While this makes fundamental particles that interact significantly with the SM (in particular, those with EM or colour charge) difficult to realise, it does not rule out 'strongly-interacting' states of much larger masses, such as small black holes (though such states are often constrained by other observations).

Illustrating the situation for lighter DM, Figure 1.2 shows the limits on light ($m < 1\,\mathrm{MeV}$) vector DM which kinetically mixes with the photon (a 'dark photon'). This is constrained by direct detection experiments, by astrophysical production mechanisms (here, by production in stars), and for masses lower than those plotted, by laboratory constraints on modifications to the Coulomb force law.

Experimentally, there are multiple ongoing efforts to probe new regions of parameter space, across an extremely wide range of potential DM signals. In Chapter 5, we review a few of the current and near-future experiments, in particular those extending Figure 1.1.

- The average mass density of dark matter, appropriately scaled to take the expansion of the universe into account, is inferred to be the same from early-universe and late-time measurements. Thus, in general, the states making up the dark matter must be stable over the lifetime of the universe. For example, only of order a percent of the DM could have decayed into (dark) radiation between recombination and the present day (see e.g. [29]). If the decay were to another DM state of almost the same mass, then the effect of the velocity kick given to the new state from the decay means that, for kicks greater than around $20\,\mathrm{km\,sec}^{-1}$, only a small proportion can have decayed during the lifetime of the universe (e.g. [30–32]). If the dark matter is meta-stable, and has some branching ratio to SM states (other than neutrinos), then its lifetime is generally constrained to be many orders of magnitude longer than the age of the universe.

The above list is by no means an exhaustive review of such constraints — reviews such as [21] and [33] provide more thorough accounts of general properties, while there are an enormous array of other observational constraints which apply to different specific DM candidates. For example, as we will discuss in Section 1.2.2, some models of dark matter predict an equal population of DM particles and anti-particles, which are able to collide and annihilate to SM states, and there are

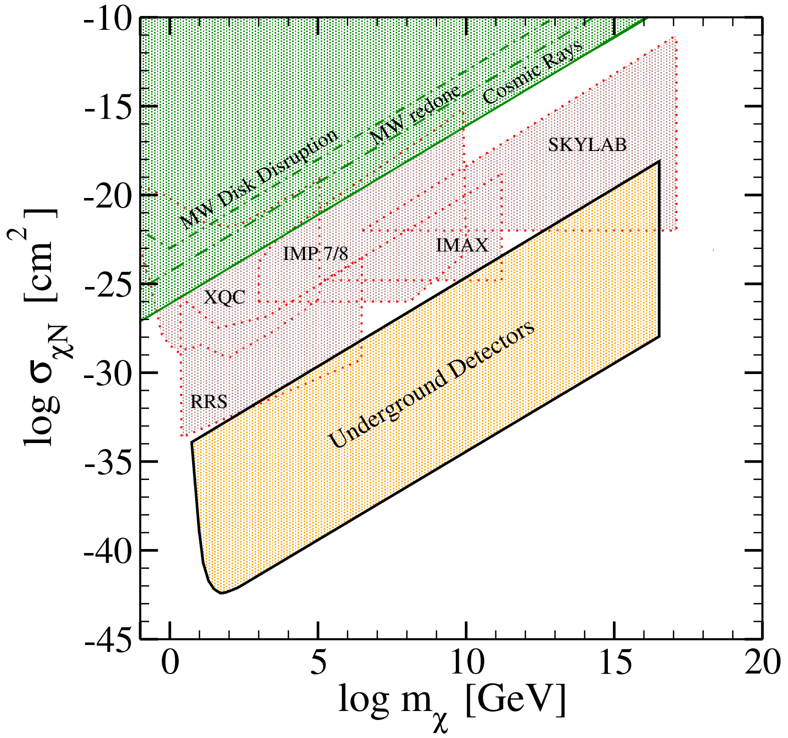

Figure 1.1: Excluded regions for $\sigma_{\chi N}$ (spin-independent dark matter scattering cross section with nucleons) vs m_χ (dark matter mass) — figure reproduced from [35]. The green shaded region is ruled out by astrophysical constraints [36–39], the red shaded regions by space-based detectors [36, 40–42], and the yellow shaded region by underground direct detection experiments [43–46]. The detector constraints assume a specific dark matter distribution at the Earth's location, given by the Standard Halo Model, and could vary up or down from those given (see e.g. Section 3.1.5).

cosmological/astrophysical constraints on this energy injection. We review some of those very briefly in Chapter 5.

One fairly robust consequence of the evidence reviewed so far is that dark matter cannot be composed of 'standard' SM states, in particular because of the too-small baryon abundance derived from BBN and CMB observations, and the fact that SM neutrinos are too light. However, it is still possible that SM objects compact enough to survive un-dissociated in the early universe, such as black holes or very large 'nuggets' of QCD matter, could be DM — [34] reviews some of the limits on these candidates.

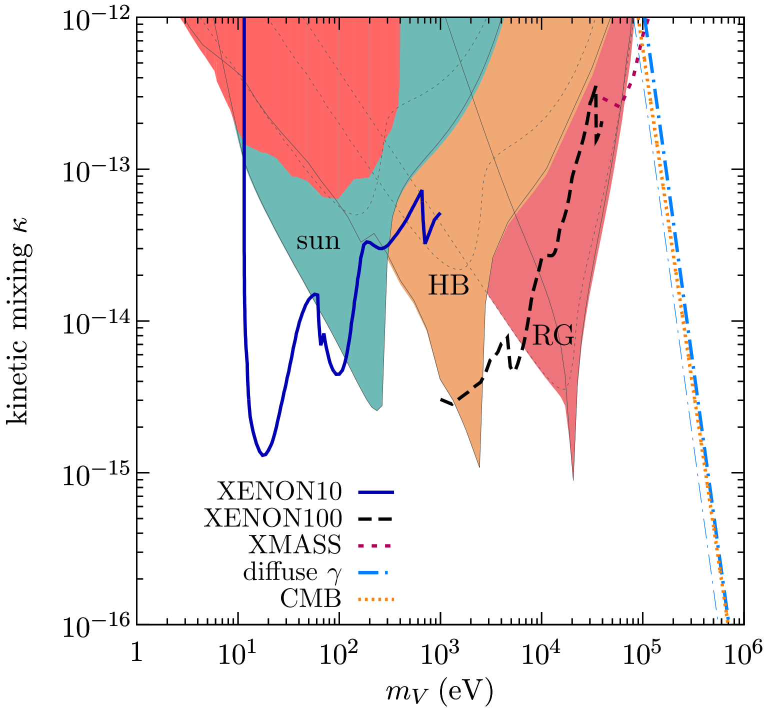

Figure 1.2: Excluded regions of kinetic mixing vs mass parameter space for dark photon DM — figure reproduced from [47]. Coloured regions labelled 'sun', 'HB', and 'RG' are constraints from energy loss in stars due to dark photon production (so do not depend on assumptions about the DM density). The blue solid and black dashed lines show constraints from direct detection experiments. See [47] for details of other plot elements.

1.1.5 Problems with Λ-CDM cosmology

As discussed above, the 'Λ-CDM' paradigm, in which cold dark matter makes up the majority of the universe's matter budget, makes predictions for structure formation that match observations of large-scale structure very well. However, on the scales of galaxies, and especially dwarf galaxies, there are currently some discrepancies between our best simulations of Λ-CDM consequences and observations. Since galaxies are also the first scale at which baryonic densities start competing with DM densities, it is not implausible that our present inability to perform linked simulations of DM and baryonic evolution is the cause of these problems. On the other hand, such discrepancies may persist even with better observations and simulations, which would indicate more strongly the need for further dark sector dynamics. For a more detailed review of these issues, see e.g. [48].

A category of the discrepancies come from the fact that Λ-CDM seems to predict more structure on sub-galactic scales than is actually observed. Simulations predict that the halo of the Milky Way, and similar galaxies, should contain a large number of high-DM-density sub-halos. While some proportion of these will be entirely dark (containing no stars), simple estimates of the expected stellar content seem to suggest that we should see more and larger dwarf galaxies than we do [49]. This picture is made slightly muddier by the recent discovery of multiple, extremely faint dwarf galaxies in the Milky Way halo [50], but there still seem to be problems, particularly with regard to the absence of the very large dwarf galaxies predicted [51].

Additionally, simulations show a universal 'cuspy' form for DM halos, in which the density increases steeply towards the centre [52]. Observations of dark matter dominated galaxies appear to suggest that DM density distributions are instead 'cored' (that is, with flatter centres), though the status of these observations is still somewhat unclear [53].

In all of these cases, approximate calculations indicate that DM with self-interaction cross sections slightly below the bounds mentioned in Section 1.1.4 could smooth out DM substructure on small scales, and possibly alleviate tensions between observation and theory. Also, as mentioned above, even the purely gravitational coupling between baryonic matter and dark matter could be important, and indeed recent work (see e.g. [54]) suggests that the kind of dynamic gas outflows observed in galaxies may be sufficient to explain the discrepancies with CDM-only simulations. Detailed observations of baryon-poor systems, such as dwarf galaxies, are potentially capable of distinguishing between these possibilities, since some of these systems do not have sufficient baryonic matter to plausibly modify their DM distribution [54].

Beyond the above issues, there is a catalogue of other observations that do not correspond well with the predictions of CDM-only simulations ([55] provides an overview). In particular, some of these take the form of simple relationships between the DM and baryonic densities, such as the 'Tully-Fisher relation' [56] — a power-law relationship between the total baryonic mass of galaxies and their (presumably dark-matter-dominated) outer rotational velocities, that appears to hold with little scatter over multiple decades in galactic mass. While such problems may plausibly be due to effects of baryonic feedback on the DM distribution [55], it is interesting that these relationships, as well as almost all of the galactic-scale evidence for dark matter (disregarding structure formation), appear to be well-fit by simple phenomenological modifications to the gravitational effect of baryonic matter. This observation has been developed into the MOND (MOdified Newtonian Dynamics) hypothesis, which posits that there is no dark matter at all, but rather that the theory of gravity needs to be modified when dealing with small accelerations [57]. Turning this into a fully consistent theory encounters many difficulties — in particular, accounting for lensing observations (where gravitating mass does not track baryonic mass) and early-universe cosmology. Modern attempts tend to accept the need for invisible matter at least at the scale of clusters (see e.g. Chapter 6 of [58]). Despite this, the surprising success of what is basically a one-parameter model in fitting diverse galactic relationships is something for which there is, as yet, no satisfying explanation in the CDM picture.

1.2 Dark matter models

In the previous section, we gave an overview of the evidence for non-baryonic dark matter, and a basic summary of the properties that it must have. In this section, we work under the assumption that the dark matter is composed of states arising from some quantum field theory extending the Standard Model, and investigate the most basic features required from such models — that they have a very long-lived massive state, and that such a state is produced in the correct abundance in the early universe.

1.2.1 Dark matter stability

As discussed above, the states making up today's DM need to be stable over timescales of at least a few times the age of the universe, and if they decay to SM states other than neutrinos, for much longer than that. This generally requires some symmetry that restricts their couplings with lighter states that they could decay into. In the Standard Model, the cosmologically-stable states illustrate a number of ways in which this can be realised:

- Photons and gravitons are massless, so cannot decay.
- Electrons/positrons are the lightest particles carrying charge under the unbroken $U(1)_{EM}$ gauge symmetry.
- The lightest neutrino mass eigenstate is the lightest fermion (where fermion parity is conserved since only fermions can carry half-integer angular momentum).
- The heavier neutrino mass eigenstates can decay into the lighter ones, but only via electroweak interactions, which introduces a suppression by the W, Z

mass scale. Since the mass of the heavier neutrinos is still very small (below 1 eV), the suppression $\sim \left(\frac{m_\nu}{m_W}\right)^4$ is enough to make their lifetimes far longer than the age of the universe.

- The proton is the lightest state carrying baryon number (and generally, the most stable nucleus of nucleon number A is the lightest state carrying baryon number A). Due to the gauge symmetry structure of the SM Lagrangian, terms that violate baryon number must be dimension-6 or higher, so the rate for proton decay will be suppressed by a high power of the inverse mass scale of the new physics responsible for these terms.[4] There are also non-perturbative electroweak field configurations (sphalerons) which violate baryon number, but the rate for these is exponentially suppressed at low temperatures [60].

For massive states, absolute stability is enforced by charge conservation in an unbroken gauge theory (or by fermion parity). However, unbroken phases of new gauge theories introduce new massless gauge bosons, which are often strongly constrained by observations, and we usually do not want the DM to be electromagnetically charged.[5] An alternative way to realise absolute stability is to be in the broken phase of a gauge theory, where this breaking preserves a discrete subgroup of the gauge group. Even in the low-energy theory, once the massive gauge bosons have been integrated out, the resulting *discrete gauge symmetries* are exact, and states can have exactly conserved charges under them [61].

The metastable but long-lived SM states arise because the symmetry structure of the theory means that the only possible decays are those which occur through higher-dimensional operators, and so are suppressed by the inverse mass scale of the new states involved ('accidental symmetries'). For heavy DM states, stability on cosmological timescales generally requires a very high scale for the new physics

---

[4] The sensitivity of terrestrial proton-decay experiments is such that naive Grand Unified Theory (GUT) models, which have the scale of new physics as $\Lambda \simeq 10^{16}$ GeV, are in some tension with the lack of any observed decays [59].

[5] Models in which DM carries small fractional EM charge have been proposed ('milli-charged DM'), though this charge must be extremely small to avoid astrophysical constraints.

involved.

Taking the examples of some popular dark matter candidates,

- SUSY particles with R-parity conservation: in supersymmetric extensions of the SM, the R-parity of each state is defined by $P_R = (-1)^{3(B-L)+2s}$, where s is the spin of the state, and B, L are the baryon and lepton numbers [62]. This makes all of the SM states R-even, and their superpartners R-odd. If R-parity is conserved (as is often helpful in evading proton-decay constraints), then the lightest R-odd state will naturally be stable. A standard technique to impose this is the idea of discrete gauge symmetries introduced above — e.g. if $U(1)_{B-L}$ is a gauge symmetry, broken down to a Z_2 discrete subgroup, then R-parity is exactly conserved [63].

- Axion-like particles: these are scalar/pseudo-scalar particles for which an approximate shift symmetry forbids a mass term, and forbids renormalisable couplings to SM states. As a result, they are naturally light, and have couplings suppressed by powers of some symmetry breaking scale, resulting in very long decay times. Such states may arise in field theory as the pseudo-Nambu-Goldstone bosons of a spontaneously broken symmetry at high scales. In string theories, there may be shift symmetries of the appropriate kind which are only broken by extremely small non-perturbative effects [64].

- Light dark photons: a 'dark photon' is a massive vector that kinetically mixes with the SM photon. If it has mass less than twice that of the electron, then it can only decay to photons or neutrinos, and the couplings of these to photons involve loops of heavier particles.

For meta-stable, rather than exactly stable, DM states, cosmologically long lifetimes also require that the state is light (at the very least, light compared to the Planck scale). Obtaining this without tuning is another challenge that also generally involves symmetries of the theory.

1.2.2 Dark matter production

As well as being stable over the lifetime of the universe, dark matter must be present, in the correct abundance, from shortly after BBN onwards. Given our limited knowledge of cosmological history before BBN, considerations about the origin of dark matter are necessarily rather uncertain. However, a reasonable expectation is that there were at least 50 e-folds of inflation, followed at some point by a radiation-dominated era, which cooled down with expansion until entering the usual Big Bang thermal history at BBN times.

Fitting dark matter into this story, one key question is whether it was ever in chemical equilibrium with other states. If it was at some point in chemical equilibrium with a bath of lighter states, then freeze-out from equilibrium at a temperature greater than its mass would leave the DM with a radiation-level abundance, which as per previous sections is generally not cosmologically viable. Freeze-out from equilibrium at a temperature lower than its mass would leave it with a Boltzmann-suppressed abundance, with its chemical potential (e.g. arising from a non-zero value of some conserved quantity) imposing a floor. If the dark state has a mass less than a few keV, then the temperature of the bath from which it freezes out much be much lower than the temperature of the SM bath, since otherwise the dark matter will not be cold. We go over these 'thermal freeze-out' scenarios in more detail in Section 1.2.3.

Alternatively, the dark matter may never have been in equilibrium with a thermal bath of lighter states — in particular, this is a way to realise very light, but still cold, dark matter. Inflation means that any 'initial' abundance would have been diluted to insignificance, so an abundance, with *adiabatic* density perturbations on comoving scales corresponding to CMB measurements, needs to be generated. This could occur in a number of ways, including decays of heavier states, sub-equilibrium couplings to other thermal baths (see e.g. [65]), or coherent production processes (inflaton decay, gravitational production, etc.).

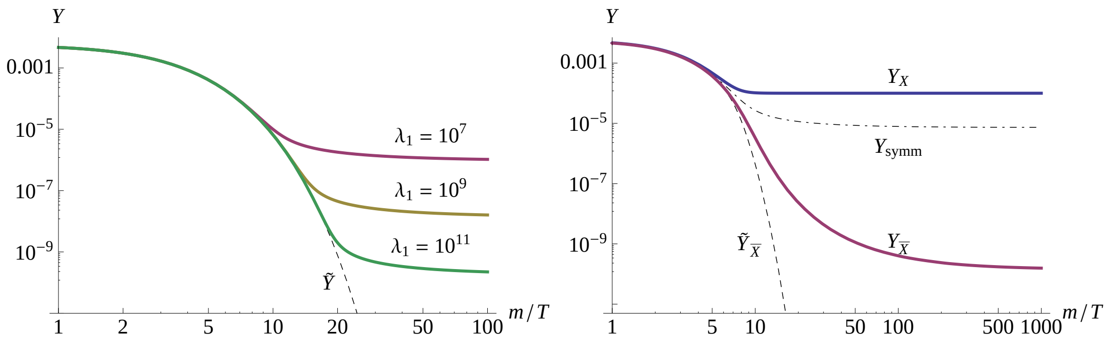

Figure 1.3: *Left:* plot of yield vs scale factor (during radiation domination, so $a \propto 1/T$) for a DM particle with mass m and thermally averaged annihilation cross section $\langle \sigma v \rangle$ (taken to be constant), where $\lambda_1 \equiv \langle \sigma v \rangle s/H$ evaluated at $T = m$. The dashed curve labelled $\tilde{Y}$ shows the equilibrium abundance. The DM abundance is taken to be symmetric, so the yields displayed are solutions of equation 1.2. Note that the eventual abundance is approximately $\propto 1/\lambda_1$, and that the temperature of departure from the equlibrium curve ('freeze-out') depends weakly on λ_1. *Right:* as for the left-hand plot, but where the DM has an asymmetry, so $Y_X - Y_{\overline{X}} = \Delta Y$ is constant and non-zero, and we are solving equation 1.8. Here, we take $\Delta Y = 10^{-4}$, and $\lambda_1 = 10^6$. The dashed curve labelled $\tilde{Y}_{\overline{X}}$ shows the equilibrium abundance of $\overline{X}$ (Y_X tracks the equilibrium abundance of X very closely). The dot-dashed curve shows the symmetric freeze-out solution for $\lambda_1 = 10^6$, for comparison.

1.2.3 Thermal dark matter, asymmetric dark matter, and baryogenesis

Figure 1.3 provides a visual overview of the thermal freeze-out scenario outlined above. Analysing this quantitatively, starting with the symmetric (zero chemical potential) case, the number of X particles in a given co-moving volume V obeys the Boltzmann equation

$$\frac{d(n_X V)}{dt} = -\langle \sigma v \rangle n_X n_{\overline{X}} V + \gamma_{X\overline{X}} V = \langle \sigma v \rangle (\tilde{n}_X^2 - n_X^2) V \ , \tag{1.1}$$

where $\langle \sigma v \rangle$ is the (kinetically averaged) annihilation cross section for $X\overline{X} \to$ (bath states) processes, and $\gamma_{X\overline{X}}$ is the production rate per unit volume for $X\overline{X}$ pairs from the thermal bath. By detailed balance, $\gamma_{X\overline{X}} = \langle \sigma v \rangle \tilde{n}_X \tilde{n}_{\overline{X}}$, where $\tilde{n}_X$ is the equilibrium number density of X. We have also assumed that $n_X = n_{\overline{X}}$, which will be a good approximation so long as we are in the ballistic rather than diffusive regime (i.e. mean free paths are longer than the characteristic X,$\overline{X}$

separation). We can simplify this by replacing the number densities with a quantity that is constant if co-moving number is conserved — assuming co-moving entropy conservation, we can use the yields $Y_X(t) = n_X(t)/s(t)$, where $s(t)$ is the entropy density of the thermal bath. This gives

$$\frac{dY_X}{dt} = \langle \sigma v \rangle s(t)(\tilde{Y}_X^2 - Y_X^2) \quad \Rightarrow \quad \frac{dY_X}{d\log a} = \lambda(\tilde{Y}_X^2 - Y_X^2) \ , \tag{1.2}$$

where $\lambda \equiv \langle \sigma v \rangle s/H$ (effectively, the interaction rate per Hubble time for a radiation-like abundance with cross section $\langle \sigma v \rangle$). If we assume a form for $H(t)$, then this equation can be solved numerically, giving solutions of the form shown in Figure 1.3. We can understand the basic behaviour analytically [2]. Once 'freeze-out' has occurred, i.e. the annihilation rate is no longer sufficient to keep Y_X close to $\tilde{Y}_X$, the equation becomes $\frac{dY_X}{d\log a} \simeq -\lambda Y_X^2$, so $\frac{1}{Y_f} - \frac{1}{Y_\infty} \simeq \int d\log a \, \lambda = -\lambda_f$, where we have assumed that we are radiation-dominated, so $H \propto 1/a^2$ and $\lambda \propto 1/a$, and that the averaged annihilation cross section is constant with temperature (as for e.g. s-wave annihilations). Assuming that $Y_\infty \ll Y_f$, this implies that $Y_\infty \simeq \lambda_f^{-1}$.

Turning to when freeze-out occurs, if we write $Y_X = \tilde{Y}_X(1+\delta)$, then to first order in δ we have

$$\delta' = -\left(2\tilde{Y}_X\lambda + (\log \tilde{Y}_X)'\right)\delta - (\log \tilde{Y}_X)' \ , \tag{1.3}$$

where primes indicate differentiation with respect to $\log a$. Since, in the non-relativistic regime, $\tilde{n}_X(T) = g_X \left(\frac{m_X T}{2\pi}\right)^{3/2} e^{-m_X/T}$, and $T \propto 1/a$, we have $(\log \tilde{Y}_X)' = -\frac{m_X}{T}$ + logarithmic corrections. So, when $\tilde{Y}_X\lambda \gg m_X/T$, departures from equilibrium are quickly corrected. Once $\tilde{Y}_X\lambda$ goes below m_X/T, such departures grow, and we have frozen out. The abundance at the freeze-out time will be roughly $Y_f \sim \tilde{Y}_f \sim \frac{m_X}{T}\lambda_f^{-1}$, so if we do freeze out with a Boltzmann-suppressed abundance, then the condition at the end of the last paragraph does hold, justifying $Y_\infty \simeq \lambda_f^{-1}$. Additionally, since $\tilde{Y}_X$ goes like $e^{-m_X/T}$, the value of $x \equiv m_X/T$ at which freeze-out occurs will depend only approximately logarithmically on the value λ_1 of λ at $x = 1$, so for $\lambda \propto 1/a$ we can write the relic abundance as

$$Y_\infty \simeq \frac{x_f}{\lambda_1} = \left.\frac{x_f H}{\langle \sigma v \rangle s}\right|_{T=m_X} , \tag{1.4}$$

where x_f is around 20 for reasonable parameters.

Going from yields to present-day energy densities, the present-day relic density is

$$\Omega_X = \frac{\rho_{X,0}}{\rho_c} = \frac{8\pi m_X Y_X s}{3 M_P^2 H_0^2} = 2.8 \times 10^{10} h^{-2} Y_X \frac{m_X}{100\,\mathrm{GeV}} \tag{1.5}$$

where ρ_c is the present-day critical density, M_P is the Planck Mass, and $H_0 \equiv 100h\,\mathrm{km\,sec^{-1}\ Mpc^{-1}}$ is the present-day Hubble parameter. The last equality of equation 1.5 assumes that freeze-out was from the SM thermal bath, so we can use the present-day SM entropy density of $2.9 \times 10^3\,\mathrm{cm^{-3}}$, and that there has been no significant entropy injection between the freeze-out epoch and now. From equation 1.4, $Y_\infty \sim \frac{x_f}{\langle \sigma v \rangle M_P m_X}$, so to leading order the m_X dependence in equation 1.5 cancels. Assuming that freeze-out takes place from the SM bath at temperatures $\gtrsim$ GeV, one obtains the approximate value [1]

$$\Omega_X h^2 \simeq \frac{3 \times 10^{-27}\,\mathrm{cm^3\,sec^{-1}}}{\langle \sigma v \rangle} . \tag{1.6}$$

Looking at the characteristic annihilation cross section arising from weak interactions, $\langle \sigma v \rangle \sim \frac{G_F^2 m_X^2}{4\pi} \simeq 10^{-26}\,\mathrm{cm^3\,sec^{-1}} \left(\frac{m_X}{10\,\mathrm{GeV}}\right)^2$, this is of approximately the right order of magnitude to obtain the required $\Omega_{\mathrm{CDM}} h^2 \simeq 0.1$. Known as the 'WIMP miracle' (Weakly Interacting Massive Particle), this coincidence is the foundation of many models of weak-scale dark matter.

In the asymmetric case, we start with a similar Boltzmann equation,

$$\frac{dY_X}{d\log a} = \lambda(\tilde{Y}_X \tilde{Y}_{\overline{X}} - Y_X Y_{\overline{X}}) , \tag{1.7}$$

with the difference that we assume $Y_X - Y_{\overline{X}} \equiv \Delta Y$ to be non-zero. Since the thermal bath does not 'know about' the asymmetry, we have $\tilde{Y}_X \tilde{Y}_{\overline{X}} = \tilde{Y}_{symm}^2$. If

$\langle \sigma v \rangle$ is small enough that we freeze out with Y_X and $Y_{\overline{X}}$ both much larger than ΔY, then the situation is almost exactly as in the symmetric case. On the other hand, if we reach $Y_X \sim \Delta Y$ while still in equilibrium (assuming $\Delta Y > 0$), then (as illustrated in the right hand plot of Figure 1.3) the equation for $Y_{\overline{X}}$ becomes

$$\frac{dY_{\overline{X}}}{d \log a} \simeq \lambda \Delta Y (\tilde{Y}_{\overline{X}} - Y_{\overline{X}}) \ . \tag{1.8}$$

In particular, $Y_{\overline{X}}$ tracks $\tilde{Y}_{\overline{X}}$ until $\lambda \Delta Y \sim m/T$, and the relic abundance is then further exponentially suppressed by $e^{-\lambda_f \Delta Y} \sim e^{-m/T_f}$. This is the 'Asymmetric Dark Matter' (ADM) regime, in which the vast majority of the relic density is in X particles — there is also an intermediate regime in which freeze-out occurs before equilibrium, but subsequent annihilations are affected by the ΔY floor. For ADM, obtaining the correct relic density $\Omega_X h^2 = 2.8 \times 10^{10} \Delta Y \frac{m_X}{100\,\mathrm{GeV}}$ (as per equation 1.5) is a matter of generating the correct initial asymmetry ΔY, and having a sufficiently large annihilation cross section.

This kind of thermal history is also the most plausible scenario for SM matter (indeed, we have evidence from BBN for asymmetric electron freeze-out), and the issue of generating the correct asymmetry there — 'baryogenesis' — is still a mystery. Modelling the behaviour of the SM thermal bath at higher temperatures (> TeV), one finds that the CP violation in the theory is nowhere near sufficient to explain the observed relic abundance, even in the presence of hypothetical strongly out-of-equilibrium dynamics [66]. One of the hopes behind many ADM models is that there may be some dynamics that can explain both the SM and dark sector asymmetries. In particular, if the DM particles have similar masses to SM baryons, then asymmetries of similar magnitude would 'explain' the order-of-magnitude coincidence, $\Omega_{\mathrm{DM}} \simeq 5\Omega_{\mathrm{b}}$, between the baryonic and DM mass densities.

1.3 Thesis outline

Despite all experiments searching for non-gravitational evidence of DM having so far shown up blank, the sensitivity of modern observations, of several types, is starting to strongly constrain some of the simpler kinds of DM models. In particular, for DM that froze out from equilibrium with the SM thermal bath, as described in the previous section, there are good medium-term prospects of ruling out (or detecting!) almost all of the naive parameter space (this point is reviewed in more detail in Chapter 5). Given this situation, it is important to investigate ways in which more complex dark sector physics may alter observational signals, and particularly the relationship between different types of observations. In the subsequent Chapters, we study the phenomenology of some dark matter models which do that. Rather than discussing single, definite models, we attempt to identify motivated classes of theories in which there is broadly model-independent behaviour.

In Chapter 2, we investigate the early-universe physics of ADM models featuring large composite bound states, analogous to SM nuclei. Strong, attractive self-interactions within a dark sector may arise in a number of ways, notably through confining forces similar to SM QCD. While the detailed behaviour of such models is difficult to calculate, it is expected that, for broad regions in parameter space, there will be stable large-number composite states. Moreover, there are good reasons to expect that, for large enough sizes, the properties of these states will scale according to simple geometrical laws. Both of these statements are broadly true in the SM, and if they also hold in a dark sector, there is the possibility that these large composite states will be synthesised in the early universe, analogously to BBN. SM BBN is a rather complicated processes, dominated by the specifics of small-number nuclear behaviour. We investigate the alternative, more model-independent regime in which successful synthesis of large nuclei occurs, and the results of the synthesis process are governed by scaling laws, finding that the eventual number distribution takes one of two characteristic forms, broadly independent of initial conditions.

Chapter 3 follows on by considering some of the present-day consequences that would follow from dark matter consisting of large composite states of this kind. One of these is that the signals from direct detection experiments may be modified in fairly model-independent ways, which could potentially be detectable in near-future experiments. Also, the interactions responsible for compositeness will generally lead to significant self-interactions between DM states, and these may have interesting consequences in regions of high astrophysical DM density. In particular, we make estimates indicating that such interactions could lead to significant modifications of the distribution of DM captured within stars, which may have model-dependent effects on stellar properties.

In Chapter 4, we calculate the modifications to DM halo distributions that result from a very simple class of dark sector energy injections. These calculations are applied to a different class of ADM models than those considered in Chapters 2 and 3, in which decays regenerate a symmetric component that may lead to astrophysical signals. Chapter 5 concludes by reviewing the status of current and near-future experimental efforts to detect thermal dark matter, focussing on how they relate to simple thermal production scenarios, and discusses how the models of previous chapters can affect the interpretation of and relationships between such observations.

CHAPTER 2

Big Bang Synthesis of Nuclear Dark Matter

Most models of dark matter assume that it is made up of point-like particles, or at least can be treated as such in its interactions. However, this is not necessarily the case. In the Standard Model most of the SM-sector mass in the universe is in the form of composite states—atoms, containing nuclei, made up of nucleons, which are themselves made up of quarks and gluons. Particularly noteworthy is the remarkable richness of SM-sector nuclear and atomic physics resulting from just a few basic conservation laws, most importantly baryon-number and charge conservation, and a few relevant interactions, dominantly the short-range strong nuclear binding force and long-range electromagnetic interaction. The compositeness and variety of the states that result, atoms and nuclei, plays a vital role in many important physical processes in the history of the universe, for example, in galaxy formation and all of stellar physics. Given the ease with which bound states can arise, it is clearly important to consider the possibility that DM may exist in the form of composite states too.

This Chapter will investigate a particular class of composite DM models—those featuring cosmologically stable “dark nuclei” (DN) of large dark “nucleon” number (DNN). In particular we focus on the case where, similar to SM nuclei, there is a relatively short-range strong “nuclear” binding force with a hard core repulsion, and there is an approximately-conserved quantum number, DNN, analogous to baryon number. Unlike the SM where both protons and neutrons are relevant, for reasons of minimality and simplicity we will take there to be just one kind of stable dark nucleon (or more generally, the differences between different nucleon types to be unimportant). Importantly, we will in addition assume that *in the dark sector the analogue of the long-range electromagnetic interaction between protons is absent*, either because there is no massless "dark photon" or because the stable dark nucleon is uncharged.[1]

With these simple assumptions there exist a very broad range of stable DN states of varying DNN, and with a binding energy per dark nucleon that *saturates* at a finite value. This is similar to the SM where there are stable nuclei at multiple baryon numbers with approximately constant binding energy per nucleon, of roughly 8 MeV, over a range of nuclear sizes. Unlike the SM, however, there is no longer a Coulomb repulsion term, so that in the dark sector the binding energy per dark nucleon truly does saturate, at least until gravitational effects become important, and never turns over, unlike the iron maximum in the SM, so there are *stable DN up to very large DNN.* In terms of a simple liquid-drop like model, analogous to the semi-empirical mass formula in the SM, we take the binding energy per dark nucleon to behave asymptotically as

$$\frac{B_k}{k} = \alpha - \frac{\beta}{k^{1/3}}, \tag{2.1}$$

where $k \gg 1$ is the DNN, the volume energy term is α, and the surface tension term β. Roughly this set of assumptions was considered in [75], which investigated the possibility that they could result in the early-universe formation of large DN.[2]

---

[1] Models of composite DM previously considered in the literature include "WIMPonium" [67–69], "dark atoms" [70], and most similarly to our work, "Q-balls" [71, 72] (non-topological solitons of scalar fields). In addition the DM candidates in technicolor-like theories are often composite states [73, 74], though these typically have small "nucleon" number, and most importantly have constituents with SM charges, unlike the cases we consider in this work.

[2] Essentially this holds for SM nuclei if Coulomb repulsion is absent (see [75] for such a model), and also for many Q-ball models [71, 72, 76]. In the absence of short-range hard-core repulsion, one obtains, in the fermionic case, states such as those investigated in [77, 78]. These are supported by degeneracy pressure until their constituents become relativistic, at which point the form of the attractive interactions becomes important—they will generally not display the

While the small bound states of such a model may have highly variable properties,[3] analogous to the special properties of deuterium or helium-4, once the DN become large enough, their properties, beyond just their binding energy, equation 2.1, can obey simple scaling laws. Most importantly certain interaction cross sections scale geometrically in the large DNN limit, at least when suitably averaged over a range of DNN to eliminate "magic number" and resonant effects which are of subdominant importance to the physics we study.

The focus of this Chapter is the regime in which such scaling properties can determine the final number distribution of DM; namely, when larger states are built up via the agglomeration of smaller ones at low temperatures, as per SM BBN. Like the BBN case, the simplest version of this process applies when the DM is *asymmetric* [73, 74, 81–116], with a particle–anti-particle asymmetry that determines the final DM abundance, similarly to the baryon asymmetry in the SM sector (though the symmetric case is also interesting). The small-DN part of such a scenario was investigated in [75]. In the following we assume, unless specifically stated otherwise, the DM to be asymmetric so the DNN will take positive integer values, and we denote the DN of various DNN as 1-DN, 2-DN, etc.

In the main body of this Chapter, Sections 2.1 and 2.2, we will show that the dark-sector analogue of SM BBN—which we call "Big-Bang Dark Nucleosynthesis" (BBDN)—can produce DN with DNN up to or even exceeding 10^8, resulting in a very wide variety of striking changes to traditional DM phenomenology.

Specifically, we find the number distributions of DN resulting from BBDN satisfy remarkably simple forms. For example, for asymmetric DM with plausible underlying parameter values, DN with DNN $\gtrsim 10^8$ can be synthesised, with the number distribution taking one of two characteristic scaling forms. If there is no substantial bottleneck of BBDN at small DNN the distribution of DN sizes takes on a peaked (in logarithmic space), universal non-power-like functional form,

---

kind of scaling we consider in this Chapter.

[3] See [79, 80] for a detailed investigation of a particular QCD-like model focussing on the properties of the small bound states.

independent of many details of the initial distribution and interactions. This solution acts as an attractor solution and we study how the distribution function of DN approaches this universal scaling form. On the other hand, in the case of a substantial bottleneck of BBDN at small DNN we find the surprising result that DN of even larger DNN, $\gg 10^8$, are often synthesised, again with a simple form of the number distribution. Such behaviours are studied both via numerical solutions of the relevant equations, and from physically motivated approximate analytical solutions.

Such states can give rise to a variety of interesting possibilities, including:

- For reasonable parameter values effectively very heavy ($\geq 10^8$ GeV) DM can be produced by BBDN in the form of large DN (and with one of two possible, essentially model-independent distribution functions). Such heavy DM is in contrast to the usual unitarity limit for point-like DM in the case of thermal freeze-out production [117],[4] and is not usually expected in asymmetric DM models, which seek to link the DM and visible sector abundances.

- Coherent enhancement of interactions: Processes that do not probe the individual constituents will have amplitude going as the DNN k, so scattering cross sections, in for example direct detection experiments, can in principle be enhanced by $k^2 \gtrsim 10^{16}$ compared to the case of a single DM nucleon. Taking account of the reduction in the number density of such states, one still finds an effective increase in direct detection interaction rates scaling as $\sim k$, so effectively *reducing* expected collider signals by $\sim 1/k$ for a given direct detection rate compared to the standard point like case. The physics of the coherent enhancement of direct detection signals, with the accompanying possibility of novel form factors from the dark sector, is discussed in detail in Chapter 3.

- Inelastic processes at both "high energy", of order the DN binding energy

---

[4] Though thermal *freeze-in* production of DM can produce superheavy elementary DM [118] with an energy density yield independent of the superheavy particle mass.

differences, and parametrically lower energy, from long-wavelength collective excitations. Examples of the high energy processes are ones that move between states of different DNNs — fusions and fissions — but there is also the possibility of the extended structure of states leading to a spectrum of excitations, as exists in SM nuclei and atoms (again, see Chapter 3).

- States with large spin: for large composite states, there is the possibility of interactions aligning the spins of many of the constituent states, leading to DN with nuclear spin proportional to k. This is of potential interest in, for example, interactions with SM nuclei in direct detection experiments, and capture in astrophysical objects.

In this Chapter, we focus on the physics of BBDN, leaving the investigation of these possibilities to Chapter 3 and to future work.

Finally, before turning to our analysis of DN and BBDN we emphasise that while there are many specific models which can realise this kind of scenario, we will focus on regimes in which the behaviour can be broadly model-independent in nature.

2.1 Basics of dark nucleosynthesis

While present-day DM may be composed of large bound states, this is generically not the case in the hot early universe. At large temperatures T, the entropy term in the free energy dominates and the chemical equilibrium distribution has almost all DM in small-number states. For small T, compared to the binding energies, the energy term dominates, and chemical equilibrium favours large bound states.

As we discuss in detail in later sections, starting from the situation at high temperatures, large DN may be assembled by an aggregation process where fusions dominate dissociations and fissions. Specifically, if interactions are not so weak as to be frozen out by the time the equilibrium shifts to favour larger states, then larger states will be built up until fusion reactions freeze out due to a combination of falling velocity, and a falling number density from both Hubble expansion and the formation of the large DN themselves.

Since, for the DM masses we consider, the DM is dilute, if we are in kinetic equilibrium then the transition from being kept in equilibrium by dissociations, to fusion reactions dominating, generally happens fast enough to be only a small perturbation to the subsequent fusion process (this technical point is discussed in detail in Appendix A.1). If thermalising interactions are not sufficiently fast to reduce the energy of de-excitation products before they hit another DN, then these may cause dissociations, leading to very different behaviour from the fusions-only approximation (c.f. SM recombination). We will not consider this regime in this Chapter, assuming instead that the de-excitation products decay or thermalise on fast enough timescales.[5]

2.1.1 Freeze-out of fusions

Given that fusions dominate at low T, we can obtain an estimate of the maximum size of DN built up by the aggregation process by investigating when fusion reactions freeze out.

First, let us suppose that the last fusions to freeze out are those between large DN, and also that we end up with a 'peaked' mass distribution in which almost all of the mass is in DN of size $\sim A$. In this case, the rate of fusions for a single DN, per Hubble time, is $\Gamma/H \sim \langle\sigma v\rangle n_A/H$, where $\langle\sigma v\rangle$ is the thermally-averaged fusion cross section, and n_A is the number density of A-DN. Since we have DNN conservation, $n_A = n_0/A$, where n_0 is the DNN density. If the DN are non-relativistic, as required to be aggregating, and in thermal equilibrium (e.g., with

---

[5] In principle, another exception to the statement that, late on, only fusions are important is when the excited states produced by the fusion processes de-excite by the emission of nucleon constituents, as occurs in the SM [119] (many Q-ball models also de-excite by losing charge, e.g. [120]). In general these emitted small-k DN are either quickly re-absorbed by larger DN and do not significantly alter the dynamics of the aggregation process, or they act approximately as an external bath with which the larger DN scatter. In the latter case, as long as enough of the small-small fusion processes can occur without involving nucleon emission, the mass fraction of small DN will be sub-dominant, though they may dominate the number density.

an external bath of light dark-sector particles as we discuss later), then the DN velocity $v_A \simeq v_1 A^{-1/2}$. For large A, saturation of the dark sector nuclear forces implies the internal mass-energy density, ρ_b, of DN matter is roughly constant with size, and that fusion cross sections scale approximately geometrically, $\sigma \simeq \sigma_1 A^{2/3}$, and so

$$\frac{\Gamma}{H} \sim \frac{\sigma_1 v_1 n_0}{H} A^{2/3} A^{-1/2} A^{-1} = \frac{\sigma_1 v_1 n_0}{H} A^{-5/6} \,. \tag{2.2}$$

In general, the temperature, T_b, of the DN bath can differ from the temperature, T, which sets the Hubble expansion rate in the radiation dominated era, and which we assume to be dominantly set by the more numerous SM sector degrees of freedom, as the dark and SM sectors may be essentially decoupled from each other. With this in mind, and using $\sigma_1 \sim 4\pi R_1^2$, $v_1^2 \sim T_b/m_1$, and $4\pi R_1^3 \rho_b/3 \sim m_1$, we then find

$$\frac{\sigma_1 v_1 n_0}{H} \sim 2\times 10^7 \left(\frac{1\,\mathrm{GeV\,fm^{-3}}}{\rho_b}\right)^{2/3} \left(\frac{g_\star(T)}{10.75}\right)^{1/2} \left(\frac{m_1}{1\,\mathrm{GeV}}\right)^{-5/6} \left(\frac{T}{1\,\mathrm{MeV}}\right)^{3/2} \left(\frac{T_b}{T}\right)^{1/2} , \tag{2.3}$$

where the parameters are normalised to SM values both for comparison and because such a parameter region is naturally motivated by many ADM models. Thus, in this scenario, if dissociation stops being important around $T = 1\,\mathrm{MeV}$, then, from equation 2.2, the largest mass that could have been built up is $(2 \times 10^7)^{6/5} m_1 \sim 5 \times 10^8\,\mathrm{GeV}$, corresponding to a radius of $\sim 480\,\mathrm{fm}$ for the fiducial parameter values.[6] Beyond this size, the number density and velocity are too low for interactions to occur. We will see that, for reasonable parameters, this bound may be attained.

Note that, if we scale all of our dimensional parameters to increase mass scales by a factor λ (i.e. $T \mapsto \lambda T$, $\rho_b \mapsto \lambda^4 \rho_b$, etc.), then the freeze-out DN mass scales as $m_{\mathrm{fo}} \mapsto \lambda^{-7/5} m_{\mathrm{fo}}$. Changing the mass scales of the constituents, e.g. by changing the

---

[6] Note that this does not depend on the dark nucleon mass m_1. If some scaling other than $m_k \propto k$ between mass and DNN held, e.g. as in the case of some Q-ball models [76], then equation 2.2 would still apply, but with A replaced by the ratio of the final mass to the mass for which $\sigma_1 v_1 n_0$ was evaluated. Such models, in which binding energies are not a small fraction of the total mass, have quite different properties.

confinement scale in a strongly coupled theory, may be expected to have roughly this effect. Thus, *decreasing* the mass scale of our constituents will tend to *increase* the masses that could be built up, mainly since larger geometric cross sections are available. Going the other way, for $m_1 \gtrsim 100\,\mathrm{TeV}$ (and corresponding scalings of the other parameters), we have $\sigma_1 v_1 n_0 / H < 1$, so there is no build-up in this regime, corresponding to the usual unitarity bound for DM self-annihilations.

Alternatively, the last fusions to freeze out may be those between 'small' + 'large' DN. Compared to large + large fusions, while the possible number density of small DN is larger, the number of separate fusion events onto a given DN needed for the same increase in size is larger by the same factor. However, since in thermal equilibrium the velocities of small DN are larger, the overall rate of size increase is *enhanced* by that factor. To qualitatively understand this scenario, suppose that an order one proportion of the dark nucleons are in small k-DN, and the rest in large A-DN. Then, the rate at which an A-DN increases in size by A is given by

$$\Gamma \sim \langle \sigma v \rangle n_k \frac{k}{A} \sim \delta \frac{1}{4} \sigma_1 v_1 n_0 k^{-1/2} A^{2/3} A^{-1} \ , \tag{2.4}$$

where we used $\langle \sigma v \rangle_{A+k} = \frac{1}{4} \delta \sigma_1 v_1 k^{-1/2} A^{2/3}$, with δ parameterising a possible suppression of small-large cross-sections from the geometric value, e.g. from quantum reflection effects, as per SM nucleon-nucleus interactions. So, the maximum attainable DNN of the DN is

$$A_{\mathrm{fo}} \sim 7 \times 10^{19} \left(\frac{\delta}{\sqrt{k}} \frac{\sigma_1 v_1 n_0 / H}{2 \times 10^{7}} \right)^3 , \tag{2.5}$$

corresponding to $m \sim 7 \times 10^{19}\,\mathrm{GeV}$ (and scaling as $m_{\mathrm{fo}} \mapsto \lambda^{-5} m_{\mathrm{fo}}$) and a radius of $3 \times 10^6\,\mathrm{fm}$ for our fiducial parameter choices.

Similarly, the rate of fusions onto an A-DN for a given k-DN is $\Gamma \sim \langle \sigma v \rangle n_A \sim \frac{n_A}{n_k} \langle \sigma v \rangle n_k$, so the largest DN that can absorb the entire population of small DN also have approximately this same maximum size. Thus, as long as δ is not too small, and a large enough population of small DN exists for long enough, there is the possibility of producing much larger DN via this route, than via an aggregation process in which the DN at any given time are of approximately the same size.

Obtaining significant quantities of DN this large requires that a population of small DN remains around until the end of the aggregation process, i.e. that small + small fusions are slow. If this is the case, but small + large fusion cross sections are roughly geometrical, and we produce a number density of 'seed' large DN $\sim n_0/A_{\text{fo}}$, then, as studied in Section 2.2.4, we will end up with most of the DM mass in DN of size $\sim A_{\text{fo}}$. If we produce a larger seed density, the maximum size will be reduced proportionally, up to a cross-over point at which this size is lower than the freeze-out limit for large + large fusions, at which point we enter that regime. If a smaller seed density is produced, then most of the DN never gets through the 'bottleneck', and remains small, with some sub-dominant population of large DN up to m_{fo}. Section 2.2.4 investigates these regimes in detail.

2.1.2 Bottlenecks, and comparison to BBN

Bottlenecks to nucleosynthesis, in the form of 'anomalously slow' small + small fusion rates for certain channels, are important in Standard Model BBN. There, only small nuclei are synthesised, with almost all of the nucleons ending up in H and ^{4}He, only small amounts in the other $A \leq 7$ nuclei, and entirely negligible amounts beyond this. The $B_D \sim 2\,\text{MeV}$ binding energy of D means that, assuming only $A = 1, 2$ states are occupied, $n_D/n_p \sim \eta(T/m_p)^{3/2} e^{B_D/T}$, and since the baryon to photon ratio $\eta \simeq 6 \times 10^{-10}$, this only becomes $\simeq 1$ at $T \simeq 0.06\,\text{MeV}$. However, slightly before this temperature, the D number density becomes large enough that $2 + 1$ and other processes start occurring, and in fact their rates are $\gtrsim 10^4$ times the Hubble rate, as expected from a calculation along the lines of equation 2.3.

The real bottleneck preventing the synthesis of large nuclei in the SM is the large binding energy per nucleon of ^{4}He compared to subsequent small nuclei. It is not until ^{12}C that the binding energy per nucleon exceeds ^{4}He. In quasi-equilibrium among small-number nuclei, this large binding energy means that ^{4}He dominates the mass fraction along with H, their ratio being set by the abundance of neutrons. The small number densities of $A = 7$ nuclei produced are nowhere near sufficient to make the rate of production of energetically favoured $A \geq 12$ nuclei comparable to the Hubble rate, and so we freeze out with quasi-equilibrium abundances (for a textbook discussion see e.g. [121]). Note that this kind of bottleneck, involving a wrong-sign binding energy difference rather than merely a small right-sign difference as in the D example, gets worse rather than better with decreasing temperature.[7] In summary, SM BBN provides an example of a nucleosynthesis process where the presence of large binding energy differences among small-number states creates a bottleneck. In fact, there are two bottlenecks, the first of which, the D bottleneck, we get through well before fusions have frozen out, but not the second, post-^{4}He.

A bottleneck in BBDN may similarly have the result of preventing significant quantities of large DN from being formed. However, there is also the possibility, as discussed in the previous section, of a suitable bottleneck leading to the build-up of even larger DN than would otherwise have been produced, with a qualitatively different distribution of DN sizes. Section 2.2.4 explores this scenario in detail.

2.2 Aggregation process

Recapping, the cross-over from the high-T regime to that in which dissociations are unimportant occurs in a sufficiently short time that only DN much smaller than the freeze-out size are able to be built up in appreciable quantities during this period. After this, there will be a period of effectively fusion-only aggregation before we reach one of the limits discussed in Section 2.1.1. This section investigates the details of this aggregation process.

Evolving with fusions only, the Boltzmann equation for the k-DN number

---

[7] In the D case, since n_D increases exponentially with falling temperature, the number of $A \geq 3$ states produced beforehand is insufficient to bypass the bottleneck. For this reason, it is somewhat difficult for the bypass process to be dominant for right-sign binding energy differences.

density, $n_k(t)$, is

$$\frac{dn_k(t)}{dt} + 3H(t)n_k(t) = -\sum_{j=1}^{\infty} \langle\sigma v\rangle_{j,k} n_j(t) n_k(t) + \frac{1}{2}\sum_{i+j=k} \langle\sigma v\rangle_{i,j} n_i(t) n_j(t)\,, \quad (2.6)$$

where $\langle\sigma v\rangle_{i,j}$ is the velocity-averaged cross section for the fusion of i-DN and j-DN.[8]

This equation combines together the dilution of number densities due to Hubble expansion, the change in cross sections due to the decrease in DN velocities, and the change in the relative concentrations of k-DN. We can separate these processes out by moving to different variables. Writing the velocity-averaged cross sections as $\langle\sigma v\rangle_{i,j} = \sigma_1 v_1 K_{i,j}$, where the $K_{i,j}$ encode the relative rates of different fusion processes, we have the Boltzmann equation in terms of the dimensionless yields $Y_k \equiv n_k/s$,

$$\frac{dY_k(t)}{dt} = \sigma_1 v_1(t) s(t) \left(-Y_k(t) \sum_j K_{j,k}(t) Y_j(t) + \frac{1}{2} \sum_{i+j=k} K_{i,j}(t) Y_i(t) Y_j(t) \right)\,, \quad (2.7)$$

where $s(t)$ is the total entropy density. Here we assume that entropy in conserved throughout the aggregation process, so $s \propto a^{-3}$. This system of aggregation equations can be solved in terms of relative concentrations, $y_k \equiv Y_k/Y_0$ (with $Y_0 = n_0/s$ the yield of dark *nucleons* irrespective of how they are distributed among DN of different sizes) and by defining a new, dimensionless time w:

$$\frac{dy_k}{dw} = -y_k \sum_j K_{j,k} y_j + \frac{1}{2} \sum_{i+j=k} K_{i,j} y_i y_j\,, \quad (2.8)$$

where

$$\frac{dw}{dt} = Y_0 \sigma_1 v_1(t) s(t) = n_0(t) \sigma_1 v_1(t)\,. \quad (2.9)$$

---

[8] When de-excitation from some fusion events is via nucleon emission, then, as mentioned in footnote 5, the behaviour may still approximately follow the fusions-only aggregation solution. If large + large fusions are the dominant process, as in the 'scaling' regime discussed in Section 2.2.1, then the behaviour of small DN is not crucial. If small + large fusions are most important, as in the 'bottlenecked' regime 2.2.4, and these dominantly de-excite via nucleon emission, this will just reduce their net forward rate by some factor, and, in simple cases, leaves the qualitative behaviour otherwise intact.

Note that Y_0 is constant in time (assuming no entropy injection) by nucleon number conservation, and the solution is normalised such that $\sum_k k\, y_k = 1$ throughout.

In words, the function $w(t)$ describes how quickly the number distribution of DN changes, whereas the set of distributions moved through is determined by the form of the 'aggregation kernel' $K_{i,j}$ and the corresponding solution to the aggregation system equation 2.8.

2.2.1 Scaling regime

The system of aggregation equations, equation 2.8 for all k, is simplest to solve when the $K_{i,j}$ do not depend on w, i.e. when we can absorb all of the time/temperature dependence into the single quantity $v_1(t)$. The simplest case in which this is true is when the DN are in kinetic equilibrium with each other, at some temperature $T_b(t)$. k-DN then have mean-square velocities $\langle v^2 \rangle = T_b/m_k = k^{-1}(T_b/m_1)$. If fusion cross-sections scale approximately geometrically for large DN, then a kernel of the form

$$K_{i,j} = \text{area} \times \text{velocity} = (i^{1/3} + j^{1/3})^2 \left(\frac{1}{i^{1/2}} + \frac{1}{j^{1/2}} \right) , \tag{2.10}$$

is a good approximation for large DN.[9] In this expression we have, for simplicity, replaced the relative velocity, which is non-relativistic in the fusion regime, by an averaged velocity.

Figure 2.1 shows, in both w and t space, numerical solutions for the aggregation dynamics equation 2.8 with this kernel, starting from $y_1(0) = 1$ initial conditions. What is immediately noticeable is that the number distributions at different times have almost the same shape, but shifted relative to each other corresponding to an increase in average size. This arises because the kernel in equation 2.10 is *homogeneous*, $K_{bi,bj} = b^\lambda K_{i,j}$ with, here, $\lambda = 1/6$. Physically, if we scale up the DNN of

---

[9] In the plots for this chapter, the slightly different kernel $K_{i,j} = (i^{2/3}+j^{2/3})(i^{-1/2}+j^{-1/2})$ was used, to match cases investigated in the mathematical literature [122]. The scaling relationships and qualitative behaviour are the same for both kernels.

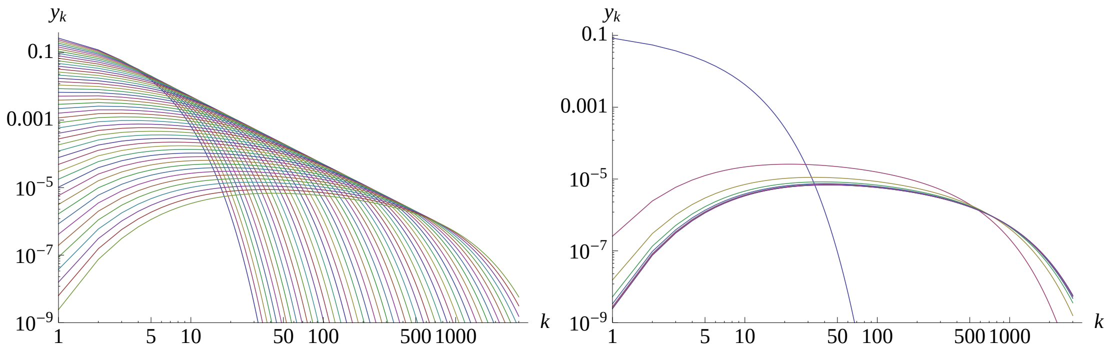

Figure 2.1: *Left:* Number distributions obtained by solving the system of equations determining aggregation dynamics, equation 2.8 for all k, from single-nucleon initial conditions, $y_k(0) = \delta_{k1}$, at equally-spaced values in $\log w$ up to a maximum of $w = 75$. The first curve is a Kronecker delta $y_1(0) = 1$, the second curve is the one with smallest intercept on the k axis, etc. Note that distribution of DN sizes very quickly broadens in w-time. *Right:* The same number distributions at half e-folding time intervals, assuming DN temperature falling with scale factor and $w(t)$ evolving as per equation 2.15, with $w_{\max} = 75$. As the physical time goes to infinity the distribution is given by the $w = w_{\max}$ distribution shown by the thick solid curve.

all of the DN by some factor, this just corresponds to an *overall* scaling of the rate of fusions, and doesn't change the relative rates of different-number processes. It is known [123] that, for such kernels, there is generally a 'scaling solution' such that almost any finitely-supported initial conditions eventually converge to the form

$$y_k(w) = \frac{1}{\overline{k}(w)^2} f\left(\frac{k}{\overline{k}(w)}\right) , \tag{2.11}$$

where $\overline{k}(w) \propto w^{1/(1-\lambda)}$ is the 'characteristic size' of DN at time w, f is the kernel-dependent scaling solution, and the $1/\overline{k}^2$ factor ensures correct normalisation.

In our case, we can check whether the numerical solutions in Figure 2.1 obey this scaling behaviour by choosing a plausible form for $\overline{k}$ (e.g. for a peaked number distribution, we could take one over the total number of DN, $1/\sum_k y_k$), and plotting $\overline{k}^2 y_k$ against $k/\overline{k}$, as shown in Figure 2.2. We see that, for $y_1(0) = 1$ initial conditions, the distribution converges very quickly to such a scaling solution, which can then be used to extrapolate to larger w values. From the mathematical theory of aggregation developed in other contexts [122, 124], we expect $f(x)$ to drop as $\sim x^{-\lambda} e^{-\text{const.}\ x}$ for $x \gg 1$, and to have the form $f(x) \sim x^{\theta} e^{-\text{const.}/\sqrt{x}}$ for

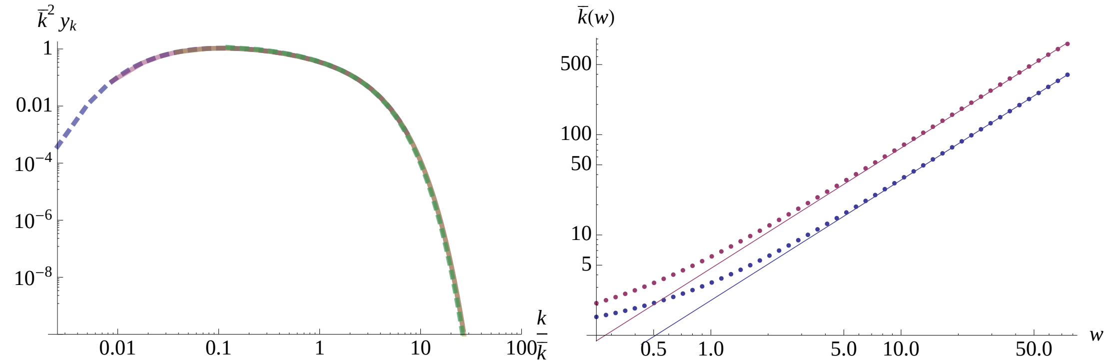

Figure 2.2: Illustration of convergence of aggregation equation solutions to ‘scaling’ behaviour. *Left*: Solutions of aggregation equation after different ‘times’ w (with $y_1(0) = 1$), plotted on scaled axes $\overline{k}^2 y_k$ versus $k/\overline{k}$, where $\overline{k} = 1/\sum_k y_k$. Green dashed line shows solution at $w = 3$, yellow at $w = 8$, red at $w = 25$, and blue dashed at $w = 75$. The almost complete overlap shows that convergence to the attractor form of the ‘scaling solution’ is rapid. *Right*: Plot of $\overline{k}$ behaviour with time—dots are numerical $\overline{k}(w)$ values, lines are $w^{6/5}$ curves. Blue are for $\overline{k}(w) \equiv 1/\sum_k y_k$, red are for $\overline{k}(w) \equiv \sum_k k^2 y_k$.

$x \ll 1$, with θ some constant, both of which match sensibly onto the numerically obtained form. Also, the behaviour of $\overline{k}(w)$ with w matches, for larger w, the $\propto w^{6/5}$ form predicted from $\lambda = 1/6$. This also holds for different choices of $\overline{k}$, as expected for a peaked number distribution.

2.2.2 (In-)Dependence on initial conditions

As discussed in Section 2.1, we do not expect to start the fusions-only aggregation process with single-nucleon-only initial conditions—instead, we will have whatever was produced during the phase when dissociations were still important. Furthermore, fusion cross sections between small DN will probably not be well approximated by the geometrical scaling appropriate to large DN; for example, SM cross sections between small nuclei display very complicated behaviour. Since, as we discuss in the next section, there is only a finite w time available for aggregation due to Hubble expansion, the question is whether these initial conditions, and small-k behaviour, converge to the scaling solution quickly enough for appropriate measures of convergence.

If the initial conditions include a subdominant large-k ‘tail’ for which large + large fusions are frozen out (see the right panel plot of Figure 2.3 as an example), then as long as the aggregation of smaller DN proceeds not much slower than the scaling behaviour, only a small proportion of the small DN fuse with those in the tail. To see this we can approximate the tail by purely A-DN, and use the fact that the rate at which a given small k-DN fuses into the tail is $\Gamma_{k+A} \sim \delta \sigma_1 v_1 n_A A^{2/3} k^{-1/2}$. So, writing the fraction of the DN in the tail as $\alpha = A n_A / n_0$,

$$\frac{d(1-\alpha)}{dt} \sim \Gamma_{k+A}(1-\alpha) \quad \Rightarrow \quad \frac{d \log(1-\alpha)}{dw} \sim -\delta \frac{n_A}{n_0} A^{2/3} k^{-1/2} \,. \tag{2.12}$$

While α is small, so the small-k build-up proceeds like the scaling solution, we have $k \sim w^{6/5}$. Since $A + A$ fusions are frozen out, n_A is roughly constant throughout, so

$$\frac{d\alpha}{dw} \sim \delta \left(\frac{n_A}{n_0}\right)^{1/3} \alpha^{2/3} w^{-3/5} \quad \Rightarrow \quad \alpha_{\max} \sim \delta \frac{n_A}{n_0} w_{\max}^{6/5} \sim \delta \frac{n_A}{n_0} k_{\max} \,. \tag{2.13}$$

Thus, either $\delta k_{\max} \gtrsim A$, in which case the tail is subsumed into the scaling distribution, or else α is always $\ll 1$. Note that this only occurs because k increases sufficiently quickly with w. As we shall see in Section 2.2.4, if that does not happen, then none of the DN may ever reach the scaling regime, and $\alpha_{max} \sim \frac{n_A}{n_0} w_{\max}^3$ can become of order 1, so all of the small DN can be absorbed by the frozen-out tail.

Alternatively, suppose that the initial conditions have some component for which similar-size fusions are not frozen out, e.g. the left panel of Figure 2.3. If these have the same average size as a monomer-only scaling solution after δw, then the eventual distribution will be close to the monomer-only solution after $w_{\max} + \delta w$. Since small + large fusions are faster than large + large, the ‘memory’ of the initial shape is erased fairly efficiently.[10]

---

[10] Similarly, if the small-k cross sections are larger than those extrapolated down from large k, the effect is to start the large-k process slightly earlier, $w \to w + \delta w$, while if the cross sections are smaller than the extrapolation then the solution interpolates between the scaling and bottlenecked regimes—see Section 2.2.4.

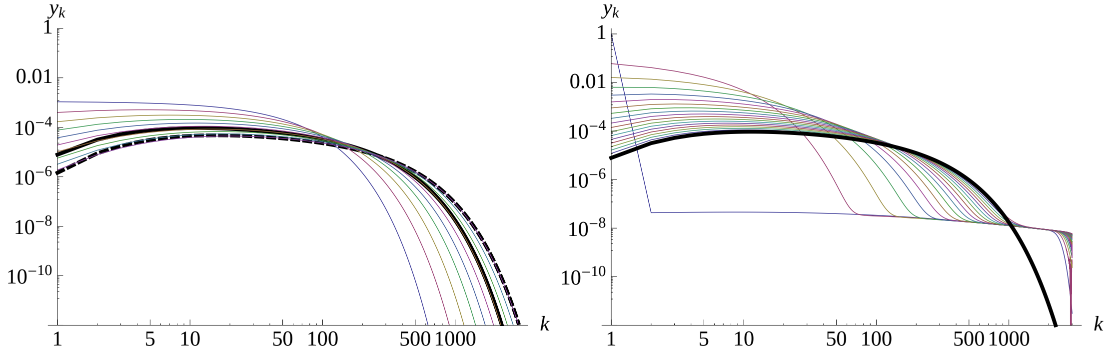

Figure 2.3: Illustration of convergence of aggregation equation solutions to 'scaling' behaviour, for more complicated initial conditions. *Left*: Coloured curves are solutions of aggregation dynamics, starting from $y_k(0) = e^{-k/30}$ initial conditions, at equally-spaced w values from 0 to 25. For comparison solid black curve shows solution at $w = 25$ for monomer-only initial conditions, while black dashed curve is monomer-only solution at the later time $w = 33.25$. We see that despite the change in initial conditions we still end up with the scaling distribution but now it is slightly shifted in w-evolution compared to the monomer-only case. *Right*: Solutions of aggregation dynamics at equally-spaced w values from 0 to 25, starting from initial conditions with most of the mass in single nucleons ($y_1(0) = 0.97$), but also a sub-dominant population in a broad tail out to large k values (as might arise from e.g. build-up while most of the nucleons are trapped behind a low-k bottleneck). The black curve is the solution at $w = 25$ for monomer-only initial conditions. Since the initial state has only a small fraction of the nucleons in the tail, and fusions between states in the tail are frozen out, the tail has no significant effect on the majority of the scaling solution.

Figure 2.3 illustrates these behaviours numerically, with the left panel showing the convergence of non-frozen-out initial conditions to a slightly-further-along scaling distribution, and the right panel showing that a sub-dominant frozen-out tail has little effect on the scaling solution obtained.

2.2.3 Real-time behaviour

The scaling distribution gives us the form of the $y_k(w)$ solution—to obtain the real-time distribution $y_k(t)$, we need to know the behaviour of $w(t)$ from solving equation 2.9. Generally, we are most interested in the $t \to \infty$ limit, so want to find $w(t \to \infty)$. To obtain this we in turn need to know the behaviour of $v_1(t)$, which is simple in the case that the DN are in *kinetic* equilibrium throughout the aggregation process.

The simplest way for the DN to be in kinetic equilibrium is for them to be in thermal contact with a bath of lighter particles during the aggregation process. If this bath is relativistic, so $T_b \propto 1/a$ (here ignoring possible changes in the number of species for simplicity), and taking $v_1 = \sqrt{T_b/m_1}$, we obtain, assuming radiation domination,

$$\frac{dw}{dT} \simeq -\left.\frac{n_0 \sigma_1 v_1}{H}\right|_{T_0} \left(\frac{T}{T_0}\right)^{1/2} \frac{1}{T_0}\,, \tag{2.14}$$

where T_0 is the temperature when $w = 0$, i.e. at the start of the aggregation process. Solving this,

$$w(T) \simeq \frac{2}{3} \left.\frac{n_0 \sigma_1 v_1}{H}\right|_{T_0} \left(1 - \left(\frac{T}{T_0}\right)^{3/2}\right) \to \frac{2}{3} \left.\frac{n_0 \sigma_1 v_1}{H}\right|_{T_0}\,, \tag{2.15}$$

where the limit is $T \searrow 0$. The right panel of Figure 2.1 shows the solutions obtained at different t values, assuming this relationship between w and T, illustrating the convergence towards the $w = w_{\max}$ solution.

Alternatively, if the hidden sector bath is non-relativistic, so $T_b \propto a^{-2}$, we obtain

$$w(T) \simeq \frac{1}{2} \left.\frac{n_0 \sigma_1 v_1}{H}\right|_{T_0} \left(1 - \left(\frac{T}{T_0}\right)^{2}\right) \to \frac{1}{2} \left.\frac{n_0 \sigma_1 v_1}{H}\right|_{T_0}\,. \tag{2.16}$$

Since $\overline{k} \sim w^{6/5}$, we have $\overline{k}(t \to \infty) \sim \left(\left.\frac{n_0 \sigma_1 v_1}{H}\right|_{T_0}\right)^{6/5}$ in both cases. This agrees with the approximate freeze-out calculation of equation 2.2, which had $\Gamma/H \sim \frac{n_0 \sigma_1 v_1}{H} A^{-5/6}$.

Generally, since from equation 2.9 $\frac{dw}{d\log a} = \frac{n_0 \sigma_1 v_1}{H}$, and during the radiation era we have $H \propto a^{-2}$, $n_0 \propto a^{-3}$, and writing $v_1 \propto a^{-\gamma}$, we have $\frac{dw}{d\log a} \sim a^{-(1+\gamma)}$, so, $\Delta w \sim \Delta\left(a^{-(1+\gamma)}\right)$ as we obtained in equations 2.15) and 2.16. Thus the *bulk of the aggregation process takes of order a Hubble time to complete.* This is illustrated in the right panel of Figure 2.1, which shows solutions at half-e-folding-time intervals. Such behaviour just comes from the freeze-out properties of the interactions, so in the bottlenecked regime we take at most this long as well—in fact, as we shall see in the next section, that process may take much less than a Hubble time.

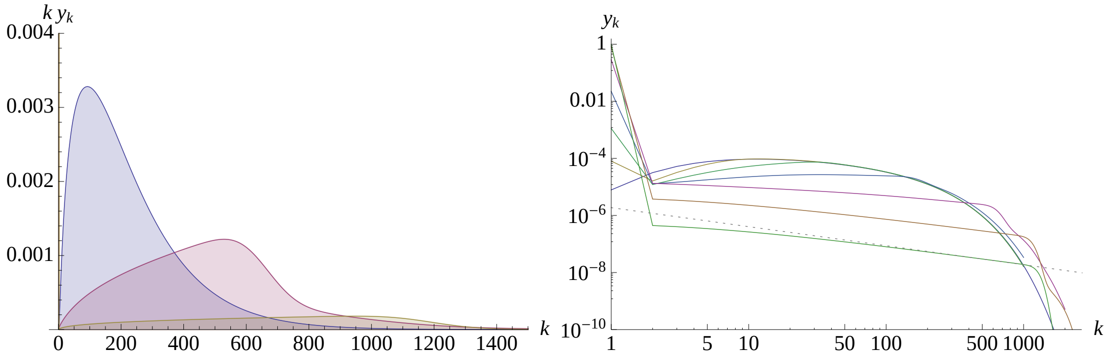

Figure 2.4: Illustration of transition between scaling regime and bottlenecked regime. *Left:* Mass distribution at $w = 25$, starting from initial conditions of single nucleons, $y_k(0) = \delta_{k1}$, for the original kernel with $K_{1,1} = 4$ (purple), and modified kernels with $K_{1,1} = 10^{-4}$ (red), and $K_{1,1} = 10^{-5}$ (yellow). We see that, within this range, making $1 + 1$ fusions slower results in building up larger DN. *Right:* Number distribution at $w = 25$, again starting from initial conditions of single nucleons, for $K_{1,1} = (4, 1, 10^{-1}, 10^{-2}, \ldots, 10^{-6})$. The dotted line aligned with the $K_{1,1} = 10^{-6}$ (green) curve is $\propto k^{-2/3}$. We transition from converging very quickly to the scaling solution, to ending up with a power-law distribution cutting off at larger k. Between $K_{1,1} = 10^{-5}$ and 10^{-6}, the maximum k reached hardly increases, with the overall number density in the power-law tail just going down—we have reached the freeze-out limit for building up large DN.

2.2.4 Bottlenecked regime

As illustrated in Section 2.2.1, if the fusion rates, as parameterised by $w_{\max}$ and the $K_{i,j}$, are not too small compared to the support of our initial conditions, then we reach the scaling regime of the attractor solution. However, if some of the fusion rates are reduced far enough to 'trap' a proportion of the DN in a small-k region for long enough, then we will not reach the scaling regime. Counter-intuitively, this can result in building up *larger* DN than would otherwise have been the case. As roughly described by equation 2.4, this occurs because small + large fusions are less velocity-suppressed in kinetic equilibrium than large + large fusions, so, if there is a bath of small DN present throughout the aggregation process, build-up interactions may freeze out at higher A. Figure 2.4 shows a simple example of moving between the scaling and bottlenecked regimes, which may be helpful to keep in mind through the following.

Since small + large fusions keep the number density of large DN the same, they act to increase the rate of large + large fusions, which goes as $A^{2/3}A^{-1/2} = A^{1/6}$. If Γ/H becomes of order 1 or higher, then large-large fusions will start operating and bring it down to ~ 1, establishing a scaling distribution for the larger DN. Since the rate of fusions for a single small DN is larger than that for large DN, this also means that all of the small DN will be used up, clearing the bottleneck and placing us in the scaling regime.

The more interesting case is when large-large interactions are always frozen out. We can then model the aggregation process as a combination of the slow creation of large post-bottleneck 'seed' DN, and the fast accretion of small pre-bottleneck DN onto these. Looking first at the accretion process, from our previous assumptions the growth rate for a large DN scales geometrically, i.e. proportional to $R^2 \sim A^{2/3}$. So, $dk/dw \sim k^{2/3} y_s$, where y_s parameterises the concentration (and size) of small DN, and thus $k \sim \left(\int dw\, y_s\right)^3$. If the bath of small DN is populated throughout most of the w time, then $k_{\max} \sim w_{\max}^3$, realising the freeze-out bound of equation 2.4.

As well as the maximum size, we are also interested in the number distribution over k. If a seed DN is produced at time $w_{\rm inj}$, then its eventual size will (for roughly constant y_s) be $k \sim (w_{\max} - w_{\rm inj})^3$. More precisely, if we change time variable to z, where $dz/dw = y_s$, we have $k \sim (z_{\max} - z_{\rm inj})^3$. This means that the relationship between injection time $z_{\rm inj}$ and final size k is given by $-\frac{dz_{\rm inj}}{dk} \sim k^{-2/3}$. Next, write $a_k(z)$ for the total concentration of seed k-DN injected by time z. Since accretion only changes the k-number, and not the density, of an injected seed population, we obtain

$$y_k = -\frac{d}{dk}\left(\sum_j a_j(z_{\rm inj}(j \to k))\right) = -\sum_j \frac{da_j}{dz}\frac{dz_{\rm inj}(j \to k)}{dk} \sim k^{-2/3}\sum_j c_j \frac{da_j}{dz}\ . \tag{2.17}$$

For k large compared to the j which dominate the sum, we can write this as $k^{-2/3} f_i(z_{\rm inj})$. In particular, if for small z the injection rate is roughly constant (this is reasonable, since only a small fraction of the pre-bottleneck bath has been used up, and the temperature, scale factor etc. change by only a small amount), then for large k we should have a power law number distribution $y_k \sim k^{-2/3}$.

As we increase the injection rate f_i, we move through the three different regimes described at the end of Section 2.1.1:

- If the injection rate is small enough, then most of the small bath is not used, and most of the mass is stuck behind the bottleneck, with a small proportion in a $y_k \sim k^{-2/3} f_i(z_{\text{inj}})$ tail, which extends to $k_{\max} \sim w_{\max}^3$. As an example, if we assume that f_i decreases with time, such that the nucleon number integral $\int^{k_{\max}} dk\, k\, k^{-2/3} f_i$ is dominated by the upper decade, scaling as $k_{\max}^{4/3} f_i(0)$, then the upper limit of this regime is given by $f_i(0) \sim k_{\max}^{-4/3} \sim w_{\max}^{-4}$.
- For larger injection rates, we use up all of the small bath before we reach $w_{\max}$, so we build up to correspondingly smaller $k_{\max}$. Under the same assumptions on f_i, we have $k_{\max} \sim f_i(0)^{-3/4}$.
- For sufficiently large injection rates, large-large fusions eventually become important, and we enter the scaling regime. We expect this to happen roughly when $k_{\max}$ for the addition process is comparable to the k values of the scaling peak. Since this has $\overline{k} \sim w^{6/5}$, under the above assumptions on f_i we expect the cross-over to be at around $f_i(0) \sim w_{\max}^{-8/5}$.

In the first regime, the proportion of DM in the pre-bottleneck bath stays roughly constant, so $\frac{dz}{dw} = y_s \simeq \text{const}$. From the previous section, $\Delta w \sim \Delta(a^{-(1+\gamma)})$, so the bulk of the process again takes of order a Hubble time. For the intermediate regime, we use up most of the small bath within $\Delta w \simeq (3k_{\max})^{1/3} < w_{\max}$, a small fraction of a Hubble time. For the rest of w time, either large-large fusions are frozen out, in which case we only make small modifications to the number distribution, or we enter the scaling regime.

Figure 2.4 shows the numerical solution of a particularly simple bottlenecked example—using the geometrical kernel of equation 2.10, but reducing $K_{1,1}$. In this case, the injection rate $f_i \propto y_1^2$, so for most of the addition process it is constant,

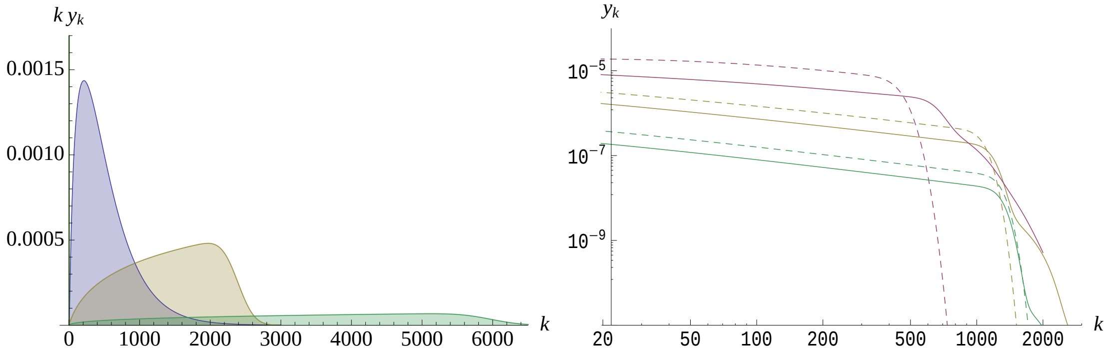

Figure 2.5: Further illustrations of behaviour in the bottlenecked regime. *Left:* Mass distribution at $w = 50$, starting from single nucleons, for original kernel $K_{1,1} = 4$ (purple), and modified kernels with $K_{1,1} = 10^{-5}$ (yellow), $K_{1,1} = 10^{-6}$ (green) (latter two in the 'addition approximation', i.e. only taking into account $1 + k \to (1 + k)$ fusions). Comparing to Figure 2.4, going to larger w increases the difference between the bottlenecked and scaling solutions. *Right:* Solid lines are number distributions at $w = 25$, starting from single nucleons, for $K_{1,1} = 10^{-4}$ (red), $K_{1,1} = 10^{-5}$ (yellow), and $K_{1,1} = 10^{-6}$ (green). Dashed lines are number distributions in the addition approximation.

giving a power-law number distribution $y_k \sim k^{-2/3}$ for large k. The right panel of Figure 2.4 illustrates how we move through the three regimes identified above as we decrease $K_{1,1}$. We start out converging quickly to the scaling distribution, but for $K_{1,1} \lesssim 10^{-4}$ we never reach this regime, ending up with a power law out to larger k. For $K_{1,1} \lesssim 10^{-5}$, most of the $k = 1$ population never makes it past the bottleneck, and our power-law tail goes to smaller concentrations rather than higher k values.

The right panel of Figure 2.5 shows explicitly that, for the bottlenecked solutions, we are close to being in the addition-dominated regime, i.e. the dominant process is $1 + k \to (k + 1)$. Comparing the left panel to Figure 2.4 illustrates that, as we increase $w_{\max}$, the difference between the $k_{\max}$ attainable in the scaling and bottlenecked regimes increases.

As was the case in the scaling regime, sufficiently small changes in the initial conditions, or in the rates of individual processes, will not make a major difference to the eventual number distribution. If we start with a small mass fraction of the DN past the bottleneck, this will be equivalent to an injection spike at $z = 0$, and so a bump at the end of the overall tail. If some of the rates for small + large fusions differ from the geometrical approximation, say for large DN of size k, then this will affect all of the large DN that grow to sizes $> k$—as long as the reduction in the rate is not large enough to cause a further bottleneck, there will be little change in the qualitative form of the final distribution.

2.3 Aspects of dark sector phenomenology

So far, we have investigated the BBDN process, and the number distribution of DN that may result from it. The DM self-interactions, and the extended hidden sector needed to realise such models, mean that these theories generically have the possibility of interesting hidden sector phenomenology, including non-standard indirect detection signals, modifications of halo properties, and early-universe signatures of extra species. Also, though not required in these models, it is possible that the DN have sufficiently strong interactions with SM states to give signals in future direct detection experiments. If that is the case, then such signals may differ from those of usual WIMP DM, and have different relationships to collider bounds. Additionally, such interactions may lead to the capture of DN in astrophysical objects, and then self-interactions among captured DN could become important. We will discuss the latter two possibilities in Chapter 3.

In standard ADM models, annihilations with the relic symmetric population can lead to astrophysical energy injections, most detectably in the early universe, putting a limit on how large this population can be. In nuclear DM models there is additionally the energy injected by inelastic processes, particularly the release of binding energy from fusions.

For simple ADM models with DM mass $\lesssim 100\,\mathrm{GeV}$, annihilation of the symmetric component generally needs to go into, or via, lighter hidden sector particles rather than directly to the SM, to avoid constraints from direct detection and collider experiments, as discussed in Section 4.2.4. We will see below that in the case of DN, the constraints from direct detection on the SM couplings of individual DN constituents are often even tighter, confirming the need to annihilate into lighter hidden sector particles. In addition, there must exist some lighter state(s) through which DN fusions can de-excite, as the limits on SM interactions are generally strong enough that we cannot de-excite fast enough via those alone. We also need some mediator particle to transmit the binding force. If any of these additional states are sufficiently light, strongly-interacting, or long-lived, then there may be astrophysical constraints on their properties.

2.3.1 Post-nucleosynthesis energetics in the dark sector

Since we have been considering DM with strong self-interactions, an obvious question is whether these self-interactions have late-time consequences. For elastically-scattering DM with velocity-independent self-scattering cross section, the observational limit on the self-scattering cross section is $\sigma_{XX}/m_X \lesssim 1\,\mathrm{barn}/\,\mathrm{GeV}$, as discussed in Section 1.1.4. For a population of A-DN,

$$\frac{\sigma_{AA}}{m_A} \simeq \frac{0.05\,\mathrm{barn}}{\mathrm{GeV}} A^{-1/3} \left(\frac{1\,\mathrm{GeV}}{m_1}\right)^{1/3} \left(\frac{1\,\mathrm{GeV}\,\mathrm{fm}^{-3}}{\rho_b}\right)^{2/3}, \tag{2.18}$$

in the notation of equation 2.3. From the results of Section 2.1.1, if we scale $M_1 \mapsto \lambda M_1$, $\rho_b \mapsto \lambda^4 \rho_b$ etc., then in the scaling regime, $A \mapsto \lambda^{-12/5} A$. Thus, $\frac{\sigma_{AA}}{m_A} \mapsto \lambda^{-11/5} \frac{\sigma_{AA}}{m_A}$, so we would hit the observational limit at roughly $10\,\mathrm{MeV}$ scales for the constituents, assuming that we built up to the largest allowed sizes.

Realistically, the situation can be more complicated than this. Firstly, there would be a spectrum of DNN values. However, for the scaling distribution, and simple forms of the bottlenecked distributions, the area distribution $k^{2/3} n_k$ and the mass distribution $k n_k$ both receive most of their contribution from a single decade or so of nucleon numbers, so the above calculations will hold approximately.

More interestingly, the fact that DN collisions may not be elastic could have phenomenological consequences. Since, neglecting collisions, DN of different sizes will have the same velocity distribution, with e.g. $v \sim 10^{-3} c$ in the Milky Way, large DN will have kinetic energies much larger than the single-nucleon binding energy scale. Thus, it is possible that DN-DN collisions will result in inelastic collisions, including nuclear fragmentations, transitions to excited states, and fusions.

Some types of collisions may be dissipative, reducing the average kinetic energy (KE) per nucleon of the final state DN. Examples include scattering to excited states, in which some of the initial KE is lost into de-excitation products (fusions with sufficiently small binding energy differences also lose KE overall). If these de-excitation products interact with the SM, there may be indirect detection signals from these processes. Independently, the inelastic form of the scattering will tend to lead to the contraction of DM mass distributions, as compared to elastic scatterings. It may be the case that, in regions of sufficiently high DM density, there is the possibility of run-away contraction (in particular, if the DM is self-gravitating, then removing KE results in the distribution contracting and also heating up, due to the negative heat capacity). More generally, the effects and constraints will be different from the usual simulations of elastic DM self-interactions.

On the other hand, the presumed binding-energy-based stability of large DN means that there may be exothermic collisions, in which the average KE of the DN is increased (c.f. fusions in stars, in the SM). If the velocity kick given to the DN is large compared to the velocity dispersion in the halo, exothermic collisions will have the effect of clearing out the central high-density region, until the number density is low enough that collisions occur once per particle per Hubble time. Since smaller halos tend to have smaller velocity dispersions, small velocity kicks may only modify structure on small scales (where there are problems with Λ-CDM predictions for structure, as discussed in Section 1.1.5).

These general effects of inelastic DM self-interactions are not specific to nuclear DM, and a number of models have been investigated in the literature. In particular, models in which the DM transforms under some approximate symmetry can easily realise small mass splitting, and the effects of illustrative cases corresponding to a

Yukawa self-interaction have been considered in [125, 126].

Turning to the energy released in de-excitations; considering energy injections once the aggregation process has frozen out, the injection rate is just set by the local DM velocities and number density (which, in regions where only a small fraction of the DN undergo self-interactions, will be the standard collisionless DM values). Generally, if the rate is velocity-suppressed (as for large DN-DN collisions), and freeze-out is before BBN, then present-day cosmic ray (CR) constraints dominate those from earlier times, if the injection is to sufficiently energetic SM particles [127, 128]. Velocity-independent processes with rate proportional to n^2 have BBN, CMB and CR constraints within a few orders of magnitude of each other, depending on the form of SM injections [127–129].

In regions where only a small fraction of DN undergo fusions, the proportion of the DM mass density represented by the binding energy released in late-time fusions is

$$\langle\sigma v\rangle n_A t_{\rm sys}\frac{\Delta BE}{M_A} \sim 10^{-3}A^{-2/3}\frac{\Delta BE}{A^{2/3}0.01m_1}\left\{\frac{\rho_{\rm DM}}{0.3\,{\rm GeV\,cm^{-3}}}\right. \\ \left.\left(\frac{1\,{\rm GeV\,fm^{-3}}}{\rho_b}\right)^{2/3}\left(\frac{1\,{\rm GeV}}{m_1}\right)^{1/3}\left(\frac{v}{10^{-3}}\right)\left(\frac{t_{\rm sys}}{10\,{\rm Gyr}}\right)\right\}\,, \tag{2.19}$$

(where the ΔBE terms corresponds to the binding energy difference in $A+A \to 2A$ fusions scaling as $A^{2/3}\beta$, in the notation of equation 2.1; $\beta = 0.01m_1$ is around the SM value). This corresponds to a proportion $\sim 0.1A^{-1/3}\{\ \}$ of the DN undergoing collisions, where $\{\ \}$ indicates the term in curly brackets in equation 2.19, so the total KE of the DN involved is $\sim 7\times 10^{-8}A^{-1/3}\{\ \}$ of the DM mass density.

As an illustration of a comparable indirect detection signal, for standard symmetric DM, the proportion of the DM mass density released in s-wave annihilations is

$$\langle\sigma v\rangle n_X t_{\rm gal} \sim 3\times 10^{-8}\left(\frac{100\,{\rm MeV}}{m_X}\right)\left(\frac{\langle\sigma v\rangle_X}{\rm pb}\right)\left(\frac{\rho_{\rm DM}}{0.3\,{\rm GeV\,cm^{-3}}}\right)\,, \tag{2.20}$$

where we take $t_{\rm gal} \sim 10\,{\rm Gyr}$. Since the detectability of CR signals from annihilating DM at $\sim$ pb cross-sections depends on the SM injection channel etc. [130], the same applies for DN collisions within the A ranges of interest. Given the range of initial DN masses, and the possibility of excited states of DN, such signals may have a richer structure than the indirect detection signals usually considered. Additionally, the geometric cross sections we have assumed give different velocity dependence to the partial wave processes usually considered.

Also, as considered above, for dissipative collisions in sufficiently dense regions, there may be the possibility of (run-away) contraction of the DN distribution, which could significantly affect signals from e.g. the Galactic centre.

2.3.2 Light dark sector states

As mentioned above, DN models generally require additional lighter hidden sector states. Since the assumption is that these do not make up the bulk of the DM, they either need to never have a large abundance (generally difficult to realise in thermal ADM histories), be sufficiently light and weakly interacting with the SM to persist as dark radiation, or their abundance needs to be reduced.

Reducing the yield of a species can occur by transferring its energy density to other hidden sector species, or to the SM. In the latter case, if this injection occurs during or after BBN, there are constraints on its form and magnitude. For injection to hadronic channels, the total energy density injected after $T_\gamma \sim 1\,{\rm MeV}$ must be significantly below that of the DM. For electromagnetic ($e^\pm$ or γ) injection, the dominant effect at times before thermalisation becomes inefficient, $\lesssim 10^4\,{\rm sec}$, is alteration of the photon-baryon ratio,[11] which constrains the amount of energy injected to $\lesssim 0.1 \rho_\gamma$ [131]. At later times, any energy injections, apart from those to neutrinos, must again be significantly sub-DM [132–134].

For hidden sector particles of mass $\gg 100\,{\rm MeV}$, their (symmetric) chemical

---

[11] The other significant effect is increasing the photon temperature relative to that of neutrinos, so decreasing $N_{\rm eff}$ at later times compared to BBN.

equilibrium abundance (at the SM temperature) by BBN times is significantly sub-DM. The dominant constraints on their couplings to the SM generally come from collider experiments, and permit decay times of $\ll 1\,\mathrm{sec}$ (e.g. [135]). So, in these cases, if such decays are possible, then there are generally consistent scenarios in which any initial abundance decays to the SM before BBN.[12]

On the other hand, for hidden sector particles with $m \ll 100\,\mathrm{MeV}$, astrophysical, collider, and other observations place strong constraints on their SM couplings. These restrict their SM decay times to $\gtrsim 1\,\mathrm{sec}\left(\frac{100\,\mathrm{MeV}}{m}\right)^{1+2k}$, where $k \geq 0$ is set by the mass dimension of the decay operator (see e.g. [136, 137]), and mean that direct interactions with the SM are frozen out below very high temperatures ($T_\gamma \gg m$).[13] If $m \gtrsim 10\,\mathrm{keV}$, purely SM decays occur at $T_\gamma < m$, so the decay of a thermal abundance would transfer $\gtrsim \rho_\gamma$ energy density to the SM. For smaller m, the decay time is $\gtrsim 10^4\,\mathrm{sec}$, so the constraints on energy injection to the SM are much more severe. In either case, limits on SM energy injection generally imply that the majority of the initial thermal energy density needs to be transferred to other, lighter hidden sector states.[14] Considering these states in turn, we eventually require that there be long-lived hidden sector states, which will act as dark radiation, at least during the early universe. Extra relativistic species are compatible with current observations [138], and if the hidden sector is at a lower temperature than the SM, its contribution to the effective number of such species N_{eff} may be small. Plausible candidates for these species within hidden

---

[12] As noted in previous sections, obtaining sufficiently fast annihilations (directly to the SM) to reduce the energy density to sub-DM levels is generally difficult for $m \ll 100\,\mathrm{GeV}$, without involving lighter states or non-minimal flavour structures.

[13] Faster decay times may be possible with more complex dark sectors, but these generally involve additional lighter dark states.

[14] It may be possible to realise alternative scenarios in which energy is transferred to the SM indirectly, via other hidden sector states. If the hidden sector is at a slightly lower temperature than the SM, and the transfer is before $\sim 10^4\,\mathrm{sec}$, this may be safe (sitting at the upper end of the mass range, and transferring mostly before BBN, may also work). This would require that number-changing interactions with other hidden sector states are sufficiently fast to keep the light state in thermal equilibrium during the process. Three-body interactions with heavier hidden sector states are suppressed by two factors of the heavy state number density (which is small for DM of SM mass or higher), and inelastic two-body collisions are only relevant if such excitations are accessible at low temperatures, imposing model-building constraints. Alternatively, models in which SM energy injection is dominantly to neutrinos may also be viable.

sector models include very light pseudo-Nambu-Goldstone bosons or Z' states.

2.4 Summary

In this Chapter we have studied the "Big Bang dark nucleosynthesis" process by which 'nuclear' bound states of DM may be built up in the early universe. Specifically we focussed on the case of asymmetric DM models where the nuclear binding energy per dark nucleon saturates in the large nucleon number limit.

We find that, if fusions between small dark nuclei (DN) happen sufficiently fast, and fusion cross-sections between large DN scale on average geometrically, the resulting number distribution generically takes on a universal form, illustrated in Figures 2.1 and 2.2. This result is broadly independent of small changes to the initial conditions or fusion rates, assuming that the DN are in kinetic equilibrium throughout the process, as discussed in Section 2.2.2. The average mass of the DN built up during this process can be as large as $\sim 10^8\,\mathrm{GeV}$, for SM-like dark sector parameters.

If fusion reactions between small DN are not large enough to reach this regime, but large-small fusions still occur at an appreciable rate, then there is the counter-intuitive possibility of building up even larger DN due to the higher velocities of smaller particles, leading to larger fusion rates. The resulting number distribution generally takes the form of a power law multiplied by an 'injection profile' parameterising the change of small-small fusion rates with time. Figures 2.4 and 2.5 illustrate this behaviour.

Given this possibility of building up large dark nuclear bound states, direct detection signals may be modified in a number of ways—by the coherent enhancement of SM-DM interactions, by dark form factors if the DN radius is significantly larger than SM nuclear radii, and by inelastic interactions if there are sufficiently low-lying excitations. We discuss some of these possibilities in more detail in Chapter 3.

The possibility of inelastic collisions can also lead to interesting astrophysical dark sector interactions as mentioned in Section 2.3.1. These include annihilation-type indirect detection signals, which are usually absent from asymmetric DM models (and here may have a richer structure, corresponding to the number distribution of DN). Inelastic collisions may also modify the effects of DM self-interactions on halo structure, especially at short distance scales. In addition, as we discuss in Chapter 3, there are a range of possible consequences for the capture of DN by astrophysical objects as well, from ejection by de-excitations, through to fusions leading to a very dense DN core.

Finally, the discussion here has intentionally been as model-independent as is practical, investigating idealised versions of the behaviour that classes of models can display. The physics is inspired by that observed in the SM sector, with the simple, but important, change that the Coulomb barrier is removed. Although the example of the SM reassures us that a sufficiently complicated model can realise the physics we discuss, it would be interesting to investigate, along the lines of [75, 80, 139], specific simple toy models which realise all or some of the features discussed in this Chapter. As with the SM, we would expect there to be additional features in the dark nuclear spectroscopy and interaction cross sections, e.g. due to shell structure, on top of the general scaling behaviour of nuclear properties that we have utilised. In addition the extra hidden sector states required (to mediate binding forces, carry away de-excitation energy, etc) beyond the dark nucleon itself can be relevant for astrophysical phenomenology and constraints. In particular, if some of these states have masses $\lesssim 100\,\mathrm{MeV}$, there is likely to be a need for extra hidden sector states which act as dark radiation. Another avenue for further work is the possibility of symmetric DM models.

CHAPTER 3

Signatures of Large Composite Dark Matter States

In this Chapter, we consider the consequences for present-day scattering processes of the simple kind of DM compositeness discussed in Chapter 2, in which the DM states are composed of a large number, A, of constituents, forming an extended semi-uniform object, analogous to SM nuclei formed out of constituent nucleons. Models that realise such a scenario include Q-balls (non-topological solitons carrying a conserved charge) [71, 72], and the kind of Nuclear Dark Matter models that were the subject of the previous Chapter, in which dark matter is made up of bound states of strongly-interacting constituents with short-range interactions [75, 79]. Here, we do not concern ourselves with the possibly-interesting early-universe cosmology of these models (see e.g. [72, 75, 79, 140]), and simply assume that a late-time population of such states exists.

This large and extended compositeness affects elastic scattering and the associated direct detection phenomenology, as we noted in Chapter 2 and will discuss in more detail in Section 3.1. Large composite states containing A constituents can have low-momentum-transfer elastic scattering cross sections coherently enhanced by a factor as large as A^2. This case is realised if the radius of the state is not too large compared to the inverse momentum exchange relevant in direct detection scatterings. In this situation, and assuming that the mass of the composite state is $\propto A$, so the DM number density is $\propto 1/A$, the event rate at direct detection experiments will effectively be enhanced $\propto A$ for a given interaction strength between SM and DM constituents. From Chapter 2 and other studies (see e.g. [72]), large values of A ($\gtrsim 10^8$) could plausibly be realised, so the effective enhancement can be significant.

In addition, if a high enough proportion of the DM states have radii larger than SM nuclei, but not so large as to significantly suppress coherent scattering, the spatial extension of the DM states leads to a dark form factor modifying the momentum dependence of DM-SM scattering (as previously considered in [141]). In the simplest case of a scalar interaction depending only on the density, this form factor has a characteristic series of peaks and troughs, analogous to SM nuclear form factors. In direct detection experiments with sufficiently good energy resolution, these could lead to the striking signature of rises in the energy recoil spectrum. We find that significant features of this kind could be distinguished from point-like elastic scattering after the observation of only $\mathcal{O}(50)$ events, independently of assumptions about the DM halo velocity distribution. A distribution over DM sizes may average out these peaks into a smoothly-falling effective form factor, in many cases resembling that from e.g. the exchange of an intermediate-mass mediator, but multiple direct detection experiments using different SM nuclear targets would still be able to separate out the momentum dependence from halo velocity distribution effects, as with other models of dark form factors [141–145].

As we discuss in Section 3.2, large composite states also generically give rise to long-wavelength and low-energy collective excitations. We focus on the most model-independent possibility of collective density excitations. We find that they can be of sufficiently low energy to be excited in collisions with SM nuclei, leading to coherently-enhanced inelastic scattering. Although this is sub-dominant to elastic scattering in the scenarios we consider, a non-negligible fraction of events may be inelastic, and we calculate the associated form factor in the leading approximation.

As is well known, couplings to SM nuclei may also lead to the capture of DM by astrophysical objects. In Section 3.3 we argue that, while the composite nature of the DM may affect the overall capture rate, perhaps the most interesting qualitative effect is that the large local DM density inside the star, and the natural possibility of inelastic DM self-interactions, could significantly modify the DM distribution inside the star. In particular, for either dissipative collisions or fusions, there is the possibility that this process runs away to a state in which most of the captured DM lies in a single very dense configuration.[1] There may be model-dependent consequences of the energy released by inelastic DM self-interactions, which in the case of fusions could release large amounts of energy into small volumes over short timescales.

3.1 Modifications to elastic scattering and direct detection

3.1.1 Dark sector form factors

For elastic scattering between a point-like state and a spatially extended state, interacting via short-range interactions sourced by some density ρ on the extended side, the dependence on the spatial properties is summarised by the form factor

$$F(\mathbf{q}) = \int d\mathbf{r}\, e^{i\mathbf{q}\cdot\mathbf{r}} \rho(\mathbf{r}), \tag{3.1}$$

i.e. by the Fourier transform of the density. For scattering of DM states off SM nuclei, effective field theory arguments show that the scattering operator on the SM side should take on one of a restricted number of forms (see e.g. [146] for a recent comprehensive analysis). The dark sector density must have a complementary tensorial structure, but could in general be determined by any properties of the

---

[1] Since the kind of large composite states we consider require some short-range repulsive interaction between constituents, there is generally no danger of forming a black hole at the centre of the star.

state, e.g. density, spin, etc.

In the case of two spatially extended states scattering off each other, the effective density is the convolution of the separate spatial profiles, so the matrix element is found by multiplying the form factors together. Thus, the overall form factor for DM-SM scattering will be $F_N(\mathbf{q})F_D(\mathbf{q})$, where F_N and F_D are, respectively, the SM nuclear form factor and the dark sector form factor (as we will discuss below, in many experimental circumstances the SM nuclear form factor is of limited importance). The specific density determining the form factor will depend on the nature of the DM-SM interaction. For simplicity, in this Chapter we will restrict ourselves to considering the case of a scalar form factor depending only on the number density of the state, e.g. arising from the exchange of a heavy scalar mediator coupling uniformly to all of the constituents. Taking, as discussed in the previous Chapter, the composite DM states to consist of an approximately uniform density of constituent matter, a first approximation for the density is a spherical top hat function, leading to a spherical Bessel function form factor,

$$F(q) = \frac{3Aj_1(qR)}{qR} = \frac{3A(\sin(qR) - qR\cos(qR))}{(qR)^3}, \tag{3.2}$$

where R is the radius of the top hat density, and A is the total volume integral of the source across the distribution, so $F(0) = A$.

SM nuclei provide an example of this kind of roughly-constant-density state, and illustrate the kind of deviations from the top-hat form factor that might occur. Figure 3.1 shows an example of the form factor corresponding to the nuclear charge density for the particular isotope ^{70}Ge [147], as inferred from electron scattering data. Generally, and in this specific case, the first few peaks and troughs of SM nuclear form factors are well-approximated by the 'Helm' functional form

$$F(q) = \frac{3Aj_1(qR)}{qR} e^{-q^2 s^2/2}, \tag{3.3}$$

which is simply the top hat form factor modified to have a finite-width fall-off, over

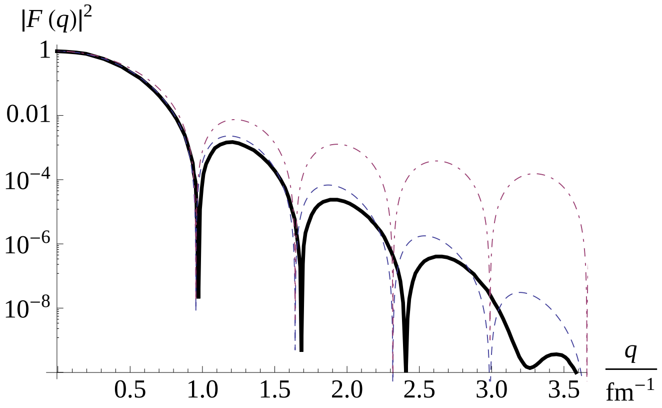

Figure 3.1: Form factor for nuclear charge density (black) of ^{70}Ge nucleus, as derived from electron scattering data [147]. Blue (dashed) curve is standard Helm parameterisation, red (dot-dashed) curve is constant-density approximation.

the 'skin depth' $s \simeq 0.9\,\text{fm}$ (comparable to the scale of the individual nucleons).

Importantly, in the case of interest to us where both a dark-sector and SM form-factor are present, if the dark states have larger radii than SM nuclei, then the first zeros, or more generally troughs, of $F_D(q)$ will occur at smaller q than for $F_N(q)$. This means that, while the SM nuclear form factor is of limited importance in most direct detection experiments, the dark form factor may have interesting structure in precisely the momentum, and thus recoil energy, ranges being probed.

3.1.2 Direct detection recap

In this section, we briefly review the standard direct detection formalism leading to the differential event rate (equation 3.7 below), mainly to establish notation for what follows. Readers familiar with this material may safely proceed to Section 3.1.3.

The differential scattering rate (event rate per unit target mass) at which incident DM particles scatter off an initially-stationary target SM nucleus, giving it recoil energy E_R, is given by

$$\frac{dR}{dE_R} = \frac{1}{m_N} \int_{|\mathbf{v}|>v_{\min}} d^3\mathbf{v}\, n_X f(\mathbf{v}) v \left.\frac{d\sigma_{XN}}{dE_R}\right|_v , \tag{3.4}$$

where m_N is the mass of the SM nucleus, $n_X f(\mathbf{v}) d^3\mathbf{v}$ is the differential number density of incident DM particles, $v_{\min}$ is the minimum velocity required to obtain recoil energy E_R, and σ_{XN} is the DM-nucleus scattering cross section. For non-relativistic elastic scattering, $v_{\min} = \sqrt{\frac{E_R m_N}{2\mu_{XN}^2}}$, where $\mu_{XN} = \frac{m_X m_N}{m_X + m_N}$ is the DM-nucleus reduced mass.

The momentum transfer in an elastic collision is $q = \mu_{XN} v \sqrt{2(1 - \cos\theta^*)}$, where θ^* is the scattering angle the centre of mass (CoM) frame. Since $E_R = \frac{q^2}{2m_N}$, we have $dE_R = \frac{2\mu_{XN}^2 v^2}{m_N}\frac{d\Omega^*}{4\pi}$, where $d\Omega^*$ is differential solid angle in the CoM frame. Referring back to the discussion of Section 3.1.1, the matrix element for scattering at angle θ^* will depend on the momentum transfer $\mathbf{q}$, and possibly also on the velocity $\mathbf{v}$. Treating isotropic, velocity-independent scattering to start with, and writing $\frac{1}{4\pi}\sigma_{XN}(q) \equiv \frac{d\sigma}{d\Omega^*}$, we have

$$\left.\frac{d\sigma_{XN}}{dE_R}\right|_v = \frac{m_N}{2\mu_{XN}^2 v^2}\sigma_{XN}(q). \tag{3.5}$$

So, under the assumption of velocity-independent scattering, we can factor the differential scattering rate as

$$\frac{dR}{dE_R} = \left(\int_{|v|>v_{\min}} d^3v \, \frac{f(v)}{v}\right) \frac{n_X}{2\mu_{XN}^2}\sigma_{XN}(q) \equiv g(v_{\min}) \frac{n_X}{2\mu_{XN}^2}\sigma_{XN}(q). \tag{3.6}$$

Altering notation somewhat from Section 3.1.1, we can write $\sigma_{XN}(q) = \sigma_{XN} F_N(q)^2 F_X(q)^2$, where σ_{XN} is the zero-momentum-transfer cross section (including any coherence enhancement), so that $|F_N(0)| = |F_X(0)| = 1$.

The scattering rate is usually expressed in terms of the DM scattering cross section with nucleons, instead of with full nuclei. For dimension-6 interactions between the DM constituents and SM quarks/gluons, the zero-momentum-transfer scattering cross section goes as $|C|^2 \frac{\mu^2}{\Lambda^4}$, where C is the coherence enhancement factor, and Λ is the suppression scale associated with the interaction. Here, C is the product of the integrated densities relevant to the microscopic interaction for the SM nucleus and the DM state, which we take to be simply the respective nucleon

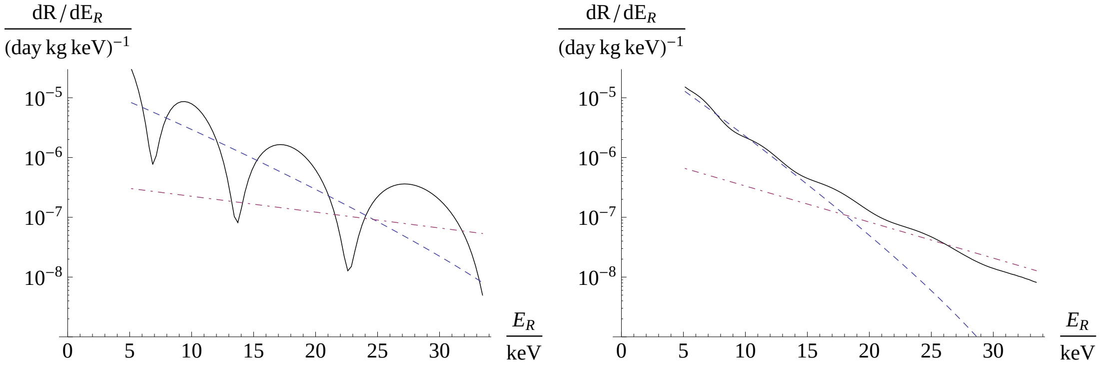

Figure 3.2: Recoil energy spectrum (black, solid curves) for Bessel-function form factor, radius 50 fm, with DM velocity distribution as given by Standard Halo Model [148], assuming *Left:* Germanium detector target, with Gaussian energy response ($\sigma(E) = \sqrt{0.3^2 + 0.06^2 E/\,\mathrm{keV}}\,\mathrm{keV}$), and *Right:* Xenon detector target, with Gaussian energy response ($\sigma(E) = 0.6\,\mathrm{keV}\sqrt{E/\,\mathrm{keV}}$), assuming 5 keV energy threshold for both. The DM state is taken to be composed of 3×10^6 constituents, each of mass 20 GeV, with constituent-SM nucleon cross section of 2×10^{-13} pb. For comparison, blue (dashed) curves show energy recoil spectrum for a 20 GeV WIMP, red (dot-dashed) for a 1 TeV WIMP, both with $\sigma_{Xn} = 10^{-9}$ pb. Energy response functions are taken from projections for future experiments in [145].

numbers. Thus $\sigma_{XN} = \frac{|C_N|^2}{|C_n|^2}\frac{\mu_{XN}^2}{\mu_{Xn}^2}\sigma_{Xn}$, where μ_{Xn} is the DM-nucleon reduced mass, and so [2]

$$\frac{dR}{dE_R} = g(v_{\min})\frac{n_X}{2\mu_{Xn}^2}\frac{|C_N|^2}{|C_n|^2}\sigma_{Xn}F_N(q)^2F_X(q)^2. \tag{3.7}$$

3.1.3 Coherent enhancement of scattering rates

With the assumptions made in the previous section, the zero-momentum transfer cross section between a DM state with A constituents and a SM nucleus with N constituents is $\sigma_0 \sim A^2 N^2 \frac{\mu_{XN}^2}{\Lambda^4}$. Taking the mass of the DM state to be $\propto A$, the DM number density is $\propto \frac{1}{m_{\rm DM}} \propto \frac{1}{A}$, assuming temporarily that all of the DM is of the same size. So, the overall scattering rate in direct detection experiments will, for $m_{\rm DM} \gg m_N$, be $\propto A$ for fixed SM-constituent interactions. This is true if the DM radius R is small enough that typical momentum transfers do not probe $qR \gtrsim 1$ — otherwise, the scattering rate is suppressed by the DM form factor, as

---

[2] This equation describes what a detector with perfect energy resolution would see. If a detector has some response function κ such that the differential rate to detect events with true energy E_R, occurring at rate R, at measured energy E_R', is $R\kappa(E_R, E_R')dE_R'$, then the differential rate for measured events is $R_d(E_R) = \int dE_R'\,\kappa(E_R, E_R')\frac{dR}{dE_R'}$.

discussed in Section 3.1.1. While, as discussed in Section 3.1.4, there might be some number distribution over DM states with different radii, if the mass distribution and scattering-rate distributions are confined to a small range in logarithmic size, then the $\propto A$ enhancement will hold approximately.

Figure 3.2 shows an example of the direct detection recoil energy spectra resulting from a scenario of this kind, corresponding to DM particles with a Bessel-function form factor of radius 50 fm. These are compared to the recoil spectra for standard momentum-independent (i.e. $F_D = 1$) WIMP scattering. Note that the constituent-SM nucleon cross section required in the composite model is much smaller than that required in WIMP models giving approximately the same event rates. An additional point is that the much better energy resolution expected in solid-state experiments would enable them to resolve the peaks and troughs of a dark form factor corresponding to much larger radii than for liquid-phase (e.g. Xenon) experiments.

The possible $\propto A$ enhancement means that, for a given direct detection event rate, the expected production of lighter single constituents in SM processes in colliders is reduced. For the example of DM coupling through the Higgs portal, the strongest collider constraint for DM states with $m_X < m_h/2$ comes from the Higgs invisible width. As described in [149], a bound of $< 10\%$ on the invisible branching ratio of the Higgs puts constraints on the DM-Higgs coupling a factor of a few better than current direct detection experiments for DM masses a small factor lower than $m_h/2$. Thus, only a modest relative suppression of collider rates vs direct detection rates is needed to render the direct detection bounds more constraining. Taking the example in Figure 3.2, with DM constituents of mass 20 GeV each having a nucleon scattering cross section $\sigma_n = 2 \times 10^{-13}$ pb, we would require Higgs invisible width bounds of $\sim 10^{-5}$ (below the SM level) to be competitive with current direct detection experiments.

3.1.4 Recoil spectrum from size distribution

The previous sections considered a dark form factor arising from DM particles having a single, common size. However, in many models of large composite states, the cosmological process through which a population of these states arises generates a distribution over multiple sizes, which would lead to a smeared-out signature in energy recoil spectra.

For dark matter consisting of a set of states X_i, the recoil spectrum for elastic scattering will be

$$\frac{dR}{dE_R} = F_N(q)^2 \sum_i g_i(v_{\min}(\mu_{i,N})) \frac{n_i}{2\mu_{i,n}^2} \frac{|C_i|^2}{|C_n|^2} \sigma_{i,n} F_{D,i}(q)^2, \tag{3.8}$$

where the subscripted quantities are those of equation 3.7 for each species X_i. In the specific case of a spectrum of related states, this may simplify somewhat. Absent astrophysical self-interactions (see Section 3.3.1), all of the states may be expected to have the same velocity distribution, i.e. $g_i = g$. From $\sigma_n \sim |C|^2 \frac{\mu_{Xn}^2}{\Lambda^4}$, we expect the $\mu_{i,n}$ dependence to cancel, and additionally, if all of the states are heavy ($m_i \gg m_N$), then $\mu_{i,N} \simeq m_N$, so we can factor out the g dependent term fully. Overall,

$$\frac{dR}{dE_R} \simeq \frac{n_X}{2m_n^2} F_N(q)^2 g(v_{\min}) \frac{|C|^2}{|C_n|^2} \sigma_n \sum_i \frac{n_i}{n_X} \frac{|C_i|^2}{|C|^2} F_{D,i}(q)^2 \tag{3.9}$$

$$\equiv \frac{n_X}{2m_n^2} F_N(q)^2 g(v_{\min}) \frac{|C|^2}{|C_n|^2} \sigma_n F_D(q)^2, \tag{3.10}$$

where $n_X \equiv \sum_i n_i$, and we have replaced the sum over individual states with a single effective form factor, choosing C appropriately so that $F_D(0) = 1$.

Figure 3.3 shows the effect of a distribution over DM states of the kind considered in Chapter 2. The sum over different sizes corresponds to adding together differently scaled form factors, which smooths out the troughs of the Bessel-function form factor. In this case, we end up with a form factor which is similar to that

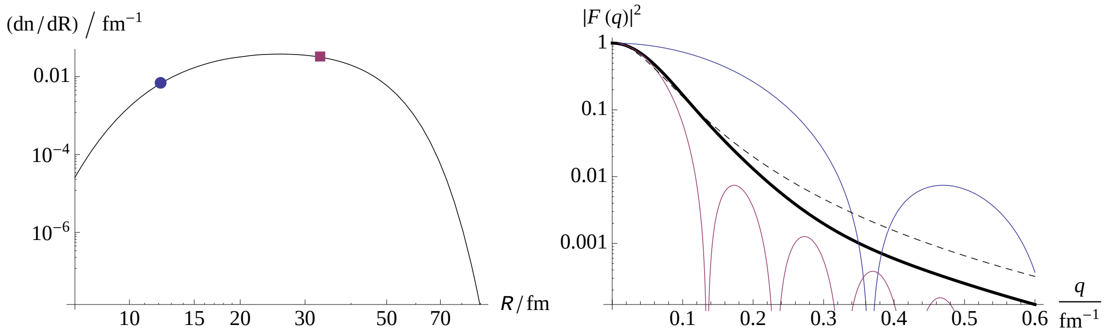

Figure 3.3: *Left:* Example (non-dimensionalised) number distribution of DM states arising from nucleosynthesis-type process (from Chapter 2). *Right:* form factors for DM sizes corresponding to points on left-hand plots (upper curve to blue circle, lower curve to red square), and (black) effective form factor for whole number distribution. Dashed line shows form factor for light mediator particle, $F(q) \propto 1/(q^2+m^2)$, with $m = 16\,\mathrm{MeV}$.

obtained from the exchange of a light mediator particle, $F(q) \propto \frac{1}{q^2+m_\phi^2}$, but arising entirely from contact interactions, without the need for a light state.[3] For a given DM velocity distribution, this kind of dark form factor gives an energy recoil spectrum with a shape different from that of standard momentum-independent scattering, falling off more slowly at high energies than a low-mass WIMP, and more quickly at low energies than a higher-mass one. In the next section, we discuss how such form factors could be distinguished from momentum-independent scattering.

3.1.5 Dependence on DM velocity distribution

From the definition in equation 3.6 of $g(v_{\min}) = \int_{|v|>v_{\min}} d^3v \frac{f(v)}{v}$, it is clear that, by choosing $f(v)$ appropriately, we can make g any non-decreasing function of

---

[3] While it is possible that a model with an intermediate-mass mediator would have additional phenomenology distinguishing it from the case of large composite DM, this would not have to be the case. Though a light mediator will give rise to self-interactions between galactic DM particles, for heavy (and thus dilute) DM these will not be frequent enough to have detectable effects on halo shapes. The direct detection event rate is set by the product of the squared couplings for the SM and the dark sector, so by making the dark sector coupling large, we could make the required SM coupling very small. Current direct detection experiments are sensitive enough that any future signals would imply a minimum value of the SM coupling small enough to be significantly below any direct production constraints. Of course, the SM coupling may be above this minimum if the dark sector coupling is also small, so direct production signals are not ruled out. Also, as discussed in Chapter 2, direct bounds on the SM couplings of light ($m \ll 100\,\mathrm{MeV}$) states generally imply that they cannot lose any initial cosmological energy density they have to the SM sufficiently fast (except possibly to neutrinos), requiring the introduction of additional light hidden sector states that persist to the present day.

$v_{\rm min}$ (with the physical constraint that it must fall off very fast past $v_e + v_{\rm esc}$, where v_e is the velocity of Earth relative to the Galactic rest frame, and $v_{\rm esc}$ is the Galactic escape velocity at the position of the Earth). Although the Standard Halo Model, which posits a Maxwell-Boltzmann DM velocity distribution, is commonly assumed, it is highly plausible that the DM velocity distribution at Earth differs from this, perhaps significantly.[4]

This has the consequence that, for elastic scattering, the energy recoil spectrum can be anything of the form $F_N(q)^2 F_X(q)^2$ multiplied by a non-increasing distribution, as discussed in [153]. So, even though the energy recoil spectrum for the dark form factor looked different from that for a WIMP *assuming the same DM velocity distribution*, by changing the velocity distribution we could make a WIMP mimic the (averaged) form factor spectrum, since this is decreasing with E_R.

However, if we have data from multiple experiments, each of which uses a different type of SM target nucleus, this degeneracy can be lifted. On the assumption that there is no dark form factor, the event distributions (once we have compensated for the different target nuclei) with respect to $v_{\rm min}$ should be the same for each of the experiments [154–158] — any disagreement indicates the presence of some extra effect. For a dark form factor, since $q(v_{\rm min}) = 2\mu_{XN} v_{\rm min}$, changing μ_{XN} by changing m_N will change the range of $F_D(q)$ that we sample (because the DM mass is assumed to be comparable or larger than the mass of the SM target nucleus). Ref. [145] performs a multi-target analysis along these lines, considering models which include DM coupling via a light mediator, which as noted above can give a very similar form factor to that obtained via averaging Bessel-function form factors. They consider the case of a $F(q) \propto q/(q^2 + m_\phi^2)$ form factor, as well as a $1/q^2$ form factor. In particular, they consider a situation with Xenon, Germanium, and Neon detectors. It is shown that, with order 100 events observed

---

[4] Simulations of dark halo formation indicate that non-Maxwell-Boltzmann velocity distributions may generically arise [150], and also suggest the possibility of a co-rotating dark matter disc [151], along with sub-structure including cold streams [152].

in each detector, a DM signal arising from a model with a form factor $F(q) \propto 1/q^2$ and 1 TeV DM mass is incompatible at 3σ with a form factor $F(q) \propto 1/(q^2 + m_\phi^2)$ for $m_\phi \gtrsim 20\,\mathrm{MeV}$. Since a DM model with no form factor corresponds to the limit $m_\phi \to \infty$ this is also excluded. Though we have not performed a detailed analysis, we believe that broadly similar results should apply to the case of an intermediate-mass mediator form factor, $F(q) \propto 1/(q^2 + m_\phi^2)$.

3.1.6 Detectability of a rising energy recoil spectrum

While Sections 3.1.4 and 3.1.5 have considered the situation of a distribution over DM sizes, the more striking scenario of DM states being concentrated around a single size, giving rise to peaks and troughs in the energy recoil spectrum as per Figure 3.2, has qualitatively different detectability in direct detection experiments. As described in the previous section, the energy recoil spectrum for elastic scattering can be anything of the form $F(q)^2$ multiplied by a non-increasing distribution. While this allows non-increasing sections of an energy recoil spectrum to be explained by a combination of form factor and DM velocity distribution, any rises in the spectrum must come from the form factor (or from the presence of inelastic scattering). Though summing over multiple Bessel-function widths will generally smooth out the individual peaks into a falling distribution, if the particle sizes were clustered mostly around a particular value,[5] then the troughs/peaks of such an effective form factor could give a rising recoil spectrum. Assuming a detector has sufficiently good energy resolution so at not to smooth out the troughs in the underlying recoil spectrum, it will be possible, with sufficiently many events, to rule out point-like elastic scattering. Furthermore, if both the falling and rising parts of a trough were visible, this would be a clear sign of a more complicated momentum-dependent form factor, or of some combination of inelastic scattering modes.

---

[5] For example, due to the binding energy per constituent reaching a maximum value at some size, and decreasing after that (as for iron in the SM), rendering larger states unstable to fission.

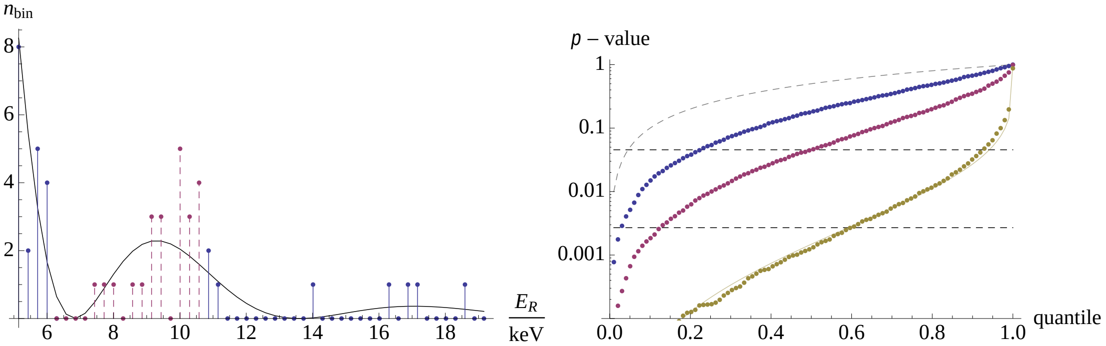

Figure 3.4: *Left:* Energy recoil spectrum (black) for a Bessel-function form factor corresponding to radius 50 fm, with other parameters as per left-hand plot of Figure 3.2. Blue points (solid lines) are a particular sample of 50 events from this distribution, binned with an energy width of 0.3 keV. Red points (dashed lines) show the interval of points that is worst fit by a non-increasing distribution (see text). The p-value for the test described in Appendix A.4 is 0.005. *Right:* Cumulative distribution functions (CDFs) for p-value from test described in Appendix A.4, for 30 samples (blue), 50 samples (red), and 100 samples (yellow). Grey (dashed) curve shows the CDF for a uniform underlying distribution. The upper and lower dashed lines shows the p values corresponding to 2σ and 3σ significance for rejecting the hypothesis of a non-increasing distribution.

We can test whether a given set of events came from a non-increasing distribution by locating the energy interval with the 'worst' bias towards its high-energy end — here measured simply by the average energy of the events — and asking what the probability is that a given sample from a candidate non-increasing distribution would have an interval that extreme (explained in more detail in Appendix A.4). Figure 3.4 displays the results of applying this test to simulated data from a model with a Bessel-function dark form factor, scaled so that a number of the peaks/troughs are visible in the energy recoil spectrum. As illustrated, around 12 expected events in the most significant rising section, corresponding here to around 50 events overall, are sufficient to obtain a 2σ exclusion of the non-increasing hypothesis in the majority of cases. While a realistic analysis would need to take into account the distribution of background events and other issues, this illustrates that relatively few events from only a single detector may suffice to give very interesting physical information about dark matter properties.

3.2 Low-energy excitations & inelastic scattering

3.2.1 Properties of low-energy excitations

Another feature generic to large composite states is the presence of low-lying modes, leading to the possibility of inelastic scattering in which these modes are excited. Such modes can be broadly characterised as either of 'single-particle' or 'collective' type. We are most interested in the collective modes since, as we will discuss, their excitation amplitudes can be coherently enhanced compared to the single-particle excitations, and thus can dominate the inelastic scattering rate if they are of low enough energy to be excited.

There are a number of forms such collective excitations could take. The simplest and most generic type of collective excitations are simply vibrational modes of either the bulk or of the surface of the large composite state. Alternatively, if the constituents have spins, moments, or other intrinsic properties, then collective oscillations of these properties, such as spin waves, can occur. In addition, if the ground state is not spherically symmetric, so the composite state is deformed in shape as happens for large SM nuclei, then there will be low-lying rotational modes as well. For definiteness, in this work we will focus on the inelastic scattering involving the most universal and model-independent of these collective modes, namely, the surface and bulk vibrational modes that are of long wavelength compared to the scale of the individual constituents.

For large composite states consisting of roughly uniform 'nuclear matter', the lowest-energy density waves will generally be surface waves, i.e. volume-preserving oscillations of the 'nuclear surface' [159]. The reason for this is that the energy of the lowest bulk compressional excitations is set by the speed of sound for such waves, $c_c \sim \sqrt{\frac{K}{\rho}}$, where K parameterises the compressibility of the nuclear material, and ρ is its density. Taking into account that the lowest possible wavenumber is $k \sim 1/R$, the energy of the low-lying compressional excitations is given by

$$\delta E_c \sim \sqrt{\frac{K}{\rho}}\frac{1}{R} \ . \tag{3.11}$$

On the other hand, the speed of volume-preserving surface capillary waves is set by $c_s \sim \sqrt{\frac{\sigma k}{\rho}}$, where σ is the surface tension (this also holds in relativistic hydrodynamics [160]), so the energy of the low-lying surface excitations is given by

$$\delta E_s \sim \sqrt{\frac{\sigma}{\rho}}\frac{1}{R^{3/2}} \ . \tag{3.12}$$

Using the facts that $R \sim A^{1/3} R_1$, where R_1 is the length scale of a single constituent, and that both the surface tension and bulk compressibility are set by the same underlying interaction strength between the basic constituents so we have $\sigma \sim R_1 K$, leads to

$$\frac{\delta E_c}{\delta E_s} \sim A^{-1/6} \ . \tag{3.13}$$

Thus for large A the energy of the bulk compressional modes is well separated from the lower-lying surface modes.

We now summarise the dynamics of the surface modes more quantitatively. Classically, for small-amplitude surface waves of a homogeneous, incompressible, sharp-edged fluid droplet, we have $\rho(r, \theta, \phi)$ constant inside $R'(\theta, \phi, t)$ and zero outside, with

$$R'(\theta, \phi, t) = R\left[1 + \sum_{l\geq 2} \sum_{m=-l}^{l} \alpha_{lm}(t) Y_{lm}(\theta, \phi)\right] , \tag{3.14}$$

for amplitude coefficients $\alpha_{lm}(t)$. The $l = 1$ modes are removed as they correspond to oscillations of the CoM position, while the $l = 0$ mode is removed as it is just the monopole compression oscillation.[6] The total Hamiltonian of the surface

---

[6] If the amplitude of the surface waves were not small then volume-preserving oscillations would require $\alpha_{00} = -\sum_{l\geq 2,m} |\alpha_{lm}|^2$, but this constraint can be ignored at leading order in the α_{lm}.

excitations is

$$H = \frac{1}{2} \sum_{\substack{l \geq 2, \\ m=-l,\ldots,+l}} \left(B_l \left| \dot{\alpha}_{lm}(t) \right|^2 + C_l \left| \alpha_{lm}(t) \right|^2 \right) , \tag{3.15}$$

where $B_l = \rho R^5 / l$ and $C_l = (l-1)(l+2) R^2 / \sigma$ are the 'mass' and 'stiffness' parameters of each mode.

Quantising this system leads to each mode being an independent quantum harmonic oscillator. The mode frequencies, ω_{lm}, of the oscillations are independent of the azimuthal spherical harmonic parameter m and are given by [160]

$$\omega_l = \sqrt{\frac{C_l}{B_l}} = \left(\frac{l(l+2)(l-1)\sigma}{R^3 \rho} \right)^{1/2} . \tag{3.16}$$

The overall excitation energy spectrum $\Delta E_{\{n_l\}} = \sum_{l \geq 2} n_l \omega_l$ is thus set by the occupation numbers n_l of the $(2l+1)$-fold-degenerate l-modes. It will be important for our discussion of the coherent excitation probability of these modes that the simple harmonic oscillator-like wavefunctions associated to each mode are characterised by a length scale, $R\epsilon_l$, where the dimensionless parameter ϵ_l is given by

$$\epsilon_l = \frac{1}{\sqrt{2 B_l \omega_l}} . \tag{3.17}$$

(For an individual mode with occupation number $n_l \gg 1$ the corresponding classical amplitude of oscillation simply scales as $|\alpha_l| \sim \epsilon_l \sqrt{n_l}$.) In terms of the underlying parameters of the composite state

$$\epsilon_l \propto A^{-7/12} \left(\frac{\beta}{m_1} \right)^{-1/4} , \tag{3.18}$$

where $\beta \sim \sigma R_1^2$ is the energy associated to surface tension, and m_1 is the single-constituent mass. As discussed in [161], the hydrodynamic values of B_l and C_l can differ by factors of $\mathcal{O}(10)$ from those obtained experimentally for SM nuclei, due to the effects of shell structure etc. However, the hydrodynamic approximation should give a good qualitative guide to the properties of the low-lying modes of large composite states.

Finally, as mentioned above, as well as collective modes there may also be modes corresponding to the excitation of 'single constituents'. If the interior of the state consists of degenerate fermionic matter, then excitations which move a state from just below the Fermi surface, through a small change in momentum $\mathbf{q}$ approximately tangential to the surface, will look like quasi-particles of energy $\mathbf{q}^2/(2m_*)$, where the quasi-particle mass m_* will often be of order the constituent mass [162]. Since the smallest allowed momentum change is $q \sim 1/R$, the lowest-energy quasi-particle excitation will have energy $\omega \sim \frac{1}{2R^2 m_*} \sim A^{-1/3}/R$, so for large A will be of lower energy than the collective surface modes. However, as discussed in the next section, in the regimes of interest in this Chapter, the cross sections for exciting them are much lower. Additionally, the properties of these modes are model-dependent — for example, pairing interactions between constituents could lead to superfluidity, as arises in forms of SM nuclear matter.

3.2.2 Inelastic scattering form factors

The presence of the low-lying modes means that even low-velocity scattering processes may have sufficient energy to be inelastic. In particular, scattering off the long-wavelength collective modes, since these involve all of the constituents, will be coherently enhanced as for elastic scattering, and have their own momentum-dependent form factors.

Generally, this form factor can be calculated from the overlap of initial- and final-state wavefunctions. As derived in Appendix A.2, if the scattering occurs through a scalar contact interaction with the constituents of the DM state, then (returning to the notation of Section 3.1.1) the form factor for inelastic scattering into a one-phonon surface mode of angular momentum number l is, as given in equation A.14,

$$F(q) = \frac{3A}{\sqrt{4\pi}} i^l (2l+1)^{1/2} \epsilon_l j_l(qR) \tag{3.19}$$

(as compared to equation 3.2 for elastic scattering), where ϵ_l is the natural amplitude associated with oscillations in that mode. This result is correct to first order in ϵ_l, and valid for $qR \lesssim 1/\epsilon_l$ (beyond that, the wavefunction overlap can be computed numerically). Excitations of multiple phonons are associated with further factors of ϵ_l. Comparing elastic to inelastic scattering, we see that the latter has form factors corresponding to higher spherical Bessel functions, and is suppressed by powers of the natural amplitude of the surface modes; as per equation 3.18, this is parametrically small for large A.

The cross sections for scattering off single-particle excitations add incoherently, giving $\sigma \propto A$. There may also be further suppression factors. The case of degenerate fermionic matter may be well-approximated by scattering off a Fermi gas of non-interacting quasi-particles — as discussed in Appendix A.3, this is, for low momentum transfers, strongly suppressed by degeneracy factors. Generally, incoherent scattering should only be significant for momentum transfers comparable to the Fermi momentum (and energy transfers comparable to the Fermi energy), or for very large composite states where scattering from collective modes is highly suppressed (Appendix A.3).

3.2.3 Inelastic recoil spectra

If collisions are inelastic — say, the DM state is excited from m_X to $m_X + \delta$ — then the minimum velocity for which we can obtain a given recoil energy is [7]

$$v_{\min} = \frac{1}{\sqrt{2 m_N E_R}} \left(\frac{m_N E_R}{\mu_{XN}} + \delta \right) \ . \tag{3.20}$$

We have $dE_R = \frac{2pp'}{m_N} \frac{d\Omega^*}{4\pi}$, where p and p' are the initial and final momentum in the CoM frame. The final state phase space available is also proportional to p', so the

---

[7] Equation 3.20 is accurate up to multiplicative correction of size at most $\sim \sqrt{\delta/M}$ — this always gives a good approximation, since $\delta < \frac{1}{2}\mu_{XN} v_{\max}^2$ is required for any excitations to occur, and galactic escape velocity is highly non-relativistic.

differential rates for elastic and inelastic scattering are related by

$$\frac{d\sigma_i}{dE_R} = \frac{d\sigma_e}{dE_R}\frac{|\mathcal{M}_i|^2}{|\mathcal{M}_e|^2}\ , \tag{3.21}$$

where $\mathcal{M}_\rceil$ and $\mathcal{M}_\rangle$ are the matrix elements for elastic and inelastic scattering respectively, while σ_e and σ_i are the corresponding cross-sections. Aside from differences in the momentum-dependence of the matrix elements, giving different form factors, the main qualitative difference from elastic scattering is that $v_{\min}$ is no longer monotonically increasing with E_R, instead having a minimum at $E_R = \delta\mu_{XN}/m_N$. This is in contrast to elastic scattering, where the fact that that $v_{\min}$ is monotonically increasing had important consequences (see Sections 3.1.5 and 3.1.6) for data analysis.

As per above, we generically expect large composite states to have low-energy excitations, which may be excited by scattering with SM nuclei. The energy recoil spectrum will then be a sum over the spectra for scattering into each of these states (including the ground state, which gives elastic scattering). Labelling the states by λ,

$$\frac{dR}{dE_R} = \frac{n_X}{2\mu_{Xn}^2}\sigma_{Xn}F_N(q)^2\sum_\lambda g(v_{\min,\lambda}(E_R))\frac{|C_\lambda|^2}{|C_n|^2}F_{D,\lambda}(q)^2, \tag{3.22}$$

where $\frac{C_\lambda}{C_n}$ gives the ratio of matrix elements (c.f. equation 3.7), and the $F_{D,\lambda}$ have a common normalisation such that elastic scattering has $F(0) = 1$.

Figure 3.5 shows an example of the energy recoil spectrum arising from a uniform-density composite state of the kind discussed in Section 3.2.1, in the regime where elastic scattering, and inelastic scattering into the first few surface modes, are the dominant effects. Due to the relative suppression of inelastic modes, from both form factor effects and the small amplitude of surface oscillations, elastic scattering generally dominates in such scenarios.

The above assumed that the DM particles are dominantly in the ground state. If de-excitation times are long enough, there is a (model-dependent) possibility

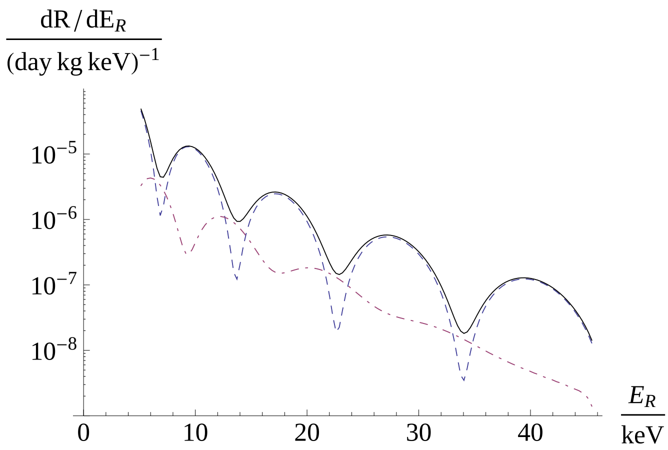

Figure 3.5: Energy recoil spectrum (Germanium target) for a spherical DM state with parameters as per Figure 3.2, incorporating elastic scattering and inelastic excitations of surface modes (black). Blue (dashed) and red (dot-dashed) curves show contributions from elastic and inelastic scattering respectively. The energy of the first surface mode is taken to be 28 keV, so a number of modes contribute at higher recoil energies, flattening out the inelastic recoil spectrum. The amplitude of the inelastic modes is set a factor $\sim$ 10 above the hydrodynamic estimate from Section 3.2.1, for illustrative purposes. Note that the form factor for the first excited mode is 90 degrees out of phase from that for elastic scattering — this effect can be seen in inelastic SM-SM scattering, e.g.F̃igure 1 of [161].

that there may be a significant cosmological population of excited DM states, altering the inelastic scattering phenomenology.

3.3 Astrophysical capture

In addition to potentially being visible in direct detection experiments, interactions between DM and SM matter may also lead to the capture of DM by astrophysical objects, the most interesting generally being various kinds of stars. Once enough DM has accumulated inside the star, then either self-interactions among the DM (annihilations, self-scattering, etc.), or more complicated DM-SM interactions, may in some models lead to observable alterations of stellar properties. For definiteness, we consider the case of asymmetric dark matter, in which DM may build up in the star without being destroyed through annihilations.

For spatially-extended DM states, the possibility of large cross sections for inelastic DM-DM interactions may give rise to modifications of the distribution of captured DM inside the star, analogously to the possibility of effects on astrophysical halo shapes mentioned in Chapter 2. In models with large velocity kicks after exothermic collisions, these could take the form of ejecting captured DM from the star, as discussed e.g. in [79]. Alternatively, other models could lead to the contraction of the captured DM distribution, potentially all of the way down to a very dense configuration at the centre of the star. Since we have been considering composite states composed of similar constituents, some kind of repulsive self-interaction countering the attractive binding forces is already required in such models, and will generally remove the danger of such a DM configuration collapsing into a black hole.[8] In the absence of any further dynamics, there are no obvious externally observable consequences of a high-DN-density central region. In particular, the release of binding energy from DN fusions will have no significant effect on the star—for symmetric DM, almost all of the DM captured by the star can annihilate with no observable heating, and we are only injecting a small fraction of this energy. However, in the case of run-away fusions, there may be inelastic collisions between extremely large composite states, which could result in the release of large amounts of energy, in small volumes and on rapid timescales. If some of these de-excitation products couple to the SM strongly enough, the SM energy injection resulting from these processes may have consequences, particularly in meta-stable systems such as white dwarfs.

The composite nature of the DM may also affect the initial capture rate, through the momentum-dependence of scattering cross sections. For $kR \lesssim 1$, where $k \sim m_N v_{\rm esc}$ is the typical momentum of SM scatterers in the initial collision, the momentum dependence will not have a significant effect. For $kR \gtrsim 1$, the (elastic) capture rate will be suppressed by $\sim (kR)^{-2} \min\left(1, \frac{1}{m_X m_N R^2 \overline{v}^2}\right)$, where $\overline{v}$ is the typical DM halo velocity (this replaces the usualkinematic $\min\left(1, \frac{m_N v_{\rm esc}^2}{m_X \overline{v}^2}\right)$ factor). As an example, if we suppose that the Sun (escape velocity $0.002c$) has $kR \simeq 1$, then capture in white dwarfs ($v_{\rm esc} \sim 0.02c$) is suppressed by a factor of

---

[8] As may occur in models of very heavy fundamental ADM [163, 164]

$\sim 2\times 10^{-3}$, and in neutron stars ($v_{\rm esc} \sim 0.7c$) by $\sim 5\times 10^{-6}$, compared to standard elastic scattering (for white dwarfs, the SM nuclear form factor is also important). These suppressions mean that inelastic scattering may be the dominant capture process, though we leave the investigation of this to future work.

3.3.1 Self-interactions of captured dark matter

One possible effect of large DM self-interaction cross sections is to increase the capture rate, in that incoming DM can scatter off already-captured DM as well as off SM nuclei in the star. However, for heavy DM, and in locations of reasonable astrophysical DM density, it is generally hard to accumulate enough captured DM to have any significant effect on the overall capture rate. Supposing that the star has effective capture cross section A_s for DM particles streaming through it, the total number of DM particles it captures in its lifetime is $N_X \sim A_s t_s v n_X$, where n_X is the local DM number density and v is the characteristic relative velocity (of order galactic orbital velocities, $\sim 220\,\mathrm{km\,sec^{-1}}$). Writing the DM self-scattering cross-section as σ_{XX}, the total cross sectional area for DM-DM scattering is at most

$$\begin{aligned} A_X &= \sigma_{XX} N_X \sim (\sigma_{XX}/m_X) t_s v \rho_X A_s & (3.23)\\ &\simeq A_s \left(\frac{\sigma_{XX}/m_X}{\mathrm{barn/\,GeV}}\right) \frac{v}{220\,\mathrm{km\,sec^{-1}}} \frac{t_s}{5\,\mathrm{Gyr}} \frac{\rho_X}{0.3\,\mathrm{GeV\,cm^{-3}}}\ . & (3.24)\end{aligned}$$

For elastically-scattering DM with velocity-independent self-scattering cross section, the observational limit on the self-scattering cross section is $\sigma_{XX}/m_X \lesssim 1\,\mathrm{barn/\,GeV}$ (see Section 1.1.4). That A_X can be of order A_s for this value means that there are possible dark matter models in which self-capture is significant (see e.g. [165, 166]). However, as per Section 2.3.1, for large composite DM states, the fact that $\sigma_{XX}/m_X \propto m_X^{-1/3}$ for uniform matter means that large states generally stand little chance of having significant self-capture. Recapitulating equation 2.18, evaluating σ_{XX}/m_X for a composite state of interior density ρ_b, and constituent number A,

$$\frac{\sigma_{AA}}{m_A} \simeq \frac{0.05\,\mathrm{barn}}{\mathrm{GeV}} A^{-1/3} \left(\frac{1\,\mathrm{GeV}}{m_1}\right)^{1/3} \left(\frac{1\,\mathrm{GeV\,fm^{-3}}}{\rho_b}\right)^{2/3} , \tag{3.25}$$

we see that for SM-like or heavier constituents, large composite states are well below elastic self-interaction bounds, so do not give interesting self-capture effects.

However, interactions between already-captured DM states could potentially have interesting effects. Particularly interesting are interactions which may lead to 'run-away' effects, in which the DM distribution inside the star contracts to a very dense state. This could arise either from inelastic collisions which are dissipative (i.e. some of the initial KE is lost into de-excitation products), or from fusions, which result in heavier DM states that have a correspondingly smaller equilibrium radius inside the star. In Sections 3.3.1.1 and 3.3.1.2, we will perform some approximate calculations to demonstrate the feasibility of these scenarios.

3.3.1.1 Dissipative collisions

For dissipative collisions, the dynamics are governed by the rate at which DM-DM collisions dissipate energy, versus the rate at which DM-SM collisions add it, re-thermalising the DM. As an estimate, if some fraction α of integrated phase space density for DM lies within a spatial radius r, then the rate of self-interactions is set by

$$\Gamma_{XX} \sim \sigma_{XX} n_X v_X \sim \frac{\sigma_{XX}}{r^2} \alpha N_X \frac{3}{4\pi} \sqrt{\frac{G M_\star}{R_\star^3}} \sim 10\,\mathrm{day}^{-1} \alpha \frac{A_X}{r^2} , \tag{3.26}$$

where we have taken $v_X^2 \sim \frac{GM(r)}{r}$, and A_X is as per equation 3.24. In thermal equilibrium with the SM matter in the star, the DM states would have an isothermal distribution,

$$\rho_X \sim e^{-r^2/(2r_*^2)} \quad , \quad r_* = \left(\frac{3T_\star}{4\pi G m_X \rho_\star}\right)^{1/2} , \tag{3.27}$$

where $T_\star$ and $\rho_\star$ are the temperature and density of the stellar core. Evaluating Γ_{XX} for $r = r_*$, and putting in values appropriate to the Sun,

$$\Gamma_{XX} \sim 6\,\mathrm{yr}^{-1}\alpha \left(\frac{\sigma_{Xn}/m_X}{10^{-8}\,\mathrm{pb}/\,\mathrm{TeV}}\right)\left(\frac{m_X}{\mathrm{TeV}}\right)^{2/3}\left(\frac{1\,\mathrm{GeV\,fm}^{-3}}{\rho_b}\right)^{2/3} , \tag{3.28}$$

where we have used equation A.18 for the solar capture rate, and we have replaced σ_{XX} by the geometrical cross section between two spheres of mass m_X and internal density ρ_b.[9] This interaction timescale is much less than the lifetime of the Sun. So, as long as scattering with SM particles does not counteract the increase in the local DM number density that comes about from losing energy in inelastic scatterings, it is inconsistent for a large fraction of the captured DM to have a basically-isotropic steady state phase space distribution with most of the density within a sphere of isothermal or smaller radius. Thus, if the DM-SM cross section is large enough, the DM distribution may contract down to a very dense configuration at the centre of the star.

It remains to check that SM scatterings do not re-thermalise DM fast enough to avoid this contraction. The viscous drag force on a DM state is approximately $\mathbf{f}_{\rm drag} \sim -m_N n_N v_N \sigma_{XN} \mathbf{v}_X \equiv -\gamma m_X \mathbf{v}_X$, where m_N, n_N and v_N are the mass, number density and average speed of the SM scatterers, σ_{XN} is the momentum transfer cross section between X and the scatterers, and $\mathbf{v}_X$ is the velocity of X in the thermal rest frame of the scatterers. Thus, γ gives the damping rate at which scatterings return $\mathbf{v}_X$ to the thermal distribution. For parameters relevant to the solar core,

$$\gamma \simeq \frac{m_N n_N v_N \sigma_{XN}}{m_X} \simeq 3 \times 10^{-4}\,\mathrm{yr}^{-1}\left(\frac{\sigma_{Xn}/m_X}{10^{-8}\,\mathrm{pb}/\,\mathrm{TeV}}\right) . \tag{3.29}$$

Thus, as long as each inelastic collision does not dissipate too small a fraction of the initial KE ($\sim 10^{-4}$ for the parameters in equations 3.28 and 3.29), SM-DM

---

[9] A $1\,\mathrm{TeV}$ mass sphere of this density has radius $\simeq 6\,\mathrm{fm}$, which is of the order of the inverse momentum transfer in the initial DM-nucleus collisions (for solar capture), so there will not be significant momentum suppression of the capture rate.

thermalisation will be too slow to prevent contraction. Also, since the thermalisation timescale is much less than the lifetime of the star, we do expect to contract down to isothermal densities in the first place (in particular, this means that we will lose almost all of any net angular momentum the captured DM distribution might have had initially, meaning that rotational support of the collapsing distribution will not be a worry). The same separation between self-interaction rates and thermalisation times may, for suitable parameter ranges, apply in the case of white dwarfs and neutron stars as well (however, for neutron stars there is an issue of whether thermalisation timescales are less than the lifetime of the star [167]).

3.3.1.2 Fusions

An alternative way to realise run-away contraction is for the DM states to progressively increase in mass through fusions, and correspondingly for their isothermal radius within the star to decrease. In contrast to the previous section, this scenario relies on thermalisation through SM-DM scattering being *fast* enough. It also relies on fusion cross sections being large enough, and on fusions remaining energetically favourable up to very large sizes — these features may naturally be realised in models of composite DM such as those discussed in Chapter 2.

As discussed in Appendix A.3, we expect the coherent momentum transfer cross section between DM and SM states to scale as $\sigma_{AN} \propto A^{2/3}$ for states A with $pR_A \gg 1$, where p is the characteristic momentum of the SM scatterers. Thus, $\gamma_A \simeq (A_p/A)^{1/3}\gamma_{A_p}$ for $A \gg A_p$, where A_p is the size for which the DM states are of radius $\sim 1/p$, i.e. $pR_{A_p} \sim 1$, with γ given by equation 3.29. In terms of the size A_i of states which have radius $\sim 1/p_i$, where p_i is the characteristic momentum of SM scatterers in the *initial* collision (which occurs are around the escape velocity), thermalisation is effective (assuming small enough injections of kinetic energy on the DM side) for $A \lesssim 10^{26} A_i \left(\frac{\sigma_{A_i n}/m_{A_i}}{10^{-8}\,\mathrm{pb}/\,\mathrm{TeV}}\right)^3 \equiv A_{\mathrm{th}}$. From equation 3.28, an isothermal distribution for states of size $A_{\rm th}$ has

$$\Gamma_{AA} \sim 10^{18}\,{\rm yr}^{-1}\alpha \left(\frac{\sigma_{A_i n}/m_{A_i}}{10^{-8}\,{\rm pb/\,TeV}}\right)^3 \left(\frac{m_{A_i}}{\rm TeV}\right)^{2/3} \left(\frac{1\,{\rm GeV\,fm^{-3}}}{\rho_b}\right)^{2/3} \quad , \tag{3.30}$$

If further fusions do not result in velocity kicks that substantially alter this distribution, then build-up can continue, with $\Gamma_{AA} \propto A^{-1}A^{2/3} \sim A^{-1/3}$ from number density and cross section factors respectively. Over the lifetime of the Sun, this allows $A_{\rm max} \sim 10^{83} A_{\rm th}$ for the parameters in equation 3.30 — that is, most of the DM would form into a very dense configuration.

For white dwarfs and neutron stars, we have a similar conclusion that fusions are potentially fast enough to form a very dense configuration. In these cases, the star is compact enough that even a DM distribution of radius comparable to the entire star can still have a high enough self-interaction rate for fusions to combine the majority of the DM into a dense state (though we would still need to worry about dissipating energy and angular momentum, especially in the neutron star case).

We note that the estimates in Section 3.3.1.1 and 3.3.1.2 should be viewed as rough plausibility estimates — proper investigation of these issues would require realistic modelling of the DM-DM collisions, and of the phase space distribution of DM at each stage of the process. In particular, this section has ignored the possibility that DM collision types other than fusions are important (e.g. fragmentations etc.), and also assumed that the velocity kicks imparted by fusion de-excitation products are small enough to be re-thermalised quickly. However, the point was merely to illustrate that run-away contraction is a plausible possibility.

3.4 Summary

In this Chapter, we have investigated some of the consequences that follow if a proportion of dark matter is composed of large composite states — that is, states consisting of a large number of constituents forming an extended, semi-uniform object.

The spatial extension of these objects introduces a dark form factor into scattering amplitudes. This has two effects — coherently enhancing scattering rates, as discussed in Section 3.1.3, and introducing momentum dependence, whose effects on direct detection energy recoil spectra (for DM states large compared to SM nuclei) are considered through Section 3.1. In the most visible cases, such signals may be distinguishable from elastic scattering, in a halo-velocity-independent manner, with only $\mathcal{O}(50)$ scattering events (Section 3.1.6).

Large composite states will generically have long-wavelength collective excitations, which give rise to the possibility of low-energy, coherently enhanced inelastic scattering processes, as discussed in Section 3.2. Though such processes will generally be sub-dominant in direct detection experiments (Section 3.2.3), in specific models they may have signatures, in direct detection or astrophysically.

Finally, we considered the capture of DM by stars (Section 3.3). While the presence of dark form factors and inelastic scattering may alter the capture rate, the main feature of qualitative interest that we investigated is the possibility of inelastic interactions between captured DM states having an effect on the DM distribution inside the star. Most interestingly, for plausible types of self-interactions, it appears to be possible for almost all of the captured DM to accumulate into a very dense configuration (Sections 3.3.1.1 and 3.3.1.2).

Our calculations have aimed to compute the leading, model-dependent approximations which we might expect to be valid for DM states much larger than the scale of their constituents. It would be clearly be interesting to construct and investigate specific models which realise such scenarios.

CHAPTER 4

Dark matter distributions after velocity kicks & decaying ADM

As noted in Chapters 2 and 3, an interesting possibility motivated by dark sector structure, including but certainly not limited to composite models, is that dynamics within the dark sector may result in inelastic processes among DM particles. These could take many forms, including the dissipative phenomena discussed in Sections 2.3.1 and 3.3.1.1, or exothermic interactions of the kind mentioned in Section 2.3.1.

Properly investigating the effect of such phenomena on DM distributions would generally require numerical simulations. However, it is possible to make semi-analytic estimates in many circumstances. In this Chapter, we do so for one of the simplest scenarios, in which DM particles receive a non-relativistic velocity kick, and so adopt new orbits within an *un-modified* background gravitational potential, where we also ignore the effect of any further collisions. This situation could arise either from only a small proportion of DM particles receiving velocity kicks, or from the gravitational potential dominantly being sourced by SM matter (e.g. near the Galactic centre, or inside stars). Other scenarios, such as those considered in Section 2.3.1, are also interesting, and may lead to more striking phenomenology, but would require different (and more difficult) calculations.

As an example application of these calculations, we investigate a different kind of ADM model to those considered in previous Chapters. In this class of models, some of the DM is meta-stable on cosmological timescales, so a small proportion of it decays. We assume a two-species dark matter population with a small mass splitting, in which decays of the heavier state have the lighter state's anti-particle as one of their products. This structure may arise from a dark sector with two approximately conserved quantum numbers, only the difference of which is conserved by higher-scale physics (analogously to $B-L$ in the SM). The lighter state emerges from the decay with some velocity kick, depending on the mass splitting and on the other decay products. Annihilations between the injected antiparticles and the DM population of the lighter states can then give annihilation-type indirect detection signals, which are not usually expected from ADM models. Particularly strikingly, it could almost entirely eliminate signals from small-escape-velocity systems such as dwarf galaxies, modifying the expected correspondence between events rates from these and rates from larger galactic systems.

Illustrating the kind of modifications to halo shapes such a velocity kick process may bring about, Figure 4.1 shows the post-injection distribution for galactic NFW-type halo initial conditions. As expected, a velocity kick of order the initial velocity dispersion is required to have a major effect on the final distribution — for larger velocity kicks, the central core of the distribution is significantly flattened out.

4.1 Effect of velocity kick on DM distribution

Suppose that we have a steady-state distribution of DM particles X, which we treat as collisionless, in a gravitational potential Φ. Some of these, labelled Y, are given a non-relativistic velocity kick — for example, arising from a decay with a small mass splitting. We wish to calculate the steady-state distribution of the Y population, assuming that the gravitational potential Φ is unchanged.

We could approach this in a brute-force way by sampling from a large number of

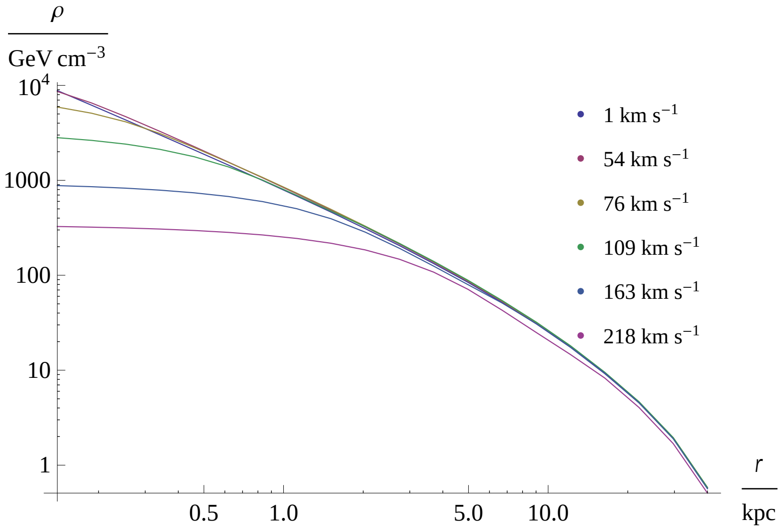

Figure 4.1: Approximation to DM profile after injection at relative velocity v_i as listed, starting from a NFW-type initial distribution with shape parameter $\gamma = 1.2$ (so $\rho \propto r^{-1.2}(1 + r/r_s)^{-1.8}$, taking $r_s = 20$ kpc). The initial distribution is taken to have isotropic velocity distribution, which implies velocity dispersion of $\sigma = 94$ km s^{-1} at $r = 1$ kpc. As described in the text, we approximate the final distribution as also having isotropic velocity distribution, which will make the larger-v_i profiles slightly less peaked than they should be.

X starting positions and velocities, sampling from the possible relative Y velocities, then calculating the resulting Y orbit and accumulating the time spent at given $\vec{x}$ and $\vec{v}$ in this orbit into the overall $\vec{x}, \vec{v}$ distribution (more sophisticated analyses such as [168] take some variation of this approach). However, we can simplify the problem slightly by assuming that the X distribution, and the gravitational potential, are both spherically symmetric, and that the X distribution is non-rotating. Although this ignores various effects, their impact should be minor (see Appendix A.6).

By the Strong Jeans Theorem [169], the steady state phase-space distribution of a system of collisionless particles moving in a spherical potential can be expressed as $f = f(\varepsilon, \vec{L})$, where ε is the binding energy and $\vec{L}$ is the angular momentum (both per unit mass). Furthermore, assuming that the $X \to Y + \ldots$ decay is spherically symmetric, the distribution of the Y in phase space must be of the form $g = g(\varepsilon, L^2)$. So, if we start out with a distribution function (DF) $f(\vec{x}, \vec{v}) =$

$f(\varepsilon, L^2)$ for the X, we can derive the 'post-injection' DF

$$h(\vec{x}, \vec{v}) = \int \mathrm{d}^3 v' K(|v - v'|) f(\vec{x}, \vec{v}') \ , \tag{4.1}$$

for the Y, where $K(\Delta v)$ corresponds to the probability of injecting with a given velocity change. In general, h will not be a steady-state distribution, as can be seen by considering e.g. a high-central-density profile with a cool core, which will be smoothed out by a large velocity boost. However, since ε and L^2 are preserved along particle orbits, the number of particles in a volume $\mathrm{d}\varepsilon \, \mathrm{d}L^2$ of (ε, L^2) space will be the same for h and for the steady-state distribution g. Then, since g depends only on ε and L^2, we can recover it from the $\mathrm{d}\varepsilon \, \mathrm{d}L^2$ density p, via $g \, \mathrm{d}V = p \, \mathrm{d}\varepsilon \, \mathrm{d}L^2$, where $\mathrm{d}V = \mathrm{d}^3 x \, \mathrm{d}^3 v$ is phase space volume. Explicitly,

$$\frac{\mathrm{d}V}{\mathrm{d}\varepsilon \mathrm{d}L^2} = \int \mathrm{d}^3 x \int \mathrm{d}^3 v \, \delta\left(\varepsilon - \left(\psi - \frac{1}{2} v^2\right)\right) \delta(L^2 - r^2 v_\perp^2) \tag{4.2}$$

$$= 2\pi \int \mathrm{d}^3 x \left(\frac{v}{\sqrt{r^2 v^2 - L^2}}\right)_{v^2 = 2(\psi(r) - \varepsilon)} \ , \tag{4.3}$$

where $v_\perp$ is the perpendicular-to-radial velocity, and $\psi(r) \equiv -\Phi(r)$ is the maximum binding energy at r. Similarly,

$$p(\varepsilon, L^2) = \int \mathrm{d}^3 x \int \mathrm{d}^3 v \, f(\vec{x}, \vec{v}) \delta\left(\varepsilon - \left(\psi - \frac{1}{2} v^2\right)\right) \delta(L^2 - r^2 v_\perp^2) \ , \tag{4.4}$$

and in particular, if the velocity distribution is everywhere isotropic ($h(\vec{x}, \vec{v}) = h(\vec{x}, |v|)$), then

$$p(\varepsilon, L^2) = 2\pi \int \mathrm{d}^3 x \left(\frac{v h(x, v)}{\sqrt{r^2 v^2 - L^2}}\right)_{v^2 = 2(\psi(r) - \varepsilon)} \ . \tag{4.5}$$

From $g(\varepsilon, L^2)$, we can find the number density $\rho(r)$ by integrating over the appropriate ranges of ε and L^2,

$$\rho(r) = \int \mathrm{d}^3 \vec{v} \, g(r, \vec{v}) = \int_{v^2 < 2\psi(r)} \mathrm{d}^3 \vec{v} \, g(\psi(r) - v^2/2, r^2 v^2 \sin^2 \theta) \ . \tag{4.6}$$

To find a plausible initial DF for X, we can assume that the velocity distribution is everywhere isotropic. This implies that the DF depends only on ε (it is said to be 'ergodic'). Starting from a number density $\rho(r)$ in a potential $\psi(r)$, there is a unique ergodic DF $f(\varepsilon)$ giving ρ [169], described by the Eddington formula

$$f(\varepsilon) = \frac{1}{\sqrt{8}\pi^2} \frac{\mathrm{d}}{\mathrm{d}\varepsilon} \int_0^{\varepsilon} \frac{\mathrm{d}\psi}{\sqrt{\varepsilon - \psi}} \frac{\mathrm{d}\rho}{\mathrm{d}\psi} \ . \tag{4.7}$$

For the figures in this Chapter, we also (for ease of implementation) make the approximation that the Y distribution g is ergodic, i.e. that it does not depend on L^2. This can be a poor approximation for large velocities, as can be seen by considering a cool, high-density centre subjected to a large velocity kick, where this results in most trajectories at large distances being approximately radial. However, for the not-too-large velocity kicks we will consider (as required for observable annihilation signals), and for the smaller-radius regions we are most concerned about, the approximation is acceptable. For example, taking the X profile to be the NFW $\gamma = 1.2$ one considered in Figure 4.1, and working out the full Y distribution function $g(\varepsilon, L^2)$ (for $\Delta v = 109 \text{ kms}^{-1}$) at some representative values, we can estimate that the error in ρ at $r = 10 r_{\text{deg}}$ (in the notation of Figure 4.8) will be at most a few percent.

4.2 Annihilation signals from ADM

Indirect detection signals of DM can arise if the DM decays or annihilates, producing cosmic rays containing high energy photons, electrons, positrons or antibaryons. Usually, the event density associated to signals of decaying DM depends linearly on the DM density n_{DM}, whereas for annihilating DM the signal has an n_{DM}^2 dependence. If astrophysical gamma-ray signals from DM were detected, then their profile on the sky would let us determine which process produced them, see e.g. [170, 171] (the propagation of charged cosmic rays is affected by galactic magnetic fields, so a signal in these channels would not be so helpful). Whilst decay signals of ADM can readily arise, see e.g. [172], in general, we do not expect late-time annihilation signals from ADM, since the symmetric component is assumed to have annihilated early on. However, if the symmetric component is later 'regenerated', this may give rise to annihilation signals. Previous proposals along these lines include slow DM-antiDM oscillations [173–176], and intermediate-time decays (in the higher DM-mass regime, e.g. [108]). Alternatively, there are scenarios in which an asymmetry plays a role in determining the DM relic density, but the DM itself is not asymmetric [84, 177, 178]. Here, we investigate the prospect of regenerating a symmetric component via decays in the low DM-mass regime, i.e. for $m_{\mathrm{DM}} \lesssim 20\,\mathrm{GeV}$.

As discussed in Chapter 1, a challenge in building viable models of ADM, which freeze out of the SM thermal bath, is obtaining a high enough annihilation cross section so that the relic density is set by the asymmetry and not by a frozen-out symmetric DM component. For this to occur the cosmologically stable states in the dark sector typically must have annihilation cross sections a factor ~ 10 times larger than the symmetric freeze-out value (which is $\sim 3 \times 10^{-26}\mathrm{cm}^3\mathrm{s}^{-1}$). Experimental limits on this scenario arise from a variety of sources. Direct searches rule out large regions of parameter space where the interaction with the visible sector is through heavy portal states that can be parameterised as effective operators, see e.g. [111, 114, 179, 180],[1] although viable models remain if the mediating states are light. Unitarity also often limits the cross sections that can be obtained in viable models. Additionally, indirect detection constraints are limiting in some regions of parameter space.

Generally, the strongest astrophysical constraints on the DM annihilation cross section (if the population is entirely symmetric) are close to or below the lower cross-section bound from the ADM relic annihilation constraint. In particular, if a sizeable symmetric component is regenerated before the recombination era, then

---

[1] For contact operators with preferential coupling to specific SM states, such as neutrinos [181], or appropriate flavour dependence, some of the tension with experimental constraints can be alleviated.

the limits on the annihilation cross section from CMB observations [129, 182–184] are around the thermal freeze-out value, for DM masses $\lesssim$ 20 GeV (see Chapter 5). Since the CMB limits are mostly a function of energy injection, rather than the particular annihilation products, and are not subject to uncertainties regarding DM distribution, they leave very little parameter space for early decays, for annihilation cross-sections large enough to meet the ADM relic annihilation requirements.

One way of circumventing these constraints is for the annihilation cross section at late times to be suppressed relative to earlier times, e.g. via velocity-suppression. If the symmetric population is regenerated after freeze-out, but early relative to astrophysical timescales, then the phenomenology of this scenario is much like symmetric DM with a velocity-suppressed cross section, although with the annihilation rate decoupled from the thermal value. An alternative possibility, with distinctive phenomenology, is the case in which the DM remains predominantly asymmetric up to the present time (or at least through the recombination era), with only a small symmetric component regenerated. If the decay timescale is significantly longer than the time at recombination, then CMB constraints are significantly weakened, which can open the possibility of present-day annihilation signals without corresponding CMB signals. As noted at the start of this Chapter, another interesting feature of regenerating the symmetric component through late decays is that its density profile may be modified significantly by the velocity kick from the decay process. Obtaining a sufficiently small velocity kick to keep the regenerated population concentrated in galaxies motivates DM models with a small mass splitting between different components. For these models, the annihilation profile may be different to those arising from conventional models, and could be entirely absent from systems with low escape velocities such as dwarf spheroidal galaxies.

As mentioned, coupling ADM to the SM without violating direct search constraints requires some model-building, and we consider two scenarios in detail. In one case the annihilation portal to the SM is through a pseudoscalar; this alleviates the direct detection constraints, as the DM-proton scattering cross section is significantly suppressed. If the pseudoscalar mass is just above the value needed for an s-channel annihilation resonance, then annihilations during the freeze-out process (when temperatures are high) are enhanced relative to annihilations at later times. This is essentially an example of the velocity dependence discussed above. The second scenario we consider is where annihilation occurs to two on-shell hidden sector vector bosons, which decay relatively slowly to SM states. The small coupling of the vectors to the SM suppresses direct search constraints, and the rate at which we regenerate the symmetric component controls the strength of CMB and late-time annihilation constraints. These models act as a *proof of principle* that annihilation signals can be generated from certain models of ADM, but the constraints that we discuss are more generally relevant to other models of annihilating DM in the low mass region.

4.2.1 Regeneration of symmetric component from models with two dark asymmetric species

To construct a model with late time decays, regenerating a symmetric component of DM, requires some hidden sector structure. By simple analogy to the complexity of the visible sector it is quite conceivable that the hidden sector consists of multiple states and approximately conserved global currents. As a model building example we consider a particular setup, but the constraints and possible signals we find in Section 4.2.2 are more generally applicable.

Let us suppose that two states B', L' in the hidden sector carry (approximately) conserved quantum numbers which we suggestively call dark baryon number B' and dark lepton number L'. In the SM, baryon and lepton number are approximately conserved; EW instantons and sphalerons, and GUT scale physics, do not respect these global symmetries, however these processes still conserve the combination $B - L$. In direct analogy, we propose that both B' and L' are acci-

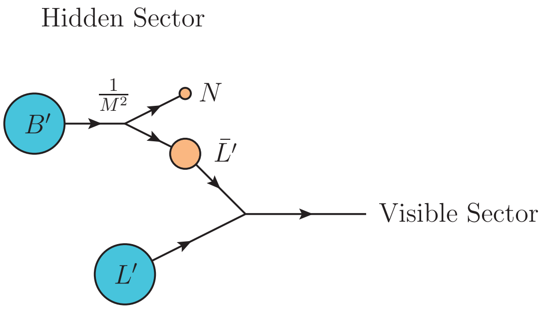

Figure 4.2: Schematic illustration of steps leading to annihilation signal. Initially, B' and L' are the only states in the hidden sector with non-negligible abundances. At some later time, such that it occurs in the current era, B' decays to $\overline{L'}$ along with additional light states labelled N. The $\overline{L'}$ subsequently (on galactic time scales) annihilate with L' to visible sector states leading to potentially observable signals.

dental symmetries of the low energy theory and are violated at some intermediate scale, however the combination $B' - L'$ is conserved by these intermediate scale interactions. We further assume that there are additional effects in the theory that link the asymmetries in the dark and visible sector, so that the true symmetry of the theory is $B - L - (B' - L')$. Since it is expected that all global symmetries are violated by Planck-scale suppressed effects, the combination $B - L - (B' - L')$ may either be gauged in the ultra-violet or violated only by Planck-scale effects that are not important for phenomenology.

Various potential genesis mechanisms have been outlined in the literature, which could be employed to generate the particle asymmetries e.g. [102, 104, 105]. We shall suppose that the asymmetries in B' and L' are of comparable magnitude. For sufficiently high annihilation cross-sections, the B' and L' states remain chemically coupled to the thermal bath long enough for Boltzmann suppression to remove most of their symmetric components. This results in $\overline{B'}$ and $\overline{L'}$ having highly suppressed relic abundances, whilst the yields of B' and L' are set by the particle-antiparticle asymmetries

$$\frac{n_{B'}}{n_\gamma} \simeq \eta_{B'} \ , \qquad \frac{n_{L'}}{n_\gamma} \simeq \eta_{L'} \ . \tag{4.8}$$

We will also assume that $\eta_{B'} \simeq \eta_{L'}$, so that we end up with a relic population of

B' and L' rather than their anti-particles. Asymmetries with different signs and magnitudes are also possible (and may be brought about dynamically, as discussed below), but we will not consider such models in this Chapter.

For such a scenario to lead to annihilation signals we propose that B'-violating operators, suppressed by some intermediate scale, induce the decay of B' to $\overline{L'}$, which subsequently annihilate with the population of L' resulting in observable signals. This scenario is illustrated schematically in Figure 4.2. This is inspired by proton decay due to GUT scale physics [185], inducing a decay $p \to e^+ + \pi^0$ which is B and L violating but $B - L$ conserving. The proton lifetime is thus dependent on the GUT scale, the scale at which B is perturbatively violated,

$$\tau_p \sim \frac{M_{\mathrm{GUT}}^4}{\alpha_{\mathrm{GUT}}^2 m_p^5} \ . \tag{4.9}$$

We expect a similar expression for the lifetime of B' decaying to $\overline{L'}$, dependent on the scale of B' violation (to some appropriate power, set by the dimension of the decay operator).

The case of particular interest is when the decays $B' \to \overline{L'} + \cdots$ (where the ellipsis denotes additional, relatively light, decay products) are slow, so that this process occurs after the dark matter has coalesced into galaxies and clusters. If the decay products acquire too much kinetic energy, they will travel faster than galactic escape velocity. In this case, as discussed later, they are unlikely to annihilate on their way out of the galaxy, resulting in either decay-type profiles or no observable signals. The maximum kinetic energy available is determined by the mass splitting $\Delta m = m_{B'} - m_{L'}$, and a natural way to ensure that the final velocities are low enough, enabling observable annihilation signals, is to have Δm small relative to the DM mass. Such small mass splittings can arise for instance through radiative mass splitting between different DM ‘flavours’. We discuss this constraint more generally in the next section, and outline a model which exhibits small mass splittings in Appendix A.9. Additionally, the small mass splitting will suppress the B' decay rate. For example, if the decay is via a dimension-6 operator induced by B'-violating physics at the scale $M_{\not{B}'}$, the lifetime will be (parametrically)

$$\tau_{B'} \sim \frac{M_{\not{B}'}^4}{\alpha^2(\Delta m)^5} \,, \tag{4.10}$$

where α is the coupling associated to the B'-violating physics.

The fact that the B' decay rate is suppressed (by powers of Δm) relative to symmetry-violating processes at higher energies means that it is necessary to check that the processes in the early universe do not alter the B' and L' asymmetries in undesirable ways. Indeed, as discussed in Appendix A.7, if these interactions are in equilibrium after the asymmetries have been established, they force $\eta_{B'} = -\eta_{L'}$, rather than the same-sign asymmetries required for the models discussed here. Consequently, the asymmetry must be set sufficiently late, such that these symmetry-violating processes are always out-of-equilibrium. Additionally, we assume that these asymmetries are set before freeze-out,[2] leading to an upper limit on Γ (equivalently, a lower limit on Δm). We shall examine these constraints shortly and demonstrate that viable models can be constructed.

4.2.2 General constraints and signals

Having introduced the general structure of the models considered, we now examine the relevant constraints and highlight particular features required for observable annihilation signals to arise in such models. For a given $B' \to \overline{L'} + \cdots$ decay rate Γ, the $\overline{L'}$ population builds up (essentially) linearly over time until a significant fraction of the B' have decayed (unless the annihilation cross section is extremely high, only a small proportion of the $\overline{L'}$ population that is regenerated ever annihilates). This $\overline{L'}$ population translates into an upper bound on the $L'\overline{L'}$ annihilation cross section from astrophysical indirect detection signals (both late-time and recombination-time). A lower bound on the annihilation cross section

---

[2] The alternative case of the asymmetry being set by decays after freeze-out is potentially interesting, however we will not examine such models here.

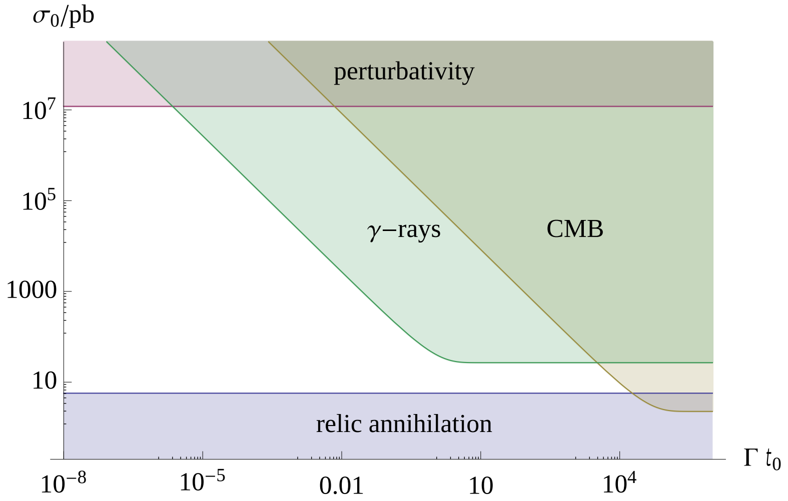

Figure 4.3: Constraints on $B' \to \overline{L'} + \cdots$ decay rate Γ and $L'\overline{L'}$ annihilation cross section σ_0, with $m_{L'} = 10$ GeV, assuming annihilation to muons. The perturbativity bound corresponds to the model of Section 4.2.5, where $L'\overline{L'}$ annihilate into a pair of hidden sector vector particles, which then decay to the SM. Here, t_0 is the current age of the universe. The relic annihilation bound corresponds to the annihilation cross-section needed to annihilate all but 1 percent of the symmetric component, i.e. to obtain $r_\infty \equiv \frac{n_{\overline{B'}}}{n_{B'}} < 0.01$. The CMB bound corresponds to the limit on energy injection from $L'\overline{L'}$ annihilation derived from CMB perturbations [17, 129, 182–184], while the gamma-ray bound is derived from FERMI observations [186] (assuming an NFW profile for the DM halo). We assume that the $\overline{L'}$ injection velocity is small enough that the $\overline{L'}$ distribution is similar to the L' one for the purposes of the gamma-ray constraints; we use the FERMI diffuse observations rather than the galactic centre observations, which would be less robust to profile modifications (see Section 4.2.3).

comes from the requirement that the relic symmetric component is sufficiently depleted due to annihilations in the early universe. Further, demanding perturbative couplings places an additional upper bound on the cross sections.

These constraints fit together as illustrated in Figure 4.3, which shows the allowed regions in terms of the (velocity independent) annihilation cross-section $\langle \sigma v \rangle \equiv \sigma_0$, and the $B' \to \overline{L'} + \cdots$ decay rate Γ. The indirect detection constraints will depend on the DM mass (which sets the number density, and energy injection from annihilation), and on the annihilation channel (here, we show annihilation to muons — alternative channels will generally improve the CMB bounds by a factor of less than 3, and the gamma-ray bounds by less than a factor 10). The perturbativity bound corresponds to a particular choice of model (see Section 4.2.5), while the relic annihilation bound is weakly dependent on the DM mass. We observe that there is a significant amount of parameter space in which viable models can implemented. The potential signal region is the area close to the current gamma-ray limits, which can be probed by current and future experiments. Also, it can be seen that relatively slow decays are required to evade CMB limits. If $\Gamma t_0 \gtrsim \frac{t_0}{t_{\rm CMB}} \sim 4 \times 10^4$ (where t_0 is the current age of the universe, and $t_{\rm CMB}$ is the age at the recombination era), corresponding to the region at the far right of the diagram, then there is typically no allowed parameter space.

A further possible constraint arises from DM self-scattering bounds (see e.g. [187–190]). The relationship between the annihilation cross section and the self-scattering cross-section is model-dependent, so may or may not introduce constraints within the perturbative region. In the model with a light hidden sector mediator considered in Section 4.2.5, the scattering cross section can be sufficiently large to introduce limits. If we drop the assumption of perturbativity, then since the self-scattering cross section will generally be comparable to or larger than the annihilation cross section, we obtain an upper bound on σ_0 of at most around $0.04 \text{ barn} \times \frac{m_{\rm DM}}{10 \text{ GeV}}$. This is low enough that, if the $\overline{L'}$ is ejected from the galaxy, only a small fraction of it will annihilate on the way out — consequently, the spatial distribution of annihilations will be approximately $\propto n_{L'}$, so will resemble a decay profile. Thus, large annihilation cross sections do not remove the need for a small velocity kick if we want to generate an annihilation-type gamma-ray profile.

As we will discuss in Section 4.2.4, some model-building is required to make sure that direct constraints (from collider and direct-detection experiments) do not place strong upper bounds on σ_0. For DM-SM interactions via contact operators, these bounds are generally (for $m_{\rm DM} \lesssim 30$ GeV) below the lower bound from relic annihilation, so would leave no allowed parameter space. Figure 4.3 can be thought of as corresponding to the model of Section 4.2.5, where $L'\overline{L'}$ annihilate to a pair of hidden sector particles, which then decay to the SM. In this case, direct constraints can be largely evaded.

4.2.3 B'-L' mass splitting and $\overline{L'}$ distribution

Unless the velocity of the decay-produced $\overline{L'}$ is low enough, these states will be ejected from the galaxy, and not sufficiently concentrated to give detectable annihilation-type signals. The escape velocity for the Milky Way is $\sim 500\ \mathrm{km\,s^{-1}}$, so the fractional B'-L' mass splitting (assuming two-body decay, with the other product having much smaller mass) should satisfy

$$\frac{\Delta m}{m_{L'}} \lesssim \frac{500\ \mathrm{km\,s^{-1}}}{c} \approx 2 \times 10^{-3}\ . \tag{4.11}$$

For mass splittings much smaller than this, the B'-to-$\overline{L'}$ velocity change will be small compared to the velocity dispersion of the B', so the distribution of the $\overline{L'}$ will be close to that of the B', and annihilation signals will have the standard $\propto n_{B'}^2$ profile. However, for intermediate mass splittings, the extra velocity will be significant, and will result in an altered distribution for the $\overline{L'}$.[3] Qualitatively,

---

[3] As relaxation times for galaxies such as the Milky Way are large enough that stellar encounters are generally unimportant [169], the extra energy will not be removed by gravitational interactions. Also, the bounds on DM self-scattering [187–190] mean that a given particle can interact at most a few times over galactic timescales, so it is only at the upper end of the allowed scattering cross section region that appreciable energy is lost this way. Such large self-scattering cross-sections also have consequences for the dominant component of the DM distribution (push-

the distribution will be ‘puffed out’, with clumpiness being smoothed out and, moreover, systems with low escape velocities (e.g. dwarf galaxies) will not develop a bound population of $\overline{L'}$ states.

Going beyond the two-body decay case, we will obtain a distribution of $\overline{L'}$ velocity kicks, so some fraction of the $\overline{L'}$ will be given higher-than-escape velocities. However, in general it is still the case that, as long as the other final or intermediate states do not have masses close to Δm, very few of the $\overline{L'}$ end up with significantly smaller velocities than $\Delta m/m_{L'}$. For example, if $\Delta m = 0.1 m_{L'}$, then the fraction of the $\overline{L'}$ getting velocity kicks of less than 2×10^{-3} is generally smaller than 5×10^{-6} (see Appendix A.8 for details). So, in the absence of other ‘coincidences’ assuring a small velocity kick, a small mass splitting is needed to obtain significant $\overline{L'}$ bound populations. As discussed in Appendix A.8, instead of tuning the B' and L' masses to be close to each other, we could also tune the masses of the other decay products or intermediate states; however, a small mass splitting is more natural in many model-building contexts.

Quantitatively, Figure 4.1 shows an approximation to the $\overline{L'}$ profiles obtained for different injection velocities, starting from an NFW-type B' profile. As described in Section 4.1, we calculate these by convolving the initial DM phase-space distribution function with a velocity-kick kernel, then reparameterising to find the new steady-state distribution function, and integrating over this to find the new spatial number density. We see, as expected, that the deviation from the distribution of the parent particle is small for injection velocities smaller than the B' velocity dispersion, with the profile being flattened out for larger v_i. For the example in Figure 4.1 the profiles of states produced with $v \lesssim 50$ km s^{-1} remain approximately NFW, and for increasing injection energies the profiles are smooth deformations away from the profile of the parent particle. In Section 4.2.7, we study the effect of this on the observed annihilation profile and the compatibility with tentative signals that may have recently been observed.

---

ing the halo towards isothermality), and we will not consider the details of such models here.

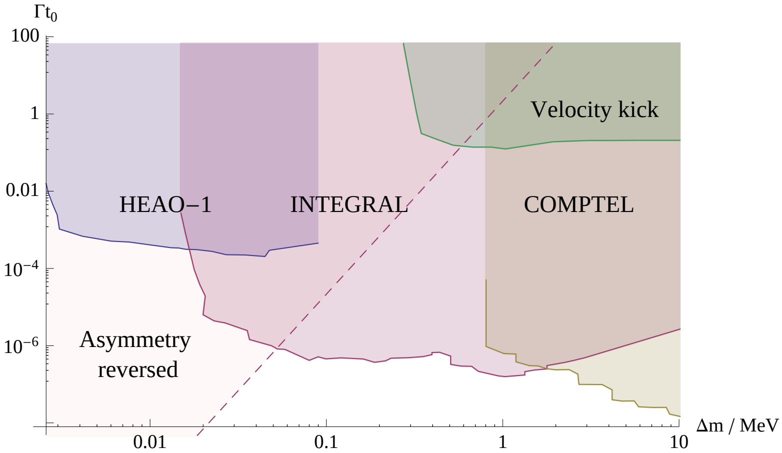

Figure 4.4: Constraints on the $B' \to \overline{L'} + \cdots$ decay rate Γ (compared to the age of the universe t_0) from X-ray observations, for $m_{B'} = 10$ GeV, assuming that all decays are $B' \to \overline{L'} + \gamma\gamma$ and that the DM profile is NFW; constraints from the HEAO-1 (blue), INTEGRAL (red), and COMPTEL (yellow) experiments [127] are shown. The green region corresponds to velocity kicks (assuming $v_i \approx \Delta m / m_{B'}$) ruled out by structure formation constraints [30, 31]. The region above the dotted line is not viable in the model of Appendix A.9, since B' and L' violating interactions stay in equilibrium until $T \lesssim 50\,\text{GeV}$ (see Appendix A.7).

There is also the possibility of indirect signals from the $B' \to \overline{L'} + \cdots$ decays themselves, if the other decay products include SM states [191]. In Figure 4.4 we show conservative ('worst-case') constraints on the decay rate in this scenario; we assume that all decays proceed via $B' \to \overline{L'} + \gamma\gamma$, producing a sharp spectrum of photons and maximising the detectability of the signal. Note that, since the bounds from decays to electrons are at most a factor of around 100 worse than from those to photons [191], then in the absence of a small ($\lesssim$ 0.1 MeV) mass splitting, if annihilation signals are to dominate over decays it is a requirement that most of the energy from decays is dumped into other hidden sector states (or into neutrinos). Otherwise, since only a small proportion of the emitted $\overline{L'}$ have annihilated by the present day, the SM states emitted in every decay will be a stronger signal. This can impose an extra constraint on our model building from the requirement of having additional light stable hidden sector states, and ensuring these have sufficiently small relic abundance. Such light states can arise through small Dirac or Majorana masses, or as pseudo-Goldstone bosons.

If the B' lifetime is not much longer than the age of the universe, then sufficiently large velocity kicks from its decay can affect the structure formation process. The strongest constraints on small velocity kicks ($v_i \lesssim 100\,\mathrm{km\,s^{-1}}$) come from their effect on the population of Milky Way satellite galaxies [30, 31]. Such constraints depend on modelling of the highly non-linear regime of structure formation, but constraints from Lyman-α observations (which probe much earlier times) are almost as limiting [32]. Figure 4.4 shows the galactic bounds in the $(\Delta m, \Gamma)$ plane (assuming $v_k \approx \Delta m / m_{B'}$).

As commented on in the previous section, the requirement that the asymmetries in B' and L' are not disrupted through symmetry-violating processes in the early universe places a lower bound on Δm (equivalently, an upper bound on Γ). In Figure 4.4 we also show the approximate bound from requiring that symmetry-violating interactions decouple sufficiently early, as discussed in Appendix A.7. The mass splittings in Figure 4.4 are related to the velocity kicks, e.g. as studied in Figure 4.1, by equation (4.11). For example, taking $m_{B'} = 10$ GeV, the value used in the figure, $\Delta m \approx 2$ MeV (7.2 MeV) corresponds to a velocity kick in the region of $v = 54$ km s^{-1} (218 km s^{-1}). We can see that there is a significant allowed region for all cosmologically-slow decay rates and mass splittings in the range of interest. However, in combination with the velocity kick bounds described in the previous paragraph, cosmologically early decays are generally excluded, independently from the previously mentioned direct detection bounds.

4.2.4 Direct and indirect detection

In addition to the gamma ray constraints arising from late-time annihilations, there is also the prospect of signals coming from annihilation products in charged cosmic rays (for the low DM mass range we consider, annihilations into neutrinos will generally be beyond the reach of near-term experiments[4]). DM annihilation

---

[4] If the DM is sufficiently strongly self-interacting, and has some scattering cross-section with nuclei, there is the possibility of building up a large population within the Sun, annihilations within which may be detectable by neutrino observatories [165, 192]. Up to some threshold, lower annihilation rates will actually increase this signal (by allowing a larger equilibrium DM population in the Sun), so such signals could arise for decay rates much slower than the age of

into quarks results in cosmic ray antiprotons, the population of which has been measured by the PAMELA experiment (and will also be measured by AMS-02) [193]. Since antiprotons are charged particles, whose trajectories are affected by galactic magnetic fields, their direction of arrival is not simply related to the location of their source, and very little can be inferred about the galactic DM distribution from such measurements. In addition, there is a considerable degree of uncertainty as to exactly how this propagation through the galaxy occurs, and different models result in significantly different derived constraints on DM annihilation rates [194]. Figure 4.5 illustrates how the antiproton limits compare to those from gamma-ray observations, under three different propagation scenarios (MIN/MED/MAX) that are standard in the literature, see e.g. [193]. The limits range from significantly less constraining than those from gamma-rays, to very significantly more so. Consequently, depending on the true propagation, it is possible that annihilation signals may first be observed in either antiprotons or photon signals.

Similar considerations apply to cosmic ray positrons, which are produced by annihilation into leptons (and also by annihilation to electroweak gauge bosons). For annihilation into electrons or muons, the constraints on the DM annihilation cross section from positron observations (for $m_{\mathrm{DM}} \lesssim 100$ GeV) are generally significantly stronger than those from gamma-ray observations (see e.g. Figure 3 of [195]) and CMB perturbations. For annihilation to taus, the constraints are comparable.

In addition to the limits from indirect detection, models of ADM are constrained by direct detection experiments and collider searches for events with missing energy. Specifically, in order for a particle asymmetry to set the relic density, and thus to obtain ADM, the symmetric component must annihilate efficiently (with a cross section larger than that required for symmetric freeze-out) and since these couplings also set the production and scattering cross sections this

---

the universe.

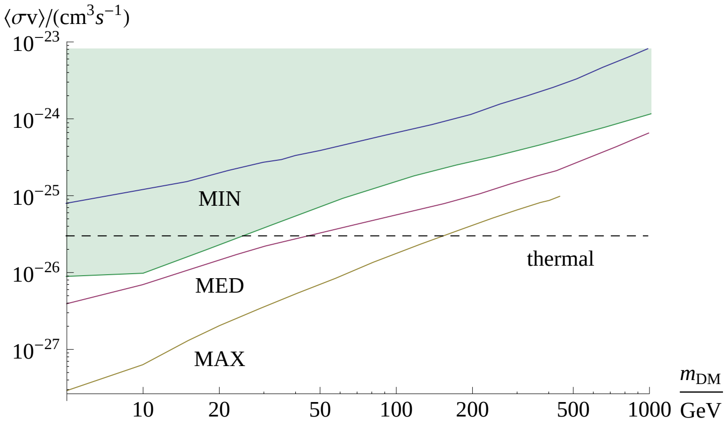

Figure 4.5: Limits on symmetric DM annihilation cross section to $b\bar{b}$ from (blue, red, yellow) PAMELA cosmic ray antiproton measurements [193], under different assumptions with respect to propagation of charged particles through the galaxy. The MIN, MED, MAX scenarios correspond to models giving the minimal, median and maximal DM antiproton flux consistent with cosmic ray observations [196]. FERMI gamma-ray constraints are in green [186]. (Note that the PAMELA bounds correspond to assuming that the DM halo has an Einasto density profile, while the FERMI bounds assume a NFW profile; however, the difference will be minor [194].)

can lead to tension with experimental searches. In particular, if the annihilation of the symmetric component is directly to SM states and can be described via contact operators (i.e. from integrating-out some heavy mediator) then this generally results in fairly strong constraints:

- Annihilation via contact operators involving SM quarks was studied in [114] (see also [111]). It was argued that direct detection experiments and LHC monojet limits typically exclude such models of ADM with minimal flavour structure for $m_{\rm DM} \lesssim 100$ GeV.

- LEP searches for mono-photon events [179] constrain couplings between DM and electrons. For universal couplings of DM to charged leptons they exclude the ADM parameter region for $m_{\rm DM} \lesssim 30$ GeV. Preferential annihilation to μ or τ leptons is not constrained. Direct detection experiments [197] extend this exclusion to multi-TeV masses.

- Ref. [180] considered the limits from collider observations of DM interactions with electroweak gauge bosons, excluding ADM models for $m_{\rm DM} \lesssim 40$ GeV.

These collider limits can be circumvented if the model features a 'light' mediator state [114, 163, 198, 199] (relative to collider energies i.e. $\lesssim$ 100 GeV for LHC searches). In the remainder of Section 4.2.2, we study two illustrative examples in which we can build perturbative models that significantly alleviate these constraints:

- Annihilation of the symmetric component to (on-shell) metastable vector bosons[5] $L'\overline{L'} \to VV$, with V subsequently decaying to SM states (similar to [200]).
- Annihilation via the s-channel process $L'\overline{L'} \to \phi \to$ SM involving a pseudoscalar mediator ϕ, with $m_\phi \approx 2m_{L'}$ such that the cross section is resonantly enhanced, cf. [114].

4.2.5 Annihilation via $L'\overline{L'} \to VV$

Let us consider the case where L' is a fermion and there is a hidden sector vector boson V which acts as a mediator state. For $m_V < m_{L'}$, annihilation to a pair of on-shell vectors is possible, $L'\overline{L'} \to VV$, and if V has a small coupling to the SM, this channel will dominate. As an explicit example of this scenario, we consider the following interaction

$$\mathcal{L} \supset \lambda \left(\overline{L'} \gamma^\mu L' V_\mu + \overline{B'} \gamma^\mu B' V_\mu \right) \ , \tag{4.12}$$

with V subsequently decaying to light SM states. In Figure 4.6 we illustrate how the constraints on λ vary with m_V, for $m_{L'} \simeq 10$ GeV and assuming that V decays dominantly to muon pairs (this assumption is for ease of comparison to experimental constraints). We assume here that the V lifetime is short enough that it does not travel an astronomically significant distance before decaying — if it is

---

[5] The simple alternative with a scalar mediator ϕ (and L' a fermion) is not viable, as in this case the annihilation channel $L'\overline{L'} \to \phi\phi$ is suppressed by v^2. Whilst the symmetric component can be regenerated through early decays without conflict with CMB observables, as the DM velocity in the galaxy is around 10^{-3}, observably high galactic annihilation rates cannot be obtained for perturbative couplings in this model.

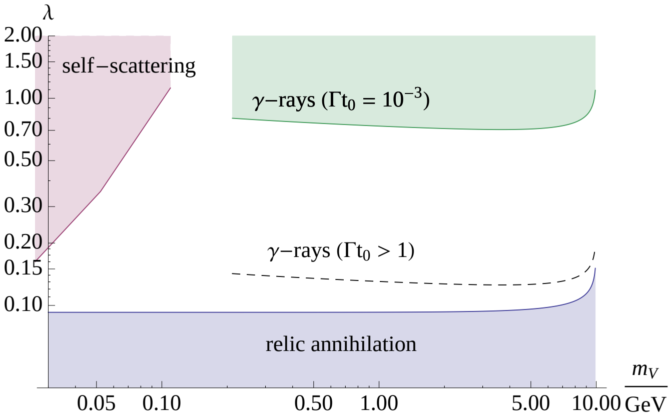

Figure 4.6: Constraints on λ for $m_{L'} = 10$ GeV, with V decaying to $\mu^+\mu^-$. The red curve corresponds to the lower limit on m_V from DM self-scattering [187], the blue curve shows the lower limit on λ required for $r_\infty < 0.01$ (i.e. for efficient annihilation of the ADM symmetric component), the dashed black curve shows the upper bound on λ from FERMI gamma-ray bounds assuming that all of the B' have decayed by the present time ($\Gamma t_0 > 1$), and the green region shows the gamma-ray bounds for the case where only a fraction $\Gamma t_0 = 10^{-3}$ of the B' have decayed. See Figure 4.3 for discussion of the gamma-ray bounds. Decays of V to e^+e^- would result in broadly similar gamma-ray constraints, and would allow m_V down to the self-scattering bound (note that, close to the self-scattering bound, the gamma-ray limits would be altered, since the assumption of a NFW halo is not self-consistent here [187–190]).

longer lived, then the drift of the V from the annihilation point can modify the observed profile, as discussed in [201] (though in that case, we would need to worry about its relic abundance and decays in the early universe). The cascade structure of the annihilation means that the resulting gamma-ray spectrum is softer than that arising from direct annihilations to muons [202] (as taken into account approximately in Figure 4.6), but since the low-energy part of the spectrum is important in setting bounds on the annihilation rate at DM masses this low [186], this does not affect the constraints very significantly. Note that V exchange contributes to DM-DM scattering and, since the self-scattering cross section increases with decreasing m_V, limits on the DM self-interaction [187] (see also [188–190]) give a lower bound on m_V, as indicated in Figure 4.6. Further constraints on this example are encapsulated in Figure 4.3; for the models shown the decays are cosmologically slow in order to evade CMB bounds. Notably, for a wide range of decay rates and mediator masses, models consistent with experimental constraints exist.

If m_V is sufficiently small, then the long-range V exchange between L' and $\overline{L'}$ can give rise to Sommerfeld-type low-velocity enhancement of the annihilation rate. However, the lower limit on m_V from self-scattering implies that this is not significant here. Also, as discussed in Section 4.2.3, DM self-scattering cross sections near to the observational limit (as sometimes invoked to solve problems with small-scale structure formation [203]) have consequences for the shape of the DM halo, though we do not consider the details here.

4.2.6 Annihilation via $L'\overline{L'} \to \phi \to \mathrm{SM}$

We now turn to the second model, in which $L'\overline{L'}$ annihilation proceeds through the s-channel exchange of a mediator ϕ, where m_ϕ is close to resonance. For the case where $m_\phi > m_{L'}$, the $L'\overline{L'}$ annihilations cannot produce on-shell ϕ pairs and rather proceed directly to SM states via a ϕ-mediator. Since we expect L' to be roughly GeV or greater, the DM-proton scattering cross section is well described by an effective operator and if ϕ is a scalar or a vector, coupling to quarks, then large regions of parameter space are excluded by direct detection experiments, see [114].[6] Whilst the effective theory is valid for DM-proton scattering, kinematic effects can be important to the annihilation process and can potentially lead to regions of parameter space which are not excluded by direct searches, as we discuss below.

Given ϕ-DM and ϕ-SM couplings, the $L'\overline{L'} \to \mathrm{SM}$ annihilation cross section is dramatically increased if $m_\phi \approx 2m_{L'}$, such that the s-channel annihilation is close to resonance. This does not make the direct search constraints tighter, so gives us more parameter space for the model. In particular, if m_ϕ is slightly above $2m_{L'}$, then at higher temperatures the thermal averaging samples more of the resonance peak, increasing the annihilation cross section. Effectively an enhancement of $\langle\sigma v\rangle$ at high temperatures occurs, as required for the early-decay case to be viable.

---

[6] More complicated portal interactions can alleviate some direct detection constraints, see e.g. [204–207].

To illustrate the allowed parameter space around the resonance region, we consider an explicit model with a pseudoscalar ϕ coupling to quarks via

$$\mathcal{L} \supset i\lambda\phi\overline{L'}\gamma^5 L' + \sum_q i\lambda' y_q \frac{m_\phi}{m_h}\phi\overline{q}\gamma^5 q\ . \tag{4.13}$$

Figure 4.7 shows the constraints in the (m_ϕ, λ) plane for $\lambda' = 0.14$ (the behaviour is mostly dependent on $\lambda\lambda'$, so we only plot variation with λ). As discussed above, there is a strong distinction between m_ϕ just above vs below $2m_{L'}$. Above, the enhancement of the annihilation cross section with temperature means that there is a large allowed region between the couplings necessary for relic annihilation and those ruled out by astrophysical constraints. For $m_\phi < 2m_{L'}$, on the other hand, higher collision energies result in ϕ being more off-shell. Consequently, in this region, the relic annihilation constraint rules out everything until λ is very large.

The figure shows the strongest bounds, when the decays are early enough to maximise the limits from both CMB and galactic timescales. Since this still leads to viable parameter space, early decays are permitted (unlike the previous models, which as seen in Figure 4.3 are very constrained if there are early decays). Note that, as we increase the decay time past recombination time, the CMB limits become less constraining relative to the gamma-ray bounds (cf. Figure 4.3), so (depending on assumptions about antiproton propagation, cf. Fig 4.5) there is a large parameter space in which gamma-ray signals may realistically be seen before other signals.

4.2.7 Tentative signals and morphology

Recently, there have been suggestions [209] (see also [210–214]) of a gamma-ray excess from the galactic centre and its vicinity, compatible with DM of mass $\sim$ 10 GeV DM (approximately NFW-profile) annihilating to leptons (with $\langle\sigma v\rangle \simeq 2\times 10^{-27}\text{cm}^3\text{s}^{-1}$) or with $\sim$ 50 GeV DM annihilating to quarks (with $\langle\sigma v\rangle \simeq 8\times 10^{-27}\text{cm}^3\text{s}^{-1}$). Both models discussed above can reproduce a signal of this

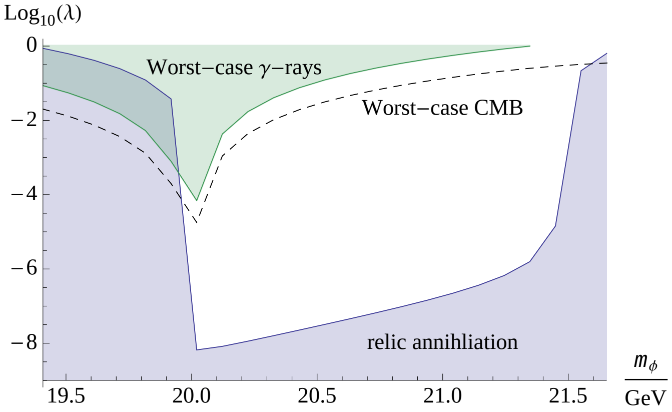

Figure 4.7: Constraints on λ for $m_{L'} = 10$ GeV, for coupling to quarks as described in section 4.2.6. The blue curve shows the lower limit on λ required for $r_\infty < 0.05$ (i.e. for efficient annihilation of the ADM symmetric component), and the green region is excluded by gamma-ray bounds (see Figure 4.3 for details), assuming that all of the B' have decayed by the present time. The black dotted curve shows the exclusion bound from CMB perturbations, assuming that all of the B' have decayed by recombination time. The relic abundance and annihilation cross-section calculations were carried out using the `micrOMEGAs` package [208].

kind, but only with a sufficiently small B'-L' mass splitting such that the $\overline{L'}$ profile remains sharply peaked towards the galactic centre. It was claimed in [209] that, for symmetric annihilating DM, the signal is fit well by a generalised NFW type profile with shape parameter $\gamma \simeq 1.2$, and with some systematic uncertainty possibly allowing γ to vary around this value to a maximum of ~ 2 (see also [215]).

Figure 4.8 shows the profile shapes resulting from different $B' \to \overline{L'} + \cdots$ injection velocities, starting from a NFW-type ($\gamma = 1.2$) B' profile. These are calculated as described in Section 4.1, utilising the properties of the steady-state DM phase space distribution function. As it illustrates, we need $v_i \lesssim 120$ kms^{-1} to match a symmetric annihilation signal with $1.1 < \gamma < 1.3$, corresponding to a fractional B'-L' mass splitting of $\lesssim 4 \times 10^{-4}$ (subject to the caveats mentioned in Section 4.2.3 and Appendix A.8). If the mass splitting is not much smaller than this limit, then the DM gamma-ray signals from structures with lower velocity dispersions than the galaxy will be modified compared to what we expect from standard annihilating symmetric DM. At present, the nature of these structures (e.g. DM clumps in the galactic halo) is poorly constrained, so it is hard to

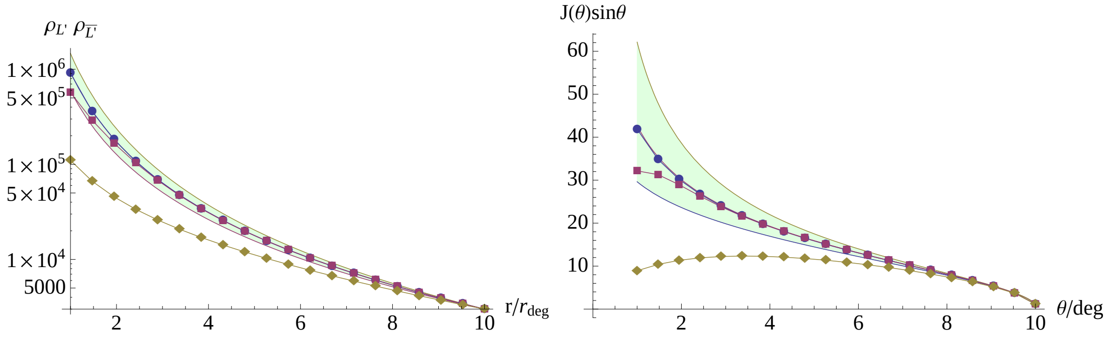

Figure 4.8: ***Left:*** The $\rho_{L'}\rho_{\overline{L'}}$ profile for different L' and $\overline{L'}$ profiles (in arbitrary units, normalised to a common value at $r = 10r_{\text{deg}}$, where a distance of r_{deg} above the galactic centre corresponds to $b = 1°$). The blue dots indicate the $\gamma = 1.2$ L' profile, and a $\overline{L'}$ profile obtained by starting with a NFW $\gamma = 1.2$ profile and applying a velocity kick of 1 kms^{-1}. The red and yellow dots correspond to the same situation, but with velocity kicks of 76 kms^{-1} and 163 kms^{-1} respectively. The shaded region corresponds to generalised NFW profiles (for L' and $\overline{L'}$) with $1.1 < \gamma < 1.3$ required to best match the apparent gamma-ray excesses near the galactic centre [209]. ***Right:*** For a given model the signal size is determined by the integral $J(\theta) = \int dl \rho_L \rho_{\overline{L}}$ along the line-of-sight as a function of angle from galactic centre. Colours and shading as in left panel.

pick out any definite differences, but since the escape velocity for most dwarf galaxies is below $\sim 50\ \text{kms}^{-1}$ [216], and the velocity dispersion is $\sim 10\ \text{kms}^{-1}$ [217], if v_i is high enough then we will almost completely suppress the annihilation signal from dwarf galaxies due to most of the $\overline{L'}$ population escaping. It is not obvious whether, once astrophysical uncertainties are taken into account, near-term gamma-ray observations of dwarf galaxies will be able to place constraints on such low DM annihilation cross section [218–220].[7]

In addition to the modified $\overline{L'}$ distribution in space, the main possibly-observable difference from a standard annihilating symmetric DM scenario is the change in $\overline{L'}$ population over time. However, due to the small (symmetric) annihilation cross section required to match the signal, the effect on the CMB from symmetric annihilations would be below cosmic variance [129, 182–184], so it would not be possible to detect the difference between this and a smaller effect in the $\overline{L'}$ case. This is not a completely general statement — there do exist viable symmetric

---

[7] However, there are current suggestions that a small gamma-ray excess seen from the Reticulum II dwarf galaxy could, assuming suitable DM properties for that galaxy, correspond to the galactic centre excess [221] — futher FERMI observations should clarify this.

DM models which have observable annihilation effects on the CMB, and in these cases the late-decay ADM model would make different predictions. Also note that possible collider signals of an ADM model may differ from those of a symmetric DM model (though in neither case are we guaranteed to have such signals, e.g. the models of Section 4.2.5 in our case, and the symmetric model of [222]).

4.3 Summary

This Chapter has presented an approximate method of computing the modifications to DM halo distributions arising from non-relativistic velocity kicks (in a static gravitational potential), and as an example application of this, has outlined a new class of ADM models in which annihilation signals are generated. In particular, we discussed a scenario involving two states B', L' with comparable relic densities, stabilised by two different approximately conserved quantum numbers. Subsequently, processes which violate these approximate symmetries lead to decays of the heavier state B', regenerating the symmetric component of the lighter species L'. This allows for the prospect of observable indirect detection signals with annihilation-like profiles via $L'\overline{L'}$ annihilations.

One of the principal model-building challenges for producing observable signals in this manner is that, unless the mass splitting between B' and L' is small, most of the $\overline{L'}$ generated via B' decays are immediately ejected from the galaxy and do not give rise to annihilation-type signals. The desire for observable annihilation signals constrains the parameter space of the model, as discussed in Section 4.2.3 and illustrated in Figure 4.3. Moreover, if the mass splitting is moderate then the symmetric component of L' may escape galactic structures with low escape velocities. Thus a distinctive signature of this class of models is that annihilation signals could be observed in our galaxy and conspicuous by their absence in dwarf galaxies.

There is a range of further experimental constraints on these models both from direct and indirect probes, as encapsulated in Figs. 4.3, 4.4, and 4.6. In order to evade the strong direct detection bounds we studied two particular scenarios: in the first case annihilations occur on resonance, and in the second the DM annihilates to pairs of meta-stable hidden sector states. We highlighted the prospect for indirect detection signals in the near future — see for instance Figs. 4.3 and 4.5 — and commented on tentative signals of DM annihilations near the galactic centre [209–214] in Section 4.2.7.

To conclude, we find that whilst models of low-mass ADM with a symmetric component regenerated by decays can produce observable annihilation signals, and satisfy the various experimental bounds, these models are typically required to possess some specific properties and thus exhibit some predictive features. Several experiments have hinted at the possibility of DM in the 1 GeV to 50 GeV range, both direct detection [223, 224] and indirect signals of DM annihilation [209–214]. If experimental evidence were to point towards annihilation-type signals consistent with light DM, annihilation cross sections differing from the thermal freeze-out value, and a lack of signals from low-escape-velocity structures, these would be suggestive of the kind of models we have discussed.

CHAPTER 5

Conclusions

As discussed in Chapter 1, there are many strands of astrophysical and cosmological evidence that, taken together, cannot be explained by the Standard Model alone, but fall neatly in place on the assumption that there exists some new form of matter, which interacts only weakly with the SM, but accounts for 5 times the mass. The nature and origin of this 'dark matter' is one of the central mysteries of fundamental physics — as emphasised in Chapter 1, there are many possible models for its microphysics and history, and distinguishing between these will require further experimental evidence. However, recent and near-future experiments have the ability to probe some of the predictions of theoretically well-motivated dark matter candidates. In this Chapter, we will review the status and prospects of some of the experimental areas that constrain DM candidates, primarly focussing on how they relate to the simplest thermal dark matter scenarios, and on how the kinds of models we have considered in previous chapters can affect such observations and the relationships between them.

Couplings between dark matter and the SM often imply signals in more than one type of experiment — as per the standard 'complementarity' diagram, Figure 5.1, a given DM-SM coupling has consequences for DM-SM scattering (direct detection experiments, astrophysical capture, etc.), for DM annihilation (in the early universe, or at later times), and for DM production in initially-SM-only pro-

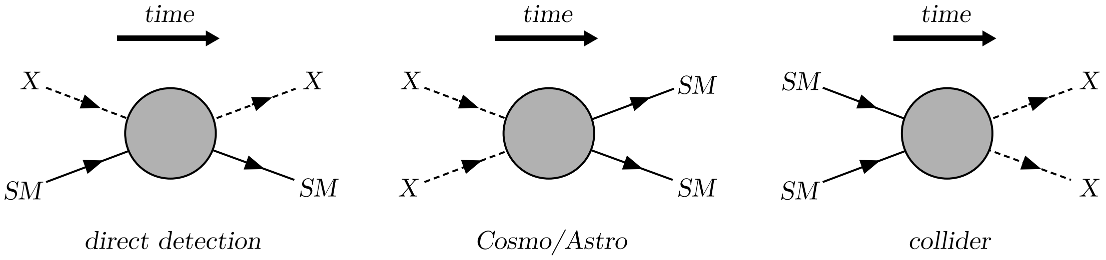

Figure 5.1: Schematic representation of how interactions between DM states X and SM states can lead to signals in different types of experiments.

cesses (such as at colliders, or astrophysically). If we try to assume the 'simplest' scenario, in which the coupling is contact-like at all scales involved, without non-minimal flavour structure, and the cosmological abundance is set by freeze-out from the SM thermal bath, then these three types of constraints are all at the stage of ruling out DM masses below a few tens of GeV. The next obvious step is to consider coupling via SM mediators — the Weakly Interacting Massive Particle scenario — for which there is more parameter space available, but much of which should be within the reach of medium-term experiments.[1] Beyond that, one can introduce extra light states into the theory, which affect the momentum depedence of cross sections, and open up additional channels in annihilations.

The DM models that we considered in Chapters 2, 3 and 4 highlight further possible modifications. The coherent enhancement of DM-SM scattering rates arising from the large composite states of Chapters 2 and 3 can suppress collider signals relative to direct detection rates, as well as introducing characteristic modifications to direct detection signals. In the model of Chapter 4, the regeneration of a small symmetric component from initially asymmetric DM allows astrophysical annihilation signals which are decoupled from the standard symmetric thermal freeze-out cross section, and can also change the relationship between astrophysical signals from different eras and targets.

---

[1] Couplings to only the Z boson imply a direct link between freeze-out annihilations and direct detection scatterings, with the latter required to be much more frequent than observed. However, couplings to the Higgs, which has small interactions with the u and d quarks, or to $W^{\pm}$, where scattering is loop-suppressed, can decrease the direct detection rate for a given annihilation cross section, rendering such scenarios currently safe, but potentially within the reach of medium-term experiments [225, 226].

Experimentally, each of the three areas will see significant improvements in the coming years. Direct detection experiments have perhaps the most impressive roadmap, summarised in Figure 5.2, which shows how experiments planned for within the next 5 years should improve today's upper bounds on DM-SM cross sections by over 100 times over a large mass range, covering large portions of the WIMP parameter space. The figure also illustrates how, beyond that generation of experiments, the flux of neutrinos from the atmosphere, from supernovae, and from the Sun will start to impose a background floor on the event rate. Directional detection methods could potentially resolve this degeneracy [227], but involve ambitious, as-yet-untested technologies.

Turning to astrophysical observations, for both annihilating DM (with standard velocity dependence) and decaying DM, the strongest constraints come from the recombination era, as measured via the CMB, and from present-day cosmic ray observations. The Planck satellite recently improved the constraints on ionising energy injection at the recombination era, as shown in Figure 5.3. For simple symmetric DM scenarios, these rule out thermal DM below masses of $\sim 10\,\mathrm{GeV}$. Future satellite proposals (e.g. CMBPol [230]) would essentially be able to reach the cosmic variance limit, raising this limit to $\sim 50\,\mathrm{GeV}$.

While effects on the CMB basically just depend on the total energy injection, and its average ionising efficiency, cosmic ray constraints depend significantly on the specifics of the injection. Taking the example of gamma rays, the most sensitive constraints at energies below $\sim$ TeV come from the FERMI satellite. Figure 5.4 shows recent limits, from 6 years of FERMI data, on the gamma-ray emission from Milky Way dwarf galaxies, interpreted as a constraint on the annihilation of DM to $b\bar{b}$ quarks. These limits rely on assumptions about the DM profile shape in such systems — the figure assumes NFW profiles, which as discussed in Section 1.1.5 are possibly too centrally concentrated, so the constraints should be viewed as optimistic. However, even the constraints from the Milky Way halo, for which the distribution is less uncertain, rule out symmetric thermal DM of this kind below

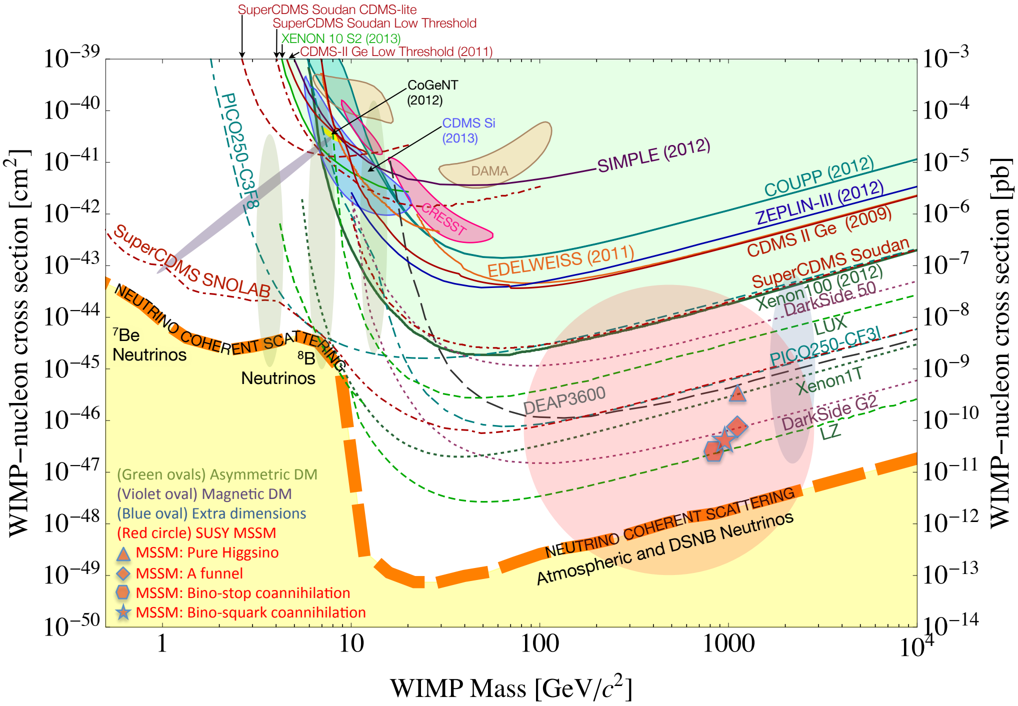

Figure 5.2: Limits on WIMP-nucleon spin-independent cross sections from current and near-future direct detection experiments — figure reproduced from [228]. The green area is ruled out by experiments up to 2013 — since then, LUX has reported results consistent with no DM signal, expanding the excluded region [229]. Coloured regions within this area are reported signals which conflict with other reported exclusions. The yellow band indicates the approximate level at which the background from solar, atmospheric, and supernovae neutrinos will start to degrade direct detection sensitivity. The light shaded ovals show approximate expected signal regions in various theoretical models, as indicated at the bottom left.

$\sim 20\,\mathrm{GeV}$. Future observations will, especially in low-background systems such as dwarf galaxies, be able to probe to even lower cross sections.

Cosmic ray signals from charged particles have their directional information affected by galactic magnetic fields, so do not allow specific targets to be picked out, and generally suffer from more uncertain astrophysical backgrounds than in gamma rays. However, there is still the prospect that interesting spectral features may be observed in experiments such as AMS-02 and follow-ons (see e.g. [231]).

With the recent observation of extra-solar neutrinos by the IceCube experiment [232, 233], an additional window into the high-energy universe has been opened up. While events rates are at present low, future upgrades should improve this [234], and in many models, neutrinos provide a very useful probe of DM annihilations or decays, especially for larger DM masses [235].

Generally, astrophysical energy injection constraints are relevant to standard asymmetric DM scenarios only through bounding the DM decay rate. However, the previous Chapters have illustrated how, in dark sectors with extra structure, annihilation-type signals could arise in ADM models, either through the regeneration of a symmetric component (Chapter 4), or through inelastic DM-DM collisions (Chapter 2). This would change the link between the freeze-out annihilation cross section and late-time event rates, as well as potentially altering the temporal, spatial and spectral properties of such signals.

The constraints from collider experiments are more model-dependent than those obtained from direct detection experiments or astrophysical observations. At the high energy frontier, the LHC second run will soon begin, and should extend the constraints on many electroweak scale DM candidates significantly (see e.g. [236]). In addition to these constraints on more massive particles, there is also the prospect of high-luminosity, lower-energy experiments giving better constraints on lighter, weakly coupled particles, as reviewed in [237]. Such states act as DM-SM mediators in many models of lighter DM (relevant to the models of Chapter 4), and may also be expected in dark sector models featuring self-interactions,

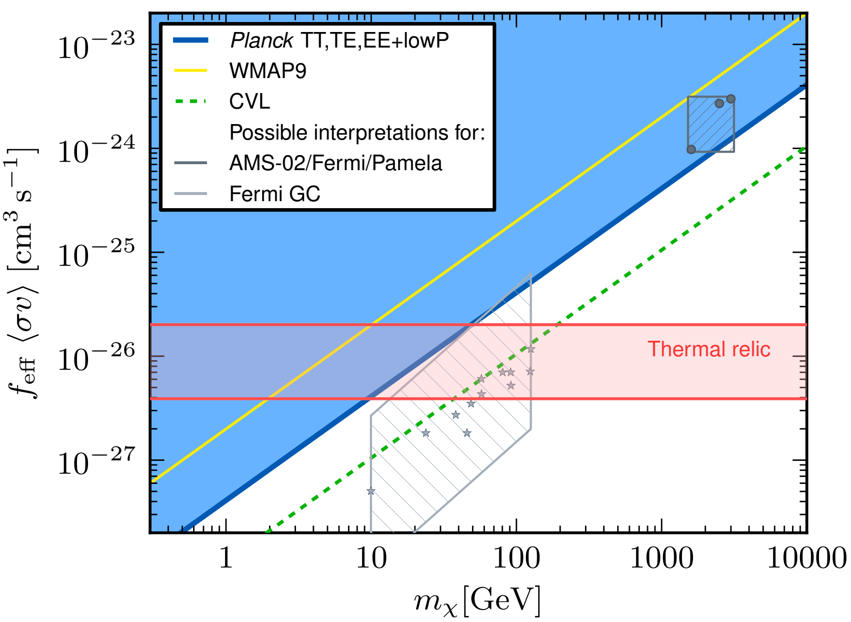

Figure 5.3: Constraints on dark matter annihilation, from energy injection during the recombination era as measured by the Planck satellite via the CMB — figure produced from [17]. The quantity constrained is $f_{\mathrm{eff}}\langle\sigma v\rangle$, where f_{eff} is the ionising efficiency of energy injection from annihilations. The blue area is excluded (at 95% CL) by Planck measurements. The green dotted curve is the best possible bound that could be obtained from CMB measurements (the 'cosmic variance' limit). The red band shows the range of $f_{\mathrm{eff}}\langle\sigma v\rangle$ corresponding to different annihilation channels, for cross sections giving the correct relic abundance from symmetric freeze-out (Section 1.2.3). For further details, see [17].

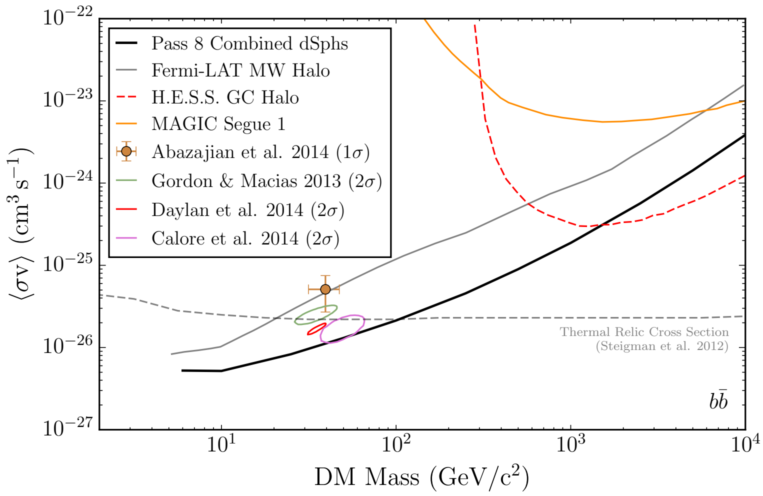

Figure 5.4: Constraints on gamma ray emissions from dark matter annihilation to $b\bar{b}$ quarks from the FERMI satellite — figure reproduced from [220]. The solid black curve is the limit from observations of dwarf spheroidal galaxies, assuming that these have NFW dark matter profiles. The solid grey curve is the limit from diffuse Milky Way halo emissions [186], while the dashed grey curve is the annihilation cross section corresponding to symmetric freeze-out with the correct relic abundance (Section 1.2.3). Curves at upper right are constraints from ground-based atmospheric Cherenkov detectors, and horizontal dotted line is annihilation cross section giving correct relic density from symmetric freeze-out. For more details, see [220].

as discussed in Chapter 2. In particular, as emphasised above and in Section 4.2.4, asymmetric DM models either need to annihilate away their symmetric abundance to the SM, which for light ($\lesssim 100\,\mathrm{GeV}$) DM cannot occur through contact interactions without non-minimal flavour structure, or annihilate into/via lighter hidden sector states. These must either decay or annihilate into the SM, or imply the existence of extra light dark species through to the present day (cf. Section 2.3.2). Thus, constraints on light, weakly coupled states are very useful for constraining DM models.

Light mediators are one way of modifying the relationship between low-momentum-transfer processes, such as direct detection scatterings, on the one hand, and processes such as particle annihilation or creation, on the other. Chapters 2 and 3 present another, in the form of coherent enhancement of scattering from large composite DM states, with its accompanying momentum-dependent form factors. As outlined, this can enhance direct detection event rates relative to collider rates by a factor of up to A, the compositeness number of the DM state, while the extended dark sector required to bind together the composite states can provide natural candidates for the lighter states required to annihilate away the early-universe symmetric abundance.

There are, of course, many other ways in which dark matter could depart from simple thermal models. In particular, its cosmological history and experimental signatures could be drastically different, as for e.g. axion-like particles. With many reasonably well-motivated DM candidates, it is clearly important to look for dark matter in as many ways as possible. However, with multiple lines of experimental evidence converging to narrow down the parameter space for simple models of thermal DM, understanding how extra structure in the dark sector — motivated from a number of theoretical directions – could change observable phenomenology in generic ways, may help in understanding the implications of both null results and any future detections.

It is an exciting time in the experimental hunt for dark matter. While there are no guarantees of positive results, new areas of model space are being probed at a rapid pace. Whatever the results, we will learn more about what makes up our universe, hopefully taking us further down the path towards understanding physics beyond the Standard Model.

APPENDICES

A.1 Transition from equilibrium to aggregation

In chemical equilibrium, detailed balance for the $k + (A - k) \leftrightarrow A$ process implies that

$$\Gamma_{A \to (k, A-k)} \tilde{n}_A = \langle \sigma v \rangle_{(k, A-k) \to A} \tilde{n}_k \tilde{n}_{A-k} \, , \tag{A.1}$$

where the $\tilde{n}_k$ are the equilibrium number densities, $\Gamma_{A \to (k, A-k)}$ is the rate of $A \to (k, A-k)$ dissociations for a single A-DN (in general, this depends on the abundances and velocities of other species), and $\langle \sigma v \rangle_{(k, A-k) \to A}$ is the thermally averaged fusion cross section (we assume, as is almost always the case, that mean free paths are long enough so that velocity rather than diffusivity is important). If we assume that the fission rate is purely determined by the temperature, then when we are in kinetic equilibrium at (non-equilibrium) number densities n_k etc.,

$$\Gamma = \langle \sigma v \rangle \frac{\tilde{n}_k \tilde{n}_{A-k}}{\tilde{n}_A} \, . \tag{A.2}$$

This assumption about the fission rate will be violated if DN-DN collisions often lead to 'prompt' fragmentations, rather than either elastic scatterings, or inelastic collisions that result in a thermally-equilibrated excited state (c.f. the 'compound nucleus' model for SM nuclear collisions [119]). The same is true for DN collisions with other baths that do not have their chemical equilibrium abundance.

Assuming ideal gas behaviour, the equilibrium number densities are related by

$$\frac{\tilde{n}_A}{\tilde{n}_{A-k}\tilde{n}_k} = \frac{g_A}{g_k g_{A-k}} \left(\frac{2\pi}{m_A T}\frac{m_A^2}{m_k m_{A-k}}\right)^{3/2} e^{(m_k+m_{A-k}-m_A)/T} \,, \tag{A.3}$$

where g_k is the number of effective degrees of freedom of k-DN. Writing $m_k = km_1 - B_k$, and assuming that binding energies are a small fraction of the mass, this is

$$\frac{\tilde{n}_A}{\tilde{n}_{A-k}\tilde{n}_k} \sim \frac{g_A}{g_k g_{A-k}} \left(\frac{A}{k(A-k)}\right)^{3/2} \Lambda^3 e^{(B_A-B_k-B_{A-k})/T} \,, \tag{A.4}$$

where $\Lambda = \sqrt{2\pi/(m_1 T)}$.

The overall forward rate for the $k + (A-k) \leftrightarrow A$ process is

$$\langle\sigma v\rangle n_k n_{A-k} - \Gamma n_A = \langle\sigma v\rangle n_k n_{A-k} \left(1 - \frac{\tilde{n}_k \tilde{n}_{A-k}}{\tilde{n}_A}\frac{n_A}{n_k n_{A-k}}\right) . \tag{A.5}$$

Thus, as long as

$$\frac{n_k n_{A-k}}{n_A} \gg \frac{\tilde{n}_k\tilde{n}_{A-k}}{\tilde{n}_A} \quad \Leftrightarrow \quad n_k \Lambda^3 e^{\Delta B/T} \gg \frac{n_A}{n_{A-k}}\frac{g_k g_{A-k}}{g_A}\left(\frac{k(A-k)}{A}\right)^{3/2} \,, \tag{A.6}$$

dissociations will give only a small correction to the fusion rate. For the $1+1 \leftrightarrow 2$ process, we start building up when $n_1\Lambda^3 e^{B_2/T} > 1$. More generally, if we assume that typical binding energy differences rise fast enough with size difference (for example, in a liquid-drop type model $B_k = \alpha k - \beta k^{2/3}$, the surface tension term β gives $B_A - B_{A-k} - B_k \sim \beta k^{2/3}$ for $A > k$), then if $n_0\Lambda^3 e^{\alpha/T} \gg 1$ (where n_0 is the number density of nucleons), the inequality should hold for all of our fusion processes between $k, A-k$ states with reasonable density, with the possible exception of anomalously low (or wrong-sign) binding energy differences for small-number states.

Since $n_0\Lambda^3 \ll 1$ (the DM is a dilute gas), $n_0\Lambda^3 e^{\alpha/T}$ becomes $= 1$ at $T \ll \alpha$. After that, and assuming that $\frac{-d\log T}{d\log a} = \mathcal{O}(1)$, we have $\frac{d\log LHS}{d\log a} \sim \frac{\alpha}{T} \gg 1$. So, with the possible exception of small-k B_k values being much smaller than expected, we go from being near-equilibrium, to dissociations being very suppressed, in a time that is parametrically $H^{-1}\frac{T}{\alpha}$.

Furthermore, during this time the build-up of DN proceeds at most as quickly as a fusions-only aggregation process, like that considered in Section 2.2. As explained there, in many regimes this progresses fairly uniformly over the first Hubble time, so a modification to the fusion rates during a small initial fraction of this time will have a small overall effect on the result.

A.2 Matrix elements for inelastic scattering

Suppose that we have a scattering process in which a state i, with initial momentum $\mathbf{k}$, scatters off a state I with initial momentum $\mathbf{p}$ (all non-relativistic), resulting in final states f and F with momenta $\mathbf{k}'$ and $\mathbf{p}'$ respectively. The matrix element for this, in the Born approximation, is

$$\mathcal{A} = \langle f, \mathbf{k}'; F, \mathbf{p}' | H_{\text{int}} | i, \mathbf{k}; I, \mathbf{p} \rangle \tag{A.7}$$

$$= \langle f, \mathbf{k}; F, \mathbf{p} | e^{i\mathbf{q}\cdot(\hat{\mathbf{x}}_F - \hat{\mathbf{x}}_r)} H_{\text{int}} | i, \mathbf{k}; I, \mathbf{p} \rangle \tag{A.8}$$

$$\equiv \int d\mathbf{r}\, e^{i\mathbf{q}\cdot\mathbf{r}} V_{\text{eff}}(\mathbf{r}, \mathbf{v}) \ , \tag{A.9}$$

where $\mathbf{k}' - \mathbf{k} = \mathbf{p} - \mathbf{p}' \equiv \mathbf{q}$ is the momentum transfer, $\mathbf{v}$ is the relative velocity of i and I, and $\langle \mathbf{x}_f; \mathbf{x}_F | H_{\text{int}} | \mathbf{k}; \mathbf{p} \rangle \equiv (2\pi)^{-3} V_{\text{eff}}(\mathbf{x}_f - \mathbf{x}_F, \mathbf{v}) e^{i\mathbf{k}\cdot\mathbf{x}_f} e^{i\mathbf{p}\cdot\mathbf{x}_F}$. That is, the matrix element is given, as a function of the momentum transfer $\mathbf{q}$, by the Fourier transform of a (possibly velocity-dependent) effective potential V_{eff}, whose form will depend on the interaction Hamiltonian. If the initial or final states have directional properties (polarisations), V_{eff} may also depend on those.

As discussed in Section 3.2.1, the surface modes of an incompressible liquid drop can be obtained by quantising the classical surface oscillations, in which the surface is displaced as in equation 3.14. Classically, for a scalar interaction between a plane-wave scatterer and the nuclear matter, the Fourier transform of the interaction potential is given by

$$F(\alpha_{lm}) = \int_{r<R'(\theta,\phi)} d^3\mathbf{r}\, e^{i\mathbf{q}\cdot\mathbf{r}} V_0 \tag{A.10}$$

$$= V_0 \int d\Omega \int_0^{R'(\theta,\phi)} r^2 dr \sum_{l'} (2l'+1) i^{l'} j_{l'}(qr) P_{l'}(\cos\theta) \ , \tag{A.11}$$

where we have taken $\mathbf{q}$ to be in the $\mathbf{z}$ direction. Recalling the definition of $R'(\theta, \phi)$ in equation 3.14, this integral is clearly zero for $m \neq 0$. Expanding to first order in a given α_{l0}, and eliding V_0,

$$F(\alpha_{l0}) = F(0) + \sqrt{4\pi} \int d\Omega\, \alpha_{l0} R^3\, Y_{l0}(\theta) \sum_{l'} (2l'+1)^{1/2} i^{l'} j_{l'}(qR) Y_{l'0}(\theta) \tag{A.12}$$

$$= F(0) + \alpha_{l0} \frac{3A}{\sqrt{4\pi}} (2l+1)^{1/2} i^l j_l(qR) \ . \tag{A.13}$$

Treating each mode as a harmonic oscillator, we have $\hat{\alpha}_{l0} = \epsilon_l(\hat{a}_l + \hat{a}_l^\dagger)$, where ϵ_l is the dimensionless amplitude from equation 3.17, and $\hat{a}_l^\dagger$ is the creation operator for the $l, 0$ mode. So the matrix element between the ground state and the first excited state is, to first order in ϵ_l, given by

$$\langle 1_l | F(\hat{\alpha}) | 0 \rangle = \frac{3A}{\sqrt{4\pi}} (2l+1)^{1/2} i^l \epsilon_l j_l(qR) \ . \tag{A.14}$$

Higher phonon number states are associated with further factors of ϵ_l (for the appropriate l numbers), and more factors of qR in front of the spherical Bessel function. For the expansion to make sense, we must have that $j_l(qr)$ varies slowly over the interval $R(1 \pm \epsilon)$, so we need $qR \lesssim \pi/\epsilon_l$. Beyond this approximation,

$$\langle 1_l | F(\hat{\alpha}) | 0 \rangle = \int d\alpha\, \psi_1^*(\alpha) \psi_0(\alpha) F(\alpha) \ , \tag{A.15}$$

where the ψ_n are the oscillator wavefunctions (for a harmonic oscillator, Hermite polynomials multiplied by an exponential), and $F(\alpha)$ is from equation A.11 (note that the oscillator properties derived in Section 3.2.1 are also to first order in

ϵ_l). In particular, comparing equation A.14 to the elastic scattering form factor $3Aj_1(qR)/(qR)$ from equation 3.2, both scale as $A\epsilon_l^2$ at $qR \sim 1/\epsilon_l$, but the correct form of the inelastic form factor from equation A.15 drops off faster than the elastic form factor beyond this, since the wavefunction for the surface displacement integrates over multiple, cancelling, Bessel-function periods.

A.3 High-momentum scattering from large composite states

In this Appendix, we consider the scattering behaviour of large composite states when the momentum p of the incoming scatterer is such that $pR \gg 1$, where R is the radius of the composite state.

A.3.1 Coherent scattering

Taking the composite state to be much heavier and much larger than the scattering state, we can approximate the scattering as being against an infinite uniform medium (assuming that p is small enough that it does not resolve structure on the scale of individual constituents). Since the collective modes are linearly dispersing, $\omega = c_c k$, then by the usual pseudo-momentum and energy conservation considerations, scatterers can only excite these if their velocity relative to the medium is greater than c_c (as per superfluids). Putting in some illustrative numbers, the speed of CNO nuclei inside the Sun is $v \simeq 3 \times 10^{-4} c$, while the speed of sound for compressional modes of SM-like nuclear matter is around $0.1c$.

For a composite state of finite radius, this corresponds to the fact that the modes of small enough energy to be excited have $k \ll q$, so the wavefunction overlap in the form factor is very small (the q wave oscillates much faster than the k wave, giving a large cancellation). With collective surface modes, as explained in Appendix A.2, for $\epsilon_l qR \gg 1$ there is again a large cancellation.

The above comments assume that the composite state is in its ground state.

If there is some non-zero occupation number for high-wavenumber modes, then down-scatterings of these are energetically permitted, and will not suffer from the cancellation suppression described. We do not consider the case of scattering against excited states here, assuming that the de-excitation times are much shorter than the times between composite-SM collisions (for this to be the case, de-excitation will generally have to be to hidden sector states).

The elastic scattering form factor should fall off at least as fast as $(qR)^{-2}$. For thermalisation-type processes, we are most interested in the rate at which SM scatters exchange energy-momentum with the composite state, which for dominantly soft scattering will be set parametrically by the momentum transfer cross section $\sigma_{\rm tr} = \int (1-\cos\theta)\frac{d\sigma}{d\Omega} d\Omega$. Writing $\frac{d\sigma}{d\Omega} = \frac{\sigma_0}{4\pi} f(qR)/(qR)^4$, and using $q^2 = 2\mu^2 v^2 (1-\cos\theta)$ in the CoM frame,

$$\sigma_{\rm tr} = \frac{1}{2}\sigma_0 \int d\cos\theta (1-\cos\theta)\frac{f(qR)}{(qR)^4} = \frac{1}{2}\frac{\sigma_0}{(\mu v R)^4}\int_0^{2\mu v}\frac{dq}{q} f(qR) \ . \tag{A.16}$$

The dimensionless integral on the RHS provides a logarithmic factor Λ, giving

$$\sigma_{\rm tr} \sim \frac{\Lambda}{(\mu v R)^4}\sigma_0 = \frac{\Lambda}{(kR)^4}\sigma_0 \ . \tag{A.17}$$

Since $\sigma_0 \propto A^2$, we have $\sigma_{\rm tr} \sim A^{2/3}$ for A large enough that $kR \gg 1$ (with Λ changing only logarithmically with kR), as used in Section 3.3.1.2.

The above assumed that the form factor was that appropriate for plane-wave scattering. If both the composite state and the SM scatterer are more localised than the size of the composite state, then the wavefunction overlap in the form factor will not probe the full composite state, giving different results.

A.3.2 Incoherent scattering

As discussed in Section 3.2.1, as well as the collective modes, there may also be low-lying modes corresponding to the excitation of 'single constituents' — in the case of degenerate fermionic matter, excitations in which particles just below the Fermi surface are scattered to just above it. By the usual Fermi-liquid theory, ignoring interactions and approximating the scattering as occurring from a non-interacting Fermi gas should provide a good first approximation. Ref. [167] discusses scattering from a degenerate Fermi gas, finding that the scattering rate for low-energy scatterers is independent of the Fermi momentum (as can be seen from geometrical considerations). This can result in large suppression factors compared to the naive scattering rate given by $\sigma n v$ — for scatterers with momentum $k \ll p_F$, and also low velocity compared to the Fermi velocity, we have an effective suppression (for energy transfer rates) of $\sim \left(\frac{k}{p_F}\right)^4 \frac{m_n^3}{\mu^2 m_X}$, where m_X is the mass of the scatterer, m_n is the effective mass of the quasi-particle, and $\mu = m_X m_n/(m_X + m_n)$ is the reduced mass.

Since the cross sections for scattering off single-particle excitations also add incoherently, $\sigma \propto A$, coherent scattering should dominate unless the size of the state is very large, so that as reviewed in the previous sub-section, the coherent transfer cross section grows slower than A. Making an estimate for SM-like nuclear matter (individual constituents of mass $m_1 = 1\,\mathrm{GeV}$, bulk nuclear matter density $\rho = 1\,\mathrm{GeV}/\,\mathrm{fm}^3$) scattering off solar material, we would need, very roughly, $A \gtrsim 10^{32}$ for incoherent scattering to start dominating the transfer cross section (corresponding to $R \gtrsim 40\,\mu\mathrm{m}$). This is well above the size beyond which thermalisations were found to be ineffective in Section 3.3.1.2. However, it does illustrate why, for example, scattering of DM in neutron stars is dominated by incoherent scattering.

A.4 Statistical identification of rising distributions

Suppose that we have some (one-dimensional) data points, which we assume are independent samples from some probability distribution. We wish to test the hypothesis that this distribution is non-increasing, with respect to some appropriate function of the parameter.

If we expect plausible alternative distributions to feature only one prominent rising segment (for example, the recoil spectra considered in Chapter 3 have successive Bessel function peaks suppressed by both the natural fall-off of the Bessel function, and the velocity distribution), a sensible approach is to locate the interval with the 'worst' bias towards its right-hand end, and ask what the probability is that a given sample from a candidate non-increasing distribution would have an interval 'that extreme'.[1]

A simple measure of how biased an interval is towards its right-hand end is simply the average position of the points within it. The non-increasing distribution maximising the probability of right-biased points is clearly the uniform distribution on the interval. If observations are binned, we can find the exact distribution for the average of bin mid-point positions, for some number n of samples, by performing the convolution of the (binned) uniform distribution on the interval with itself n times. In particular, if the bins are of uniform widths, this distribution can be computed analytically. If observations are not binned, then the distribution for the average of the positions is the (rescaled) Irwin-Hall distribution for n points. In both the discrete and continuous cases, the null distribution is approximately normal for large n, with variance $1/\sqrt{12n}$ (on the interval $[0, 1]$).

So, if we have n samples with a mean position of x (rescaling the interval to be of width 1), we can use the appropriate distribution to find the probability of a mean position $\geq x$ arising from a uniform distribution on that interval. The test statistic for the whole sample is then the minimum such p-value for each sub-interval within the sample (since it is clear that the worst sub-interval will always terminate either at the left sample end, or at the location of a point, there are a finite number of sub-intervals to test). To determine the distribution of this test statistic under a candidate non-increasing distribution, Monte Carlo simulation

---

[1] This would be a poor approach if we expected the rises in the distribution to be e.g. a small periodic signal super-imposed on some larger background, or more generally any small but structured deviation from a larger background.

can be used. A uniform distribution is clearly the non-increasing distribution most likely to produce fake rises, and while the data may indicate that the underlying distribution is far from uniform, for reasonably small numbers of samples the p-values obtained by adopting a uniform null distribution are only slightly worse than those obtained by allowing a free null distribution constrained by the fit to data. In particular, we adopt a uniform null distribution for the calculations in Figure 3.4, and find that the p-values are generally no more than a factor ~ 2 worse.

One issue is that, in many physical cases, there will be some resolution associated with our points. Then, the distribution that our samples are drawn from is some (positive) underlying distribution convolved by a (positive) detector response function, so must be smooth on scales of order the resolution. This means that rightwards bunching on such scales must be spurious, so should not be considered in our test. The simplest way to solve this issue, if we expect rising features in plausible alternative distributions to be on scales larger than the resolution, is to bin the points on around the resolution scale.

Quantitatively, the variance for the average of n uniform random variables on $[0, 1]$ is $\frac{1}{\sqrt{12n}}$, and the expected average position from a linearly rising distribution is $\frac{1}{2} + \frac{1}{6}$, so we would expect to exclude the uniform distribution at a significance of $\sim 0.6\sqrt{n}$ sigma. In the example from Figure 3.4, with 100 events overall, we expect around 26 in the first rise, so we would expect to obtain an exclusion of around 3σ, assuming that the worst intervals arising from the null distribution are of approximately that many events. This is indeed what we observe, with the p-value CDF in the 100-sample case following very closely this normal approximation (the yellow curve in Figure 3.4, lying almost entirely underneath the yellow points). The CDFs for the 30 and 50 sample cases are not so well approximated, since the 'worst interval' is more variable with small numbers of events.

A.5 Solar capture of heavy WIMPS

Here, we give a very brief review of the capture of weakly-interacting, massive dark matter particles by the Sun. For X particles much heavier than any of the relevant SM nuclei within the Sun (here, this means $m_X \gtrsim 400\,\mathrm{GeV}$), the rate of capture by the Sun scales as $C_\odot \sim \sigma_{Xn} \rho_X m_X^{-2}$, where σ_{Xn} is the scattering cross section with SM nucleons (assumed to be elastic and spin-independent) [238, 239].[2] Summing over capture rates from the various elements in the Sun (the main contributions are from the CNO elements) using a standard solar model [240], we obtain

$$C_\odot \simeq 3 \times 10^{19}\,\mathrm{sec}^{-1} \left(\frac{\sigma_{Xn}}{10^{-8}\,\mathrm{pb}}\right) \left(\frac{1\,\mathrm{TeV}}{m_X}\right)^2 , \tag{A.18}$$

(taking the couplings to protons and neutrons to be the same). We have assumed that the DM velocity distribution follows the Standard Halo Model—since, for high-mass WIMPs, only the low-velocity part of the distribution can be captured by scattering events, modifications that affect the low-velocity distribution will alter the capture rate. Direct detection experiments imply that $\sigma_{Xn} \lesssim 10^{-8}\,\mathrm{pb}\frac{m_X}{1\,\mathrm{TeV}}$ [241], and the age of the Sun is $t_\odot \simeq 5\,\mathrm{Gyr}$, so the number of X particles captured is $\lesssim 5 \times 10^{36} \left(\frac{1\,\mathrm{TeV}}{m_X}\right)$. As a fraction of the total flux of X particles hitting the Sun, we capture $\sim 3 \times 10^{-7} \left(\frac{\sigma_{Xn}/m_X}{10^{-8}\,\mathrm{pb}/\,\mathrm{TeV}}\right)$.

Here, 'captured' means that the X particles are in gravitationally bound orbits passing through the Sun. Subsequent scatterings with material in the Sun will reduce the size of these orbits further, and eventually the X particles will (ignoring other interactions) settle into an isothermal distribution $\rho_X \sim e^{-r/(2r_\star^2)}$, with [242]

$$r_\star = \left(\frac{3T_\odot}{4\pi G m_X \rho_\odot}\right)^{1/2} \simeq 2 \times 10^{-3} R_\odot \left(\frac{\mathrm{TeV}}{m_X}\right)^{1/2} \left(\frac{T_\odot}{10^7\,\mathrm{K}}\right)^{1/2} \left(\frac{150\,\mathrm{g\,cm^{-3}}}{\rho_\odot}\right)^{1/2} , \tag{A.19}$$

---

[2] One factor of m_X^{-1} comes from the number density $n_X = \rho_X m_X^{-1}$, while another arises from the fact that heavier particles lose a smaller fraction of their kinetic energy in collisions with SM nuclei, so only the low-speed part of the WIMP velocity distribution can be captured. This also assumes that σ_{Xn} is low enough that the Sun is optically thin to X particles, which is the case for $\sigma_{Xn} \lesssim 10^{-3}\,\mathrm{pb}$.

(where the temperature and density are appropriate to the solar core). If $m_X \ll 100\,\mathrm{TeV}$, then the initial orbits will be small enough that planetary perturbations can be mostly neglected, and then thermalisation occurs in less than the lifetime of the Sun if $\sigma_{Xn} \gtrsim 3 \times 10^{-13}\,\mathrm{pb}\,(m_X/\,\mathrm{TeV})^{3/2}$ [243]. For larger m_X, most of the initial orbits are large enough that the effect of Jupiter perturbs them so that they no longer pass through the Sun, resulting in most of them never thermalising [243].

The above calculations apply to the case of capture by elastic, momentum-independent scattering with SM nuclei. If scattering is momentum-dependent, or there are sufficiently low-lying excitations that inelastic scatterings are possible, this may alter the possible parameter space.

A.6 Effect of approximations to DM halo distributions

In Section 4.1, which considered effects of a non-relativistic velocity kick on a small proportion of DM particles in galactic halos, we made the approximation that both the starting distribution and the gravitational potential were spherically symmetric and static (and that the starting distribution was non-rotating). Though this ignores various effects, their impact should be minor for the case of DM in galactic halos:

- *The evolution of the galactic potential with time*: most obviously, particles injected before matter has collapsed into galaxies will not behave as outlined, and may be captured into galaxies later if their velocity is sufficiently low. These will then have the same distribution as the 'parent' particles.

  We can put a rough upper bound on this effect, for the particular case of particles emitted by X decay, by estimating the proportion of the early-emitted Y that are captured into galaxies. Free-streaming with a velocity u suppresses perturbations on conformal scales with $k > H(t)a(t)/u(t)$, as such particles will escape potential wells. Since Hubble expansion reduces the velocity of non-relativistic particles as $1/a$, we have $u(t) = u(t_1)a(t)/a(t_1)$, where t_1 is the time of injection, and $u(t_1)$ is the velocity kick. So, the critical k at the present time is $k_c = \frac{H_0 a(t_1)}{u(t_1)}$. If $k_c \lesssim 100$ kpc, the scale relevant to galaxies, then the injected particles will never have clustered into galaxies. Conversely, only states emitted with $a(t_1) \lesssim H_0 u(t_1)^{-1}/(100\,\mathrm{kpc})$ will cluster. During matter domination, $a \sim t^{2/3}$, and since $H_0/(100\,\mathrm{kpc}) \simeq 7\,\mathrm{km\,s^{-1}}$, it follows that for a Y to be captured it must be produced prior to

$$t_1 \lesssim \left(\frac{7\,\mathrm{km\,s^{-1}}}{u(t_1)}\right)^{3/2} t_0 \ . \tag{A.20}$$

Taking example velocity kicks from earlier plots, if $u(t_1) \approx 70\,\mathrm{km\,s^{-1}}$, around 3% of the Y emitted cluster in this way, and taking $u(t_1) \approx 220\,\mathrm{km\,s^{-1}}$ gives $\sim 5 \times 10^{-3}$ of the $\overline{L'}$ with the 'parent' distribution. From inspection of Figure 4.1, the modified distribution is always a significantly larger fraction of the original density than those values.

- *The shape of the DM halo*: simulations and observations favour ellipsoidal halos, but with a ratio of longest/shortest axes around 0.6, rather than more extreme values (see e.g. [244, 245]).

- *Angular momentum of the DM halo*: simulations indicate that the velocity bias due to net rotation is insignificant compared to the velocity dispersion (see e.g. [246]), so should not give a large effect.

- *The potential of the galactic disk*: there is a degeneracy between the contribution of the halo and the disk to the mass of the inner few parsecs of the galaxy [169]. As a result, in the cases where the velocity kick has most effect (i.e. DM profiles with a central density cusp to be smoothed out) the contribution of the disk is less important.

A.7 Rates of B' and L' violating processes

In Chapter 4, we assumed that all B' and L' violating processes apart from the (slow) $B' \to \overline{L'} + \cdots$ decay can be neglected. Here, we justify this assumption and estimate the rates of various processes.

Suppose that B' and L' are good symmetries at low energies, and are only violated at some high scale $M_{\not{B}'}$. The decay of B' is then described by a contact operator $\frac{1}{\Lambda^k} B' L' \mathcal{O}_{k+1}$, where we assume that B' and L' are fermions, and so $\mathcal{O}_{k+1}$ is a dimension $k+1$ operator. The small mass splitting Δm between B' and L' will result in a phase-space suppression of the decay width, and there may be additional Δm factors depending on the operator $\mathcal{O}_{k+1}$. Dimensionally, a dim-$(4+k)$ operator will give a total width going parametrically as $(\Delta m)^{2k+1}$ (or $(\Delta m)^{2k+3}$ if the $B'L'$ current gives another $(\Delta m)^2$). For example, a dimension-6 operator will, in the former case, give a total width of

$$\Gamma \sim \frac{(\Delta m)^5}{\Lambda^4} \ . \tag{A.21}$$

In contrast, symmetry-violating annihilations (for instance $B' + L' \to \cdots$) at high temperatures will not be suppressed, and for a dim-$(4+k)$ operator will have $\sigma \sim \frac{T^{2k-2}}{\Lambda^{2k}}$. Hence, in the early universe, the rate of such interactions will be $n_{L'}\langle \sigma v \rangle \sim \frac{T^{2k+1}}{\Lambda^{2k}}$. So, for T much larger than Δm, there is the possibility that these will be fast enough to affect the asymmetries in B' and L' (if these are established above that temperature).

Specifically, since $B' - L'$ is a good symmetry (ignoring processes that only respect the full $B - L - (B' - L')$), we will have $\eta_{B'} - \eta_{L'} =$ constant. By symmetry, the Boltzmann equation for the other linear combination $\eta_{B'} + \eta_{L'}$ is

$$\frac{d(\eta_{B'} + \eta_{L'})}{dx} = -\lambda(x)(\eta_{B'} + \eta_{L'}) \ , \tag{A.22}$$

to leading order in the small asymmetries, where $x \propto 1/T$. So, if λ is large enough, the asymmetries will be driven towards $\eta_{B'} = -\eta_{L'}$, corresponding to a population of B' and $\overline{L'}$ (or the reverse, depending on the sign of $\eta_{B'} - \eta_{L'}$). This would not permit the scenarios we discussed in the main text, where the asymmetries have the same sign. It may be possible to build models in which B' and $\overline{L'}$ populations give rise to the decay-followed-by-annihilation signals considered in the phenomenological sections of this paper (for example, through $B' \to L' + \nu\nu + \cdots$ type decays which conserve $B - L - (B' - L')$), but we do not go into any model-building details here.

To check more quantitatively whether this asymmetry-reversal will be important, we take as an example the model of Appendix A.9, which has (schematically) the symmetry-violating operator $\frac{1}{\Lambda^2}(B'L')(N_1^\dagger N_2^\dagger)$. This leads to a three-body decay, with differential width

$$d\Gamma = \frac{1}{2m_{B'}} |\mathcal{A}|^2 dq^2 \frac{d\Omega_{\rm CM}}{16\pi^2} \frac{|\vec{p}_{\rm CM}|}{m_{B'}} \frac{1}{2\pi} \frac{d\Omega_N}{16\pi^2} \frac{|\vec{p}_N|}{\sqrt{q^2}} \ , \tag{A.23}$$

where q is the total 4-momentum of N_1 and N_2, and the subscript-N quantities are in the frame where q is purely timelike. Neglecting the masses of N_1 and N_2, and assuming that Δm is small, we have $\vec{p}_{\rm CM}^{\,2} \approx (\Delta m)^2 - q^2$. Also, $|\mathcal{A}|^2 \approx \frac{4}{\Lambda^4} m_{B'}^2 q^2$ (summing over final spins), so overall,

$$\Gamma \approx \frac{1}{4\pi m_{B'}} \int_0^{(\Delta m)^2} dq^2 \, \frac{1}{4\pi} \frac{\sqrt{(\Delta m)^2 - q^2}}{m_{B'}} \frac{1}{8\pi} \frac{4}{\Lambda^4} m_{B'}^2 q^2 \tag{A.24}$$

$$= \frac{1}{(4\pi)^3} \frac{8}{15} \frac{(\Delta m)^5}{\Lambda^4} \ . \tag{A.25}$$

In the early universe, symmetry-violating processes of the form $B' + L' \to N_1 + N_2$, $B' + N_1 \to \overline{L'} + N_1$, etc. will be active. The associated annihilation cross sections are

$$\sigma \approx C \frac{1}{8E^2} \frac{1}{8\pi} \frac{1}{\Lambda^4} E^4 \ , \tag{A.26}$$

where $E \gg m_{B'}$ is the energy of each particle in the CoM frame, and C is a numerical constant depending on which legs are ingoing and outgoing. Thus, in a thermal bath at temperature $T \gg m_{B'}$, we have the thermally averaged cross section [247]

$$\langle \sigma v \rangle \approx \frac{3}{32\pi} C \frac{T^2}{\Lambda^4} \equiv C\sigma_1 \frac{T^2}{T_1^2} \ , \tag{A.27}$$

where T_1 is some (high) temperature. The Boltzmann equation is then (to leading order) of the form

$$\frac{1}{a^3}\frac{d}{dt}\Big[a^3\big((n_{B'} - n_{\overline{B'}}) + (n_{L'} - n_{\overline{L'}})\big)\Big] = -C' n_{N_1}(T)\sigma_1 \frac{T^2}{T_1^2}\Big[(n_{B'} - n_{\overline{B'}}) + (n_{L'} - n_{\overline{L'}})\Big] \ , \tag{A.28}$$

where C' is a numerical constant obtained from summing over all of the leg orderings, with the appropriate weights (its value is $\mathcal{O}(10)$). Converting to conserved variables $Y_i = n_i/s$, and letting $x = T_1/T$, this becomes

$$\frac{d(\eta_{B'} + \eta_{L'})}{dx} = -\frac{\lambda}{x^4}\sqrt{g_*(T)}\, Y_{N_1}(\eta_{B'} + \eta_{L'}) \ , \tag{A.29}$$

with

$$\lambda \simeq 1.32 \times C' T_1 M_{\rm Pl} \sigma_1 \ , \tag{A.30}$$

where we have used that during the radiation-dominated era, the Hubble rate is given by $H = \frac{T^2}{M^*_{\rm Pl}}$, where $M^*_{\rm Pl} = M_{\rm Pl}\sqrt{\frac{90}{\pi^2 g_\star(T)}}$. So, in terms of the B' decay rate Γ, we find that

$$\lambda = 3\pi^3 \sqrt{\frac{5}{2}}\, C' \frac{T_1^3 M_{\rm pl}\Gamma}{(\Delta m)^5} \ . \tag{A.31}$$

So, if $T^3 \gtrsim 10^{-3}\frac{(\Delta m)^5}{\Gamma M_{\rm pl}}$, then $\eta_{B'} + \eta_{L'}$ will be suppressed by multiple e-folds. Taking some representative values, for $\Gamma \sim 1/t_0$ and $\Delta m \sim 10\,\mathrm{MeV}$, we find that this corresponds to $T \gtrsim 3\,\mathrm{TeV}$. For the models proposed here to be successfully realised, it is required that the B' and L' asymmetries are established at some point after the universe has cooled below this temperature.

Further, our assumption that the asymmetries are set before B', L' freeze-out from the thermal bath, i.e. roughly before they become non-relativistic, implies a lower limit on Δm, or equivalently, an upper limit on Γ. For example, for

$\Gamma = 1/t_{\rm CMB}$ it is required that $\Delta m \gtrsim 7\,{\rm MeV}$, otherwise symmetry-violating interactions do not decouple until $T \lesssim 50\,{\rm GeV}$. This limit is plotted in Figure 4.4, demonstrating that there is viable parameter for all cosmologically slow decay rates.

There is also the possibility of symmetry-violating interactions at late times, but the number densities then are small enough to make these completely negligible. The most frequent will be those involving a N particle, since (in the simplest case) these decouple from the thermal bath when the symmetry-violating interactions discussed above decouple, forming a dark radiation component (the large difference between g_* at the time of decoupling and later means that this does not conflict with constraints on $N_{\rm eff}$ from BBN and the CMB). The N will have a number density of $\sim n_\gamma/8$, where $n_\gamma \approx 400\,{\rm cm}^{-3} \approx (10^{-10}\,{\rm MeV})^3$ is the photon number density today, so the rate of e.g. $B' + N_1 \to \overline{L'} + N_2$ interactions will be much smaller than the rate of $B' \to \overline{L'} + N_1 + N_2$ decays, since $(\Delta m)^3 \gg n_\gamma$. Note that this scenario is only viable for small enough N masses — if the mass were large enough that early decoupling would give too large a relic density, we would need some other mechanism to reduce the eventual abundance (e.g. annihilation to lighter states).

A.8 B'-L' mass splitting and $\overline{L'}$ injection velocity

As discussed in Section 4.2.3, if the $B' \to \overline{L'} + \cdots$ decay has more than two decay products, then we will obtain a distribution of final velocities for the $\overline{L'}$. In particular, a fraction of them will obtain velocities higher than some critical value v_c (e.g. the escape velocity of a bound structure). Here, we estimate this fraction, and confirm that for mass splittings $m_{B'} - m_{L'} \equiv \Delta m$ larger than $m_{L'} v_c$ it is very close to 1, assuming that none of the final or intermediate states (other than $\overline{L'}$) have masses close to Δm.

In the $B' \to \overline{L'} + \cdots$ decay, if the other decay products carry away 4-momentum

q, the velocity given to $\overline{L'}$ corresponds to a Lorentz factor γ of

$$\gamma - 1 = \frac{(\Delta m)^2 - q^2}{2m_{B'}m_{L'}} \ , \tag{A.32}$$

so if $\Delta m = m_B - m_L$ is small, the velocity is

$$v^2 = \frac{(\Delta m)^2 - q^2}{m_{L'}^2} + O\left(\left(\frac{\Delta m}{m_{L'}}\right)^3\right) + O(v^4) \ . \tag{A.33}$$

For a two-body decay $B \to \overline{L} + X$, assuming that m_X is small compared to Δm gives $v \approx \frac{\Delta m}{m_{L'}}$. For a higher-multiplicity final state, some fraction of the decays will result in $v < v_c$, i.e. those for which q^2 is only just below $(\Delta m)^2$. We can write the differential decay width to a n-body final state as

$$\mathrm{d}\Gamma = \frac{(2\pi)^4}{2M}|\mathcal{A}|^2\mathrm{d}\Phi_n(P; p_1, \ldots, p_n) \ , \tag{A.34}$$

where M is the mass of the decaying particle, $\mathcal{A}$ is the amplitude for that particular decay, and $\mathrm{d}\Phi_n$ is the differential phase space element for initial momentum P and final momenta $p_1, \ldots, p_n$. Also, we have

$$\mathrm{d}\Phi_n(P; p_1, \ldots, p_n) = (2\pi)^3\mathrm{d}q^2\mathrm{d}\Phi_2(P; p_1, q)\mathrm{d}\Phi_{n-1}(q; p_2, \ldots, p_n) \ , \tag{A.35}$$

splitting the decay into an initial two-body step and then a fragmentation of the second body. In the rest frame of the decaying particle, the two-body phase space element has the form $\mathrm{d}\Phi_2 \propto \mathrm{d}\Omega\frac{|\vec{p}|}{E}$. From above, for small Δm we have $|\vec{p}|^2 \approx (\Delta m)^2 - q^2$, so writing $q^2 = (\Delta m)^2 - \delta q^2$, the leading order behaviour of $\mathrm{d}\Phi_2$ with δq^2 is $\sqrt{\delta q^2}$. Since the mass dimension of $\mathrm{d}\Phi_n$ is $2n-4$, if the total mass of the other decay particles is small compared to $\sqrt{\delta q^2}$, then $\mathrm{d}\Phi_{n-1}$ must vary like $(\delta q^2)^{n-3}$. So overall, $\mathrm{d}\Phi_n$ will vary as $(\delta q^2)^{n-3/2}$.

The phase space volume with $v < v_c$ corresponds to that with δq^2 below a critical value, and we want to compare the total width for that volume to the total width overall. If we do not have intermediate states with masses close to Δm (heavier states have a roughly constant effect on $|\mathcal{A}|$, while lighter states enhance it towards smaller q^2), then we can obtain an approximate upper bound on the ratio of widths by comparing the phase space volumes. From above, as long as the other final state masses are small compared to Δm, this will be well approximated by $\left(\frac{\delta q^2}{(\Delta m)^2}\right)^{n-3/2}$.

To take an example, suppose that $m_{B'} = 20$ GeV, $m_{L'} = 10$ GeV, and $v_c = 500$ kms^{-1}, and that the decay is $B' \to \overline{L'} + \phi + \phi$, where the ϕ are massless states. Then, $v < v_c$ corresponds to $\delta q^2 < 5.6 \times 10^{-2}$ GeV^2, which is 1.27×10^{-8} of the three-body phase space, while $\left(\frac{\delta q^2}{(\Delta m)^2}\right)^{3/2} = 1.31 \times 10^{-8}$. Since $v^2 \approx \frac{\delta q^2}{m_{L'}^2}$, in general our volume ratio is $\left(\frac{m v_c}{\Delta m}\right)^{2n-3}$ (for $\Delta m > m v_c$; otherwise, the whole of the phase space volume corresponds to a velocity kick $< v_c$).

A.9 Model-building the B',L' splitting

It was argued in Section 4.2 that a small mass splitting is a natural way to obtain observable annihilation signals. Here, we highlight a motivated setting in which such a scenario may occur, in a model based on broken flavour symmetries in the hidden sector.

We present a simple implementation involving (fundamental) matter that obtains Dirac masses, with a small mass splitting generated from radiative breaking of a flavour symmetry. The hidden sector has a Z_2 symmetry, an exact $B - L - (B' - L')$ symmetry, and accidental approximate B' and L' symmetries.[3] The matter content of our (example) model is displayed in Table A.1; it features a heavy complex scalar ϕ and fermion matter, which is written as two component left-handed Weyl spinors. The typical mass hierarchy of the states is displayed to the right of Table A.1.

---

[3] The couplings studied here actually respect $B' - L'$, however once a mechanism to cogenerate or share asymmetries with the visible and hidden sectors is included, the true symmetry is $B - L - (B' - L')$.

	spin	Z_2	B'	L'	$B'-L'$
ϕ	0	1	–	–	0
${B'}_{L\alpha}$	$\frac{1}{2}$	1	1/2	0	1/2
${B'}^{\dagger}_{R\alpha}$	$\frac{1}{2}$	1	−1/2	0	−1/2
${L'}_{L\alpha}$	$\frac{1}{2}$	0	0	1/2	−1/2
${L'}^{\dagger}_{R\alpha}$	$\frac{1}{2}$	0	0	−1/2	1/2
$N_{1\alpha}$	$\frac{1}{2}$	1	0	0	0
$N_{2\alpha}$	$\frac{1}{2}$	0	0	0	0

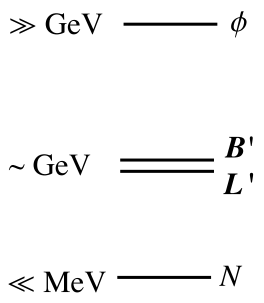

Table A.1: ***Left:*** hidden sector fundamental matter content. ***Right:*** hidden sector mass hierarchy.

The Lagrangian involving the light fields can be expressed as

$$\mathcal{L} \supset -m_{B'} B'_{L\alpha} {B'}^{\alpha\,\dagger}_{R} - m_{L'} L'_{L\alpha} {L'}^{\alpha\,\dagger}_{R} + \text{h.c.} \tag{A.36}$$

Note that Majorana mass terms for L', B' are forbidden by the exact $B-L-(B'-L')$ symmetry and mixing between these states is forbidden by the Z_2 symmetry. It can be seen that B' and L' arise as approximate symmetries since there are no renormalisable terms in the low energy effective theory that violate them. However, the heavy scalar ϕ has couplings of the form

$$\mathcal{L} \supset y_1 \phi \left(B^{\alpha}_{L} L_{L\alpha} + B_{R\dot{\alpha}} L^{\dot{\alpha}}_{R} \right) + y_2 \phi N^{\alpha}_{1} N_{2\alpha} + \text{h.c.} \tag{A.37}$$

As a result, this can mediate decays of B' to $\overline{L'}$ as shown in Figure A.1. We shall assume that the scalar ϕ gains a mass well above B' and L' and hence can be integrated out, leading to a four-fermion operator. The lifetime of B' is given in equation (4.10), setting $M_{\not{B}'} = m_{\phi}$ and hence, for a given model, one can compare with the limits indicated in Figure 4.3.

The fields N_1 and N_2 are assumed to gain Majorana masses M_1 and M_2,

$$\mathcal{L} \supset -M_1 N_{1\alpha} N^{\alpha}_{1} - M_2 N_{2\alpha} N^{\alpha}_{2} + \text{h.c.}\ , \tag{A.38}$$

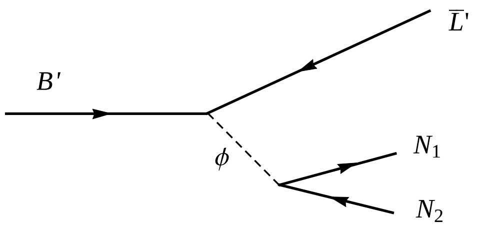

Figure A.1: $\overline{L'}$ are generated via B' decays and then annihilate with the asymmetric population of L'.

which are parametrically smaller than the B' and L' (Dirac) mass scale.[4] Further, we assume that $m_{B'} = m_{L'}$ at leading order, exhibiting an approximate 'flavour' symmetry which is only radiatively broken. This breaking could be due to the differing Z_2 parities of these states, resulting in the B' and L' having different couplings to some additional (possibly heavy) matter content in the theory. Alternatively, we could introduce an additional gauge group to the low energy theory, under which the B' and L' have differing charges. Such a soft breaking of the Z_2 flavour symmetry will lead to a small mass splitting between B' and L', similar to that employed in models of inelastic DM [248] and eXcited DM [249].

To provide a portal to the SM, we can introduce an additional gauge boson, Z', under which the states L' (and B') are charged. Provided this has the appropriate mass (through an additional scalar, that we do not specify, gaining a vacuum expectation value) annihilation of L' and $\overline{L'}$ proceeds to two on-shell Z'. If the states N_1 and N_2 are uncharged under this symmetry, and there are no other lighter hidden sector states to which the Z' can decay, then it will be approximately stable. Decay of the Z' to the SM can then occur through, for example, a small amount of kinetic mixing with the SM hypercharge U(1). Alternatively, it is straightforward to introduce an additional pseudoscalar in the theory that couples to the states L'. This can then act as a portal if it also couples to the SM quarks, leading to a model of the form of Section 4.2.6.

---

[4] As mentioned in Appendix A.7, if N_1 and N_2 do not have other interactions, then their masses must generally be ($< \mathcal{O}(\text{eV})$) to avoid having too large a relic density.

While in the model presented here the decay of B' to $\overline{L'} + \cdots$ is mediated through a heavy scalar, there are also well motivated scenarios where this occurs through a heavy vector. In particular, if B' and $\overline{L'}$ appear in the same multiplet in a (spontaneously broken) GUT theory, this decay may be mediated through a gauge boson charged under the Z_2 symmetry, analogous to the X, Y bosons that appear in SM GUTs. In this case, the Z_2 symmetry must also arise as a discrete remnant of part of the hidden sector GUT gauge group, so that the states B' and $\overline{L'}$ can have differing charges under this.

BIBLIOGRAPHY

[1] G. Bertone, D. Hooper, and J. Silk, *Particle dark matter: Evidence, candidates and constraints*, *Phys.Rept.* **405** (2005) 279–390, [`hep-ph/0404175`].

[2] S. Dodelson, *Modern Cosmology.* Academic Press. Academic Press, 2003. ISBN: 9780122191411.

[3] E. W. Kolb and M. S. Turner, *The Early Universe.* Addison-Wesley, 1990. Frontiers in Physics, 69.

[4] D. Baumann, *Cosmology, Part III Mathematical Tripos*, 2014. `http://www.damtp.cam.ac.uk/user/db275/Cosmology/Lectures.pdf`.

[5] M. Richmond, *Astrophysics I (Phys440) course notes*, 2003. `http://spiff.rit.edu/classes/phys440/lectures/gal_clus/gal_clus.html`.

[6] K. G. Begeman, A. H. Broeils, and R. H. Sanders, *Extended rotation curves of spiral galaxies - Dark haloes and modified dynamics*, *MNRAS* **249** (Apr., 1991) 523–537.

[7] S. S. Vogt, M. Mateo, E. W. Olszewski, and M. J. Keane, *Internal kinematics of the Leo II dwarf spherodial galaxy*, *AJ* **109** (Jan., 1995) 151–163.

[8] J. J. Adams, J. D. Simon, M. H. Fabricius, R. C. van den Bosch, J. C. Barentine, et al., *Dwarf Galaxy Dark Matter Density Profiles Inferred from Stellar and Gas Kinematics*, *Astrophys.J.* **789** (2014) 63, [`arXiv:1405.4854`].

[9] D. Zaritsky, R. Smith, C. Frenk, and S. D. White, *More satellites of spiral galaxies*, *Astrophys.J.* **478** (1997) 39–48, [`astro-ph/9611199`].

[10] X.-P. Wu, T. Chiueh, L.-Z. Fang, and Y.-J. Xue, *A comparison of different cluster mass estimates: consistency or discrepancy ?*, *Mon.Not.Roy.Astron.Soc.* **301** (1998) 861, [`astro-ph/9808179`].

[11] A. Vikhlinin, A. Kravtsov, W. Forman, C. Jones, M. Markevitch, et al., *Chandra sample of nearby relaxed galaxy clusters: Mass, gas fraction, and mass-temperature relation*, *Astrophys.J.* **640** (2006) 691–709, [`astro-ph/0507092`].

[12] E. Fomalont, S. Kopeikin, G. Lanyi, and J. Benson, *Progress in Measurements of the Gravitational Bending of Radio Waves Using the VLBA*, *Astrophys.J.* **699** (2009) 1395–1402, [`arXiv:0904.3992`].

[13] D. Clowe, M. Bradac, A. H. Gonzalez, M. Markevitch, S. W. Randall, et al., *A direct empirical proof of the existence of dark matter*, *Astrophys.J.* **648** (2006) L109–L113, [`astro-ph/0608407`].

[14] F. Iocco, G. Mangano, G. Miele, O. Pisanti, and P. D. Serpico, *Primordial Nucleosynthesis: from precision cosmology to fundamental physics*, *Phys.Rept.* **472** (2009) 1–76, [`arXiv:0809.0631`].

[15] G. Steigman, *Primordial Nucleosynthesis in the Precision Cosmology Era*, *Ann.Rev.Nucl.Part.Sci.* **57** (2007) 463–491, [`arXiv:0712.1100`].

[16] W. Hu, *Lecture Notes on CMB Theory: From Nucleosynthesis to Recombination*, `arXiv:0802.3688`.

[17] **Planck** Collaboration, P. Ade et al., *Planck 2015 results. XIII. Cosmological parameters*, `arXiv:1502.01589`.

[18] S. Trujillo-Gomez, A. Klypin, J. Primack, and A. J. Romanowsky, *Galaxies in LCDM with Halo Abundance Matching: luminosity-velocity relation, baryonic mass-velocity relation, velocity function and clustering*, *Astrophys.J.* **742** (2011) 16, [`arXiv:1005.1289`].

[19] **BOSS** Collaboration, L. Anderson et al., *The clustering of galaxies in the SDSS-III Baryon Oscillation Spectroscopic Survey: Baryon Acoustic Oscillations in the Data Release 10 and 11 galaxy samples*, *Mon.Not.Roy.Astron.Soc.* **441** (2014) 24–62, [`arXiv:1312.4877`].

[20] M. Viel, G. D. Becker, J. S. Bolton, M. G. Haehnelt, M. Rauch, et al., *How cold is cold dark matter? Small scales constraints from the flux power spectrum of the high-redshift Lyman-alpha forest*, *Phys.Rev.Lett.* **100** (2008) 041304, [`arXiv:0709.0131`].

[21] G. B. Gelmini, *TASI 2014 Lectures: The Hunt for Dark Matter*, `arXiv:1502.01320`.

[22] A. Boyarsky, O. Ruchayskiy, and D. Iakubovskyi, *A Lower bound on the mass of Dark Matter particles*, *JCAP* **0903** (2009) 005, [`arXiv:0808.3902`].

[23] S. W. Randall, M. Markevitch, D. Clowe, A. H. Gonzalez, and M. Bradac, *Constraints on the Self-Interaction Cross-Section of Dark Matter from Numerical Simulations of the Merging Galaxy Cluster 1E 0657-56*, *Astrophys. J.* **679** (2008) 1173–1180, [`arXiv:0704.0261`].

[24] D. Harvey, R. Massey, T. Kitching, A. Taylor, and E. Tittley, *The non-gravitational interactions of dark matter in colliding galaxy clusters*, `arXiv:1503.07675`.

[25] F. Sanchez-Salcedo, *The Dark halo of NGC 5963 as a constraint on dark matter self-interaction at the low velocity regime*, *Astrophys.J.* **631** (2005) 244–251, [`astro-ph/0506345`].

[26] M. Vogelsberger, J. Zavala, C. Simpson, and A. Jenkins, *Dwarf galaxies in CDM and SIDM with baryons: observational probes of the nature of dark matter*, *Mon.Not.Roy.Astron.Soc.* **444** (2014) 3684, [`arXiv:1405.5216`].

[27] J. Fan, A. Katz, L. Randall, and M. Reece, *Double-Disk Dark Matter*, *Phys.Dark Univ.* **2** (2013) 139–156, [`arXiv:1303.1521`].

[28] R. Foot and S. Vagnozzi, *Dissipative hidden sector dark matter*, *Phys.Rev.* **D91** (2015), no. 2 023512, [`arXiv:1409.7174`].

[29] M.-Y. Wang and A. R. Zentner, *Weak Gravitational Lensing as a Method to Constrain Unstable Dark Matter*, *Phys.Rev.* **D82** (2010) 123507, [`arXiv:1011.2774`].

[30] A. H. Peter and A. J. Benson, *Dark-matter decays and Milky Way satellite galaxies*, *Phys.Rev.* **D82** (2010) 123521, [`arXiv:1009.1912`].

[31] M.-Y. Wang and A. R. Zentner, *Effects of Unstable Dark Matter on Large-Scale Structure and Constraints from Future Surveys*, *Phys.Rev.* **D85** (2012) 043514, [`arXiv:1201.2426`].

[32] M.-Y. Wang, R. A. Croft, A. H. Peter, A. R. Zentner, and C. W. Purcell, *Lyman- forest constraints on decaying dark matter*, *Phys.Rev.* **D88** (2013), no. 12 123515, [`arXiv:1309.7354`].

[33] M. Taoso, G. Bertone, and A. Masiero, *Dark Matter Candidates: A Ten-Point Test*, *JCAP* **0803** (2008) 022, [`arXiv:0711.4996`].

[34] D. M. Jacobs, G. D. Starkman, and B. W. Lynn, *Macro Dark Matter*, *Mon.Not.Roy.Astron.Soc.* (2014) [`arXiv:1410.2236`].

[35] G. D. Mack, J. F. Beacom, and G. Bertone, *Towards Closing the Window on Strongly Interacting Dark Matter: Far-Reaching Constraints from Earth's Heat Flow*, *Phys.Rev.* **D76** (2007) 043523, [`arXiv:0705.4298`].

[36] G. D. Starkman, A. Gould, R. Esmailzadeh, and S. Dimopoulos, *Opening the Window on Strongly Interacting Dark Matter*, *Phys.Rev.* **D41** (1990) 3594.

[37] P. Natarajan, A. Loeb, J.-P. Kneib, and I. Smail, *Constraints on the collisional nature of the dark matter from gravitational lensing in the cluster a2218*, *Astrophys.J.* **580** (2002) L17–L20, [`astro-ph/0207045`].

[38] X.-l. Chen, S. Hannestad, and R. J. Scherrer, *Cosmic microwave background and large scale structure limits on the interaction between dark matter and baryons*, *Phys.Rev.* **D65** (2002) 123515, [`astro-ph/0202496`].

[39] R. H. Cyburt, B. D. Fields, V. Pavlidou, and B. D. Wandelt, *Constraining strong baryon dark matter interactions with primordial nucleosynthesis and cosmic rays*, *Phys.Rev.* **D65** (2002) 123503, [`astro-ph/0203240`].

[40] J. Rich, R. Rocchia, and M. Spiro, *A Search for Strongly Interacting Dark Matter*, *Phys.Lett.* **B194** (1987) 173.

[41] B. D. Wandelt, R. Dave, G. R. Farrar, P. C. McGuire, D. N. Spergel, et al., *Selfinteracting dark matter*, `astro-ph/0006344`.

[42] A. L. Erickcek, P. J. Steinhardt, D. McCammon, and P. C. McGuire, *Constraints on the Interactions between Dark Matter and Baryons from the X-ray Quantum Calorimetry Experiment*, *Phys.Rev.* **D76** (2007) 042007, [`arXiv:0704.0794`].

[43] **CDMS-II** Collaboration, D. Akerib et al., *Limits on WIMP-nucleon interactions from the Cryogenic Dark Matter Search at the Soudan Underground Laboratory*, *Nucl.Instrum.Meth.* **A559** (2006) 390–392.

[44] I. F. Albuquerque and L. Baudis, *Direct detection constraints on superheavy dark matter*, *Phys.Rev.Lett.* **90** (2003) 221301, [`astro-ph/0301188`].

[45] **EDELWEISS** Collaboration, V. Sanglard et al., *Final results of the EDELWEISS-I dark matter search with cryogenic heat-and-ionization Ge detectors*, *Phys.Rev.* **D71** (2005) 122002, [`astro-ph/0503265`].

[46] R. Bernabei, P. Belli, R. Cerulli, F. Montecchia, M. Amato, et al., *Extended limits on neutral strongly interacting massive particles and nuclearites from NaI(Tl) scintillators*, *Phys.Rev.Lett.* **83** (1999) 4918–4921.

[47] H. An, M. Pospelov, J. Pradler, and A. Ritz, *Direct Detection Constraints on Dark Photon Dark Matter*, `arXiv:1412.8378`.

[48] D. H. Weinberg, J. S. Bullock, F. Governato, R. K. de Naray, and A. H. G. Peter, *Cold dark matter: controversies on small scales*, `arXiv:1306.0913`.

[49] M. Boylan-Kolchin, J. S. Bullock, and M. Kaplinghat, *The Milky Way's bright satellites as an apparent failure of LCDM*, *Mon.Not.Roy.Astron.Soc.* **422** (2012) 1203–1218, [`arXiv:1111.2048`].

[50] S. E. Koposov, V. Belokurov, G. Torrealba, and N. W. Evans, *Beasts of the Southern Wild. Discovery of a large number of Ultra Faint satellites in the vicinity of the Magellanic Clouds*, `arXiv:1503.02079`.

[51] M. Boylan-Kolchin, J. S. Bullock, and M. Kaplinghat, *Too big to fail? The puzzling darkness of massive Milky Way subhaloes*, *Mon.Not.Roy.Astron.Soc.* **415** (2011) L40, [`arXiv:1103.0007`].

[52] J. F. Navarro, C. S. Frenk, and S. D. White, *The Structure of cold dark matter halos*, *Astrophys.J.* **462** (1996) 563–575, [`astro-ph/9508025`].

[53] W. de Blok, *The Core-Cusp Problem*, *Adv.Astron.* **2010** (2010) 789293, [`arXiv:0910.3538`].

[54] A. Pontzen and F. Governato, *Cold dark matter heats up*, *Nature* **506** (2014) 171–178, [`arXiv:1402.1764`].

[55] J. Silk and G. A. Mamon, *The Current Status of Galaxy Formation*, *Res.Astron.Astrophys.* **12** (2012) 917–946, [`arXiv:1207.3080`].

[56] S. S. McGaugh, J. M. Schombert, G. D. Bothun, and W. de Blok, *The Baryonic Tully-Fisher relation*, *Astrophys.J.* **533** (2000) L99–L102, [`astro-ph/0003001`].

[57] M. Milgrom, *A modification of the Newtonian dynamics as a possible alternative to the hidden mass hypothesis*, *ApJ* **270** (July, 1983) 365–370.

[58] G. Bertone, ed., *Particle Dark Matter.* Cambridge University Press, 2010.

[59] **Super-Kamiokande** Collaboration, K. Abe et al., *Search for proton decay via $p \to \nu K^+$ using 260kilotonyear data of Super-Kamiokande*, *Phys.Rev.* **D90** (2014), no. 7 072005, [`arXiv:1408.1195`].

[60] V. Kuzmin, V. Rubakov, and M. Shaposhnikov, *On the Anomalous Electroweak Baryon Number Nonconservation in the Early Universe*, *Phys.Lett.* **B155** (1985) 36.

[61] L. M. Krauss and F. Wilczek, *Discrete Gauge Symmetry in Continuum Theories*, *Phys.Rev.Lett.* **62** (1989) 1221.

[62] S. P. Martin, *A Supersymmetry primer*, *Adv.Ser.Direct.High Energy Phys.* **21** (2010) 1–153, [`hep-ph/9709356`].

[63] S. P. Martin, *Some simple criteria for gauged R-parity*, *Phys.Rev.* **D46** (1992) 2769–2772, [`hep-ph/9207218`].

[64] P. Svrcek and E. Witten, *Axions In String Theory*, *JHEP* **0606** (2006) 051, [`hep-th/0605206`].

[65] L. J. Hall, K. Jedamzik, J. March-Russell, and S. M. West, *Freeze-In Production of FIMP Dark Matter*, *JHEP* **1003** (2010) 080, [`arXiv:0911.1120`].

[66] J. M. Cline, *Baryogenesis*, `hep-ph/0609145`.

[67] M. Pospelov and A. Ritz, *Astrophysical Signatures of Secluded Dark Matter*, *Phys.Lett.* **B671** (2009) 391–397, [`arXiv:0810.1502`].

[68] J. D. March-Russell and S. M. West, *WIMPonium and Boost Factors for Indirect Dark Matter Detection*, *Phys.Lett.* **B676** (2009) 133–139, [`arXiv:0812.0559`].

[69] W. Shepherd, T. M. Tait, and G. Zaharijas, *Bound states of weakly interacting dark matter*, *Phys.Rev.* **D79** (2009) 055022, [`arXiv:0901.2125`].

[70] D. E. Kaplan, G. Z. Krnjaic, K. R. Rehermann, and C. M. Wells, *Atomic Dark Matter*, *JCAP* **1005** (2010) 021, [`arXiv:0909.0753`].

[71] J. A. Frieman, G. B. Gelmini, M. Gleiser, and E. W. Kolb, *Primordial origin of nontopological solitons*, *Phys. Rev. Lett.* **60** (May, 1988) 2101–2104.

[72] A. Kusenko and M. E. Shaposhnikov, *Supersymmetric Q balls as dark matter*, *Phys.Lett.* **B418** (1998) 46–54, [`hep-ph/9709492`].

[73] S. Nussinov, *Technocosmology: could a technibaryon excess provide a 'natural' missing mass candidate?*, *Phys.Lett.* **B165** (1985) 55.

[74] R. Chivukula and T. P. Walker, *Technicolor cosmology*, *Nucl.Phys.* **B329** (1990) 445.

[75] G. Krnjaic and K. Sigurdson, *Big Bang Darkleosynthesis*, `arXiv:1406.1171`.

[76] J. A. Frieman, A. V. Olinto, M. Gleiser, and C. Alcock, *Cosmic Evolution of Nontopological Solitons. 1.*, *Phys.Rev.* **D40** (1989) 3241.

[77] M. B. Wise and Y. Zhang, *Stable Bound States of Asymmetric Dark Matter*, *Phys.Rev.* **D90** (2014), no. 5 055030, [`arXiv:1407.4121`].

[78] M. B. Wise and Y. Zhang, *Yukawa Bound States of a Large Number of Fermions*, *JHEP* **1502** (2015) 023, [`arXiv:1411.1772`].

[79] W. Detmold, M. McCullough, and A. Pochinsky, *Dark Nuclei I: Cosmology and Indirect Detection*, *Phys.Rev.* **D90** (2014), no. 11 115013, [`arXiv:1406.2276`].

[80] W. Detmold, M. McCullough, and A. Pochinsky, *Dark nuclei. II. Nuclear spectroscopy in two-color QCD*, *Phys.Rev.* **D90** (2014), no. 11 114506, [`arXiv:1406.4116`].

[81] G. B. Gelmini, L. J. Hall, and M. J. Lin, *What is the cosmion?*, *Nucl. Phys.* **B281** (1987) 726.

[82] S. M. Barr, R. Chivukula, and E. Farhi, *Electroweak fermion number violation and the production of stable particles in the early universe*, *Phys.Lett.* **B241** (1990) 387–391.

[83] D. B. Kaplan, *A Single explanation for both the baryon and dark matter densities*, *Phys.Rev.Lett.* **68** (1992) 741–743.

[84] S. D. Thomas, *Baryons and dark matter from the late decay of a supersymmetric condensate*, *Phys.Lett.* **B356** (1995) 256–263, [`hep-ph/9506274`].

[85] D. Hooper, J. March-Russell, and S. M. West, *Asymmetric sneutrino dark matter and the Omega(b) / Omega(DM) puzzle*, *Phys.Lett.* **B605** (2005) 228–236, [`hep-ph/0410114`].

[86] R. Kitano and I. Low, *Dark matter from baryon asymmetry*, *Phys.Rev.* **D71** (2005) 023510, [`hep-ph/0411133`].

[87] K. Agashe and G. Servant, *Baryon number in warped GUTs: Model building and (dark matter related) phenomenology*, *JCAP* **0502** (2005) 002, [`hep-ph/0411254`].

[88] N. Cosme, L. Lopez Honorez, and M. H. Tytgat, *Leptogenesis and dark matter related?*, *Phys.Rev.* **D72** (2005) 043505, [`hep-ph/0506320`].

[89] G. R. Farrar and G. Zaharijas, *Dark matter and the baryon asymmetry*, *Phys.Rev.Lett.* **96** (2006) 041302, [`hep-ph/0510079`].

[90] D. Suematsu, *Nonthermal production of baryon and dark matter*, *Astropart.Phys.* **24** (2006) 511–519, [`hep-ph/0510251`].

[91] M. H. Tytgat, *Relating leptogenesis and dark matter*, `hep-ph/0606140`.

[92] T. Banks, S. Echols, and J. Jones, *Baryogenesis, dark matter and the Pentagon*, *JHEP* **0611** (2006) 046, [`hep-ph/0608104`].

[93] M. Y. Khlopov and C. Kouvaris, *Composite dark matter from a model with composite Higgs boson*, *Phys. Rev.* **D78** (2008) 065040, [`arXiv:0806.1191`].

[94] R. Kitano, H. Murayama, and M. Ratz, *Unified origin of baryons and dark matter*, *Phys.Lett.* **B669** (2008) 145–149, [`arXiv:0807.4313`].

[95] D. E. Kaplan, M. A. Luty, and K. M. Zurek, *Asymmetric Dark Matter*, *Phys.Rev.* **D79** (2009) 115016, [`arXiv:0901.4117`].

[96] K. Kohri, A. Mazumdar, N. Sahu, and P. Stephens, *Probing Unified Origin of Dark Matter and Baryon Asymmetry at PAMELA/Fermi*, *Phys. Rev.* **D80** (2009) 061302, [`arXiv:0907.0622`].

[97] G. D. Kribs, T. S. Roy, J. Terning, and K. M. Zurek, *Quirky Composite Dark Matter*, *Phys.Rev.* **D81** (2010) 095001, [`arXiv:0909.2034`].

[98] T. Cohen and K. M. Zurek, *Leptophilic Dark Matter from the Lepton Asymmetry*, *Phys.Rev.Lett.* **104** (2010) 101301, [`arXiv:0909.2035`].

[99] H. An, S.-L. Chen, R. N. Mohapatra, and Y. Zhang, *Leptogenesis as a Common Origin for Matter and Dark Matter*, *JHEP* **1003** (2010) 124, [`arXiv:0911.4463`].

[100] M. Y. Khlopov, A. G. Mayorov, and E. Y. Soldatov, *Composite Dark Matter and Puzzles of Dark Matter Searches*, *Int. J. Mod. Phys.* **D19** (2010) 1385–1395, [`arXiv:1003.1144`].

[101] T. Cohen, D. J. Phalen, A. Pierce, and K. M. Zurek, *Asymmetric Dark Matter from a GeV Hidden Sector*, *Phys.Rev.* **D82** (2010) 056001, [`arXiv:1005.1655`].

[102] J. Shelton and K. M. Zurek, *Darkogenesis: A baryon asymmetry from the dark matter sector*, *Phys.Rev.* **D82** (2010) 123512, [`arXiv:1008.1997`].

[103] H. Davoudiasl, D. E. Morrissey, K. Sigurdson, and S. Tulin, *Hylogenesis: A Unified Origin for Baryonic Visible Matter and Antibaryonic Dark Matter*, *Phys.Rev.Lett.* **105** (2010) 211304, [`arXiv:1008.2399`].

[104] N. Haba and S. Matsumoto, *Baryogenesis from Dark Sector*, *Prog.Theor.Phys.* **125** (2011) 1311–1316, [`arXiv:1008.2487`].

[105] M. R. Buckley and L. Randall, *Xogenesis*, *JHEP* **1109** (2011) 009, [`arXiv:1009.0270`].

[106] L. J. Hall, J. March-Russell, and S. M. West, *A Unified Theory of Matter Genesis: Asymmetric Freeze-In*, `arXiv:1010.0245`.

[107] B. Dutta and J. Kumar, *Asymmetric Dark Matter from Hidden Sector Baryogenesis*, *Phys.Lett.* **B699** (2011) 364–367, [`arXiv:1012.1341`].

[108] A. Falkowski, J. T. Ruderman, and T. Volansky, *Asymmetric Dark Matter from Leptogenesis*, *JHEP* **1105** (2011) 106, [`arXiv:1101.4936`].

[109] M. T. Frandsen, S. Sarkar, and K. Schmidt-Hoberg, *Light asymmetric dark matter from new strong dynamics*, *Phys.Rev.* **D84** (2011) 051703, [`arXiv:1103.4350`].

[110] M. L. Graesser, I. M. Shoemaker, and L. Vecchi, *Asymmetric WIMP dark matter*, *JHEP* **1110** (2011) 110, [`arXiv:1103.2771`].

[111] M. R. Buckley, *Asymmetric Dark Matter and Effective Operators*, *Phys.Rev.* **D84** (2011) 043510, [`arXiv:1104.1429`].

[112] H. Iminniyaz, M. Drees, and X. Chen, *Relic Abundance of Asymmetric Dark Matter*, *JCAP* **1107** (2011) 003, [`arXiv:1104.5548`].

[113] J. March-Russell and M. McCullough, *Asymmetric Dark Matter via Spontaneous Co-Genesis*, *JCAP* **1203** (2012) 019, [`arXiv:1106.4319`].

[114] J. March-Russell, J. Unwin, and S. M. West, *Closing in on Asymmetric Dark Matter I: Model independent limits for interactions with quarks*, *JHEP* **1208** (2012) 029, [`arXiv:1203.4854`].

[115] E. Hardy, R. Lasenby, and J. Unwin, *Annihilation Signals from Asymmetric Dark Matter*, *JHEP* **1407** (2014) 049, [`arXiv:1402.4500`].

[116] J. Unwin, *Towards cogenesis via Asymmetric Freeze-In: The χ who came-in from the cold*, *JHEP* **1410** (2014) 190, [`arXiv:1406.3027`].

[117] K. Griest and M. Kamionkowski, *Unitarity Limits on the Mass and Radius of Dark Matter Particles*, *Phys.Rev.Lett.* **64** (1990) 615.

[118] L. J. Hall, K. Jedamzik, J. March-Russell, and S. M. West, *Freeze-In Production of FIMP Dark Matter*, *JHEP* **03** (2010) 080, [`arXiv:0911.1120`].

[119] C. Bertulani, *Nuclear Physics in a Nutshell.* In a Nutshell. Princeton University Press, 2007.

[120] T. Multamaki and I. Vilja, *Q Ball collisions in the MSSM: Gravity mediated supersymmetry breaking*, *Phys.Lett.* **B482** (2000) 161–166, [`hep-ph/0003270`].

[121] V. F. Mukhanov, *Nucleosynthesis without a computer*, *Int.J.Theor.Phys.* **43** (2004) 669–693, [`astro-ph/0303073`].

[122] F. Leyvraz, *Rigorous results in the scaling theory of irreversible aggregation kinetics*, *ArXiv Mathematical Physics e-prints* (Feb., 2006) [`math-ph/0602007`].

[123] P. L. Krapivsky, S. Redner, and E. Ben-Naim, *A Kinetic View of Statistical Physics.* Cambridge University Press, Dec., 2010.

[124] P. van Dongen and M. Ernst, *Scaling solutions of smoluchowski's coagulation equation*, *Journal of Statistical Physics* **50** (1988), no. 1-2 295–329.

[125] A. Loeb and N. Weiner, *Cores in Dwarf Galaxies from Dark Matter with a Yukawa Potential*, *Phys.Rev.Lett.* **106** (2011) 171302, [`arXiv:1011.6374`].

[126] K. Schutz and T. R. Slatyer, *Self-Scattering for Dark Matter with an Excited State*, *JCAP* **1501** (2015), no. 01 021, [`arXiv:1409.2867`].

[127] R. Essig, E. Kuflik, S. D. McDermott, T. Volansky, and K. M. Zurek, *Constraining Light Dark Matter with Diffuse X-Ray and Gamma-Ray Observations*, *JHEP* **1311** (2013) 193, [`arXiv:1309.4091`].

[128] K. Jedamzik and M. Pospelov, *Big Bang Nucleosynthesis and Particle Dark Matter*, *New J.Phys.* **11** (2009) 105028, [`arXiv:0906.2087`].

[129] M. S. Madhavacheril, N. Sehgal, and T. R. Slatyer, *Current Dark Matter Annihilation Constraints from CMB and Low-Redshift Data*, *Phys.Rev.* **D89** (2014) 103508, [`arXiv:1310.3815`].

[130] M. Cirelli, *Indirect Searches for Dark Matter: a status review*, *Pramana* **79** (2012) 1021–1043, [`arXiv:1202.1454`].

[131] V. Simha and G. Steigman, *Constraining The Early-Universe Baryon Density And Expansion Rate*, *JCAP* **0806** (2008) 016, [`arXiv:0803.3465`].

[132] K. Jedamzik, *Big bang nucleosynthesis constraints on hadronically and electromagnetically decaying relic neutral particles*, *Phys.Rev.* **D74** (2006) 103509, [`hep-ph/0604251`].

[133] W. Hu and J. Silk, *Thermalization constraints and spectral distortions for massive unstable relic particles*, *Phys.Rev.Lett.* **70** (1993) 2661–2664.

[134] T. R. Slatyer, *Energy Injection And Absorption In The Cosmic Dark Ages*, *Phys.Rev.* **D87** (2013), no. 12 123513, [`arXiv:1211.0283`].

[135] **BaBar** Collaboration, J. Lees et al., *Search for a Dark Photon in e^+e^- Collisions at BaBar*, *Phys.Rev.Lett.* **113** (2014), no. 20 201801, [`arXiv:1406.2980`].

[136] G. G. Raffelt, *Astrophysical axion bounds*, *Lect.Notes Phys.* **741** (2008) 51–71, [`hep-ph/0611350`].

[137] D. Kazanas, R. N. Mohapatra, S. Nussinov, V. L. Teplitz, and Y. Zhang, *Supernova Bounds on the Dark Photon Using its Electromagnetic Decay*, *Nucl.Phys.* **B890** (2014) 17–29, [`arXiv:1410.0221`].

[138] **Planck Collaboration** Collaboration, P. Ade et al., *Planck 2013 results. XVI. Cosmological parameters*, *Astron.Astrophys.* (2014) [`arXiv:1303.5076`].

[139] K. Hashimoto and T. Morita, *Nucleus from String Theory*, *Phys.Rev.* **D84** (2011) 046004, [`arXiv:1103.5688`].

[140] E. Hardy, R. Lasenby, J. March-Russell, and S. M. West, *Big Bang Synthesis of Nuclear Dark Matter*, `arXiv:1411.3739`.

[141] G. Gelmini, A. Kusenko, and S. Nussinov, *Experimental identification of nonpointlike dark matter candidates*, *Phys.Rev.Lett.* **89** (2002) 101302, [`hep-ph/0203179`].

[142] S. Chang, A. Pierce, and N. Weiner, *Momentum Dependent Dark Matter Scattering*, *JCAP* **1001** (2010) 006, [`arXiv:0908.3192`].

[143] B. Feldstein, A. L. Fitzpatrick, and E. Katz, *Form Factor Dark Matter*, *JCAP* **1001** (2010) 020, [`arXiv:0908.2991`].

[144] S. D. McDermott, H.-B. Yu, and K. M. Zurek, *The Dark Matter Inverse Problem: Extracting Particle Physics from Scattering Events*, *Phys.Rev.* **D85** (2012) 123507, [`arXiv:1110.4281`].

[145] J. F. Cherry, M. T. Frandsen, and I. M. Shoemaker, *Halo Independent Direct Detection of Momentum-Dependent Dark Matter*, *JCAP* **1410** (2014), no. 10 022, [`arXiv:1405.1420`].

[146] A. L. Fitzpatrick, W. Haxton, E. Katz, N. Lubbers, and Y. Xu, *The Effective Field Theory of Dark Matter Direct Detection*, *JCAP* **1302** (2013) 004, [`arXiv:1203.3542`].

[147] G. Duda, A. Kemper, and P. Gondolo, *Model Independent Form Factors for Spin Independent Neutralino-Nucleon Scattering from Elastic Electron Scattering Data*, *JCAP* **0704** (2007) 012, [`hep-ph/0608035`].

[148] C. McCabe, *The Astrophysical Uncertainties Of Dark Matter Direct Detection Experiments*, *Phys.Rev.* **D82** (2010) 023530, [`arXiv:1005.0579`].

[149] A. Djouadi, O. Lebedev, Y. Mambrini, and J. Quevillon, *Implications of LHC searches for Higgs–portal dark matter*, *Phys.Lett.* **B709** (2012) 65–69, [`arXiv:1112.3299`].

[150] M. Kuhlen, N. Weiner, J. Diemand, P. Madau, B. Moore, D. Potter, J. Stadel, and M. Zemp, *Dark matter direct detection with non-Maxwellian velocity structure*, *JCAP* **2** (Feb., 2010) 30, [`arXiv:0912.2358`].

[151] J. I. Read, L. Mayer, A. M. Brooks, F. Governato, and G. Lake, *A dark matter disc in three cosmological simulations of Milky Way mass galaxies*, *MNRAS* **397** (July, 2009) 44–51, [`arXiv:0902.0009`].

[152] J. Diemand, M. Kuhlen, P. Madau, M. Zemp, B. Moore, et al., *Clumps and streams in the local dark matter distribution*, *Nature* **454** (2008) 735–738, [`arXiv:0805.1244`].

[153] P. J. Fox, G. D. Kribs, and T. M. Tait, *Interpreting Dark Matter Direct Detection Independently of the Local Velocity and Density Distribution*, *Phys.Rev.* **D83** (2011) 034007, [`arXiv:1011.1910`].

[154] P. J. Fox, J. Liu, and N. Weiner, *Integrating Out Astrophysical Uncertainties*, *Phys.Rev.* **D83** (2011) 103514, [`arXiv:1011.1915`].

[155] P. J. Fox, G. D. Kribs, and T. M. Tait, *Interpreting Dark Matter Direct Detection Independently of the Local Velocity and Density Distribution*, *Phys.Rev.* **D83** (2011) 034007, [`arXiv:1011.1910`].

[156] N. Bozorgnia, J. Herrero-Garcia, T. Schwetz, and J. Zupan, *Halo-independent methods for inelastic dark matter scattering*, *JCAP* **1307** (2013) 049, [`arXiv:1305.3575`].

[157] E. Del Nobile, G. Gelmini, P. Gondolo, and J.-H. Huh, *Generalized Halo Independent Comparison of Direct Dark Matter Detection Data*, *JCAP* **1310** (2013) 048, [`arXiv:1306.5273`].

[158] S. Scopel and K. Yoon, *A systematic halo-independent analysis of direct detection data within the framework of Inelastic Dark Matter*, *JCAP* **1408** (2014) 060, [`arXiv:1405.0364`].

[159] A. Bohr and B. Mottelson, *Nuclear Structure.* No. v. 1 in Nuclear Structure. World Scientific, 1998.

[160] S. R. Coleman, *Q Balls*, *Nucl.Phys.* **B262** (1985) 263.

[161] L. J. Tassie, *Scattering of Alpha-Particles by a Vibrational Nucleus*, *Australian Journal of Physics* **15** (June, 1962) 135.

[162] C. Mahaux, P. Bortignon, R. Broglia, and C. Dasso, *Dynamics of the shell model*, *Phys.Rept.* **120** (1985) 1–274.

[163] K. M. Zurek, *Asymmetric Dark Matter: Theories, Signatures, and Constraints*, *Phys.Rept.* **537** (2014) 91–121, [`arXiv:1308.0338`].

[164] C. Kouvaris, *Limits on self-interacting dark matter from neutron stars*, *Phys. Rev. Lett.* **108** (May, 2012) 191301.

[165] A. R. Zentner, *High-Energy Neutrinos From Dark Matter Particle Self-Capture Within the Sun*, *Phys.Rev.* **D80** (2009) 063501, [`arXiv:0907.3448`].

[166] M. Taoso, F. Iocco, G. Meynet, G. Bertone, and P. Eggenberger, *Effect of low mass dark matter particles on the Sun*, *Phys.Rev.* **D87** (Oct., 2010) 083509, [`arXiv:1005.5711`].

[167] B. Bertoni, A. E. Nelson, and S. Reddy, *Dark Matter Thermalization in Neutron Stars*, *Phys.Rev.* **D88** (2013) 123505, [`arXiv:1309.1721`].

[168] A. H. Peter, C. E. Moody, and M. Kamionkowski, *Dark-Matter Decays and Self-Gravitating Halos*, *Phys.Rev.* **D81** (2010) 103501, [`arXiv:1003.0419`].

[169] J. Binney and S. Tremaine, *Galactic Dynamics: (Second Edition).* Princeton Series in Astrophysics. Princeton University Press, 2008.

[170] C. Boehm, T. Delahaye, and J. Silk, *Can the morphology of gamma-ray emission distinguish annihilating from decaying dark matter?*, *Phys.Rev.Lett.* **105** (2010) 221301, [`arXiv:1003.1225`].

[171] W. Buchmuller and M. Garny, *Decaying vs Annihilating Dark Matter in Light of a Tentative Gamma-Ray Line*, *JCAP* **1208** (2012) 035, [`arXiv:1206.7056`].

[172] Y. Zhao and K. M. Zurek, *Indirect Detection Signatures for the Origin of Asymmetric Dark Matter*, *JHEP* **1407** (2014) 017, [`arXiv:1401.7664`].

[173] M. R. Buckley and S. Profumo, *Regenerating a Symmetry in Asymmetric Dark Matter*, *Phys.Rev.Lett.* **108** (2012) 011301, [`arXiv:1109.2164`].

[174] M. Cirelli, P. Panci, G. Servant, and G. Zaharijas, *Consequences of DM/antiDM Oscillations for Asymmetric WIMP Dark Matter*, *JCAP* **1203** (2012) 015, [`arXiv:1110.3809`].

[175] S. Tulin, H.-B. Yu, and K. M. Zurek, *Oscillating Asymmetric Dark Matter*, *JCAP* **1205** (2012) 013, [`arXiv:1202.0283`].

[176] N. Okada and O. Seto, *Originally Asymmetric Dark Matter*, *Phys.Rev.* **D86** (2012) 063525, [`arXiv:1205.2844`].

[177] F. D'Eramo, L. Fei, and J. Thaler, *Dark Matter Assimilation into the Baryon Asymmetry*, *JCAP* **1203** (2012) 010, [`arXiv:1111.5615`].

[178] J. Unwin, *Exodus: Hidden origin of dark matter and baryons*, *JHEP* **1306** (2013) 090, [`arXiv:1212.1425`].

[179] P. J. Fox, R. Harnik, J. Kopp, and Y. Tsai, *LEP Shines Light on Dark Matter*, *Phys.Rev.* **D84** (2011) 014028, [`arXiv:1103.0240`].

[180] R. Cotta, J. Hewett, M. Le, and T. Rizzo, *Bounds on Dark Matter Interactions with Electroweak Gauge Bosons*, *Phys.Rev.* **D88** (2013) 116009, [`arXiv:1210.0525`].

[181] I. M. Shoemaker, *Constraints on Dark Matter Protohalos in Effective Theories and Neutrinophilic Dark Matter*, *Phys.Dark Univ.* **2** (2013), no. 3 157–162, [`arXiv:1305.1936`].

[182] D. P. Finkbeiner, S. Galli, T. Lin, and T. R. Slatyer, *Searching for Dark Matter in the CMB: A Compact Parameterization of Energy Injection from New Physics*, *Phys.Rev.* **D85** (2012) 043522, [`arXiv:1109.6322`].

[183] X.-L. Chen and M. Kamionkowski, *Particle decays during the cosmic dark ages*, *Phys.Rev.* **D70** (2004) 043502, [`astro-ph/0310473`].

[184] M. Kamionkowski and A. Kosowsky, *The Cosmic microwave background and particle physics*, *Ann.Rev.Nucl.Part.Sci.* **49** (1999) 77–123, [`astro-ph/9904108`].

[185] P. Nath and P. Fileviez Perez, *Proton stability in grand unified theories, in strings and in branes*, *Phys.Rept.* **441** (2007) 191–317, [`hep-ph/0601023`].

[186] **LAT collaboration** Collaboration, M. Ackermann et al., *Constraints on the Galactic Halo Dark Matter from Fermi-LAT Diffuse Measurements*, *Astrophys.J.* **761** (2012) 91, [`arXiv:1205.6474`].

[187] S. Tulin, H.-B. Yu, and K. M. Zurek, *Beyond Collisionless Dark Matter: Particle Physics Dynamics for Dark Matter Halo Structure*, *Phys.Rev.* **D87** (2013), no. 11 115007, [`arXiv:1302.3898`].

[188] J. L. Feng, M. Kaplinghat, and H.-B. Yu, *Halo Shape and Relic Density Exclusions of Sommerfeld-Enhanced Dark Matter Explanations of Cosmic Ray Excesses*, *Phys.Rev.Lett.* **104** (2010) 151301, [`arXiv:0911.0422`].

[189] T. Lin, H.-B. Yu, and K. M. Zurek, *On Symmetric and Asymmetric Light Dark Matter*, *Phys.Rev.* **D85** (2012) 063503, [`arXiv:1111.0293`].

[190] M. Kaplinghat, R. E. Keeley, T. Linden, and H.-B. Yu, *Tying Dark Matter to Baryons with Self-interactions*, *Phys.Rev.Lett.* **113** (2014) 021302, [`arXiv:1311.6524`].

[191] N. F. Bell, A. J. Galea, and K. Petraki, *Lifetime Constraints for Late Dark Matter Decay*, *Phys.Rev.* **D82** (2010) 023514, [`arXiv:1004.1008`].

[192] I. F. Albuquerque, C. Prez de Los Heros, and D. S. Robertson, *Constraints on self interacting dark matter from IceCube results*, *JCAP* **1402** (2014) 047, [`arXiv:1312.0797`].

[193] N. Fornengo, L. Maccione, and A. Vittino, *Constraints on particle dark matter from cosmic-ray antiprotons*, *JCAP* **1404** (2014) 003, [`arXiv:1312.3579`].

[194] C. Evoli, I. Cholis, D. Grasso, L. Maccione, and P. Ullio, *Antiprotons from dark matter annihilation in the Galaxy: astrophysical uncertainties*, *Phys.Rev.* **D85** (2012) 123511, [`arXiv:1108.0664`].

[195] L. Bergstrom, T. Bringmann, I. Cholis, D. Hooper, and C. Weniger, *New limits on dark matter annihilation from AMS cosmic ray positron data*, *Phys.Rev.Lett.* **111** (2013) 171101, [`arXiv:1306.3983`].

[196] F. Donato, N. Fornengo, D. Maurin, and P. Salati, *Antiprotons in cosmic rays from neutralino annihilation*, *Phys. Rev.* **D69** (2004) 063501, [`astro-ph/0306207`].

[197] R. Essig, A. Manalaysay, J. Mardon, P. Sorensen, and T. Volansky, *First Direct Detection Limits on sub-GeV Dark Matter from XENON10*, *Phys. Rev. Lett.* **109** (2012) 021301, [`arXiv:1206.2644`].

[198] K. Petraki and R. R. Volkas, *Review of asymmetric dark matter*, *Int.J.Mod.Phys.* **A28** (2013) 1330028, [`arXiv:1305.4939`].

[199] H. Davoudiasl and R. N. Mohapatra, *On Relating the Genesis of Cosmic Baryons and Dark Matter*, *New J.Phys.* **14** (2012) 095011, [`arXiv:1203.1247`].

[200] M. Pospelov, A. Ritz, and M. B. Voloshin, *Secluded WIMP Dark Matter*, *Phys.Lett.* **B662** (2008) 53–61, [`arXiv:0711.4866`].

[201] I. Z. Rothstein, T. Schwetz, and J. Zupan, *Phenomenology of Dark Matter annihilation into a long-lived intermediate state*, *JCAP* **0907** (2009) 018, [`arXiv:0903.3116`].

[202] J. Mardon, Y. Nomura, D. Stolarski, and J. Thaler, *Dark Matter Signals from Cascade Annihilations*, *JCAP* **0905** (2009) 016, [`arXiv:0901.2926`].

[203] D. N. Spergel and P. J. Steinhardt, *Observational evidence for selfinteracting cold dark matter*, *Phys.Rev.Lett.* **84** (2000) 3760–3763, [`astro-ph/9909386`].

[204] G. Blanger, A. Goudelis, J.-C. Park, and A. Pukhov, *Isospin-violating dark matter from a double portal*, *JCAP* **1402** (2014) 020, [`arXiv:1311.0022`].

[205] E. Del Nobile, G. B. Gelmini, P. Gondolo, and J.-H. Huh, *Update on Light WIMP Limits: LUX, lite and Light*, *JCAP* **1403** (2014) 014, [`arXiv:1311.4247`].

[206] P. J. Fox, G. Jung, P. Sorensen, and N. Weiner, *Dark matter in light of the LUX results*, *Phys.Rev.* **D89** (2014), no. 10 103526, [`arXiv:1401.0216`].

[207] M. I. Gresham and K. M. Zurek, *Light Dark Matter Anomalies After LUX*, *Phys.Rev.* **D89** (2014), no. 1 016017, [`arXiv:1311.2082`].

[208] G. Belanger, F. Boudjema, A. Pukhov, and A. Semenov, *MicrOMEGAs: A Program for calculating the relic density in the MSSM*, *Comput.Phys.Commun.* **149** (2002) 103–120, [`hep-ph/0112278`].

[209] D. Hooper and T. R. Slatyer, *Two Emission Mechanisms in the Fermi Bubbles: A Possible Signal of Annihilating Dark Matter*, *Phys.Dark Univ.* **2** (2013) 118–138, [`arXiv:1302.6589`].

[210] D. Hooper, I. Cholis, T. Linden, J. Siegal-Gaskins, and T. Slatyer, *Pulsars Cannot Account for the Inner Galaxy's GeV Excess*, *Phys.Rev.* **D88** (2013) 083009, [`arXiv:1305.0830`].

[211] K. N. Abazajian and M. Kaplinghat, *Detection of a Gamma-Ray Source in the Galactic Center Consistent with Extended Emission from Dark Matter Annihilation and Concentrated Astrophysical Emission*, *Phys.Rev.* **D86** (2012) 083511, [`arXiv:1207.6047`].

[212] D. Hooper and T. Linden, *On The Origin Of The Gamma Rays From The Galactic Center*, *Phys.Rev.* **D84** (2011) 123005, [`arXiv:1110.0006`].

[213] D. Hooper and L. Goodenough, *Dark Matter Annihilation in The Galactic Center As Seen by the Fermi Gamma Ray Space Telescope*, *Phys.Lett.* **B697** (2011) 412–428, [`arXiv:1010.2752`].

[214] K. N. Abazajian, N. Canac, S. Horiuchi, and M. Kaplinghat, *Astrophysical and Dark Matter Interpretations of Extended Gamma-Ray Emission from the Galactic Center*, *Phys.Rev.* **D90** (2014), no. 2 023526, [`arXiv:1402.4090`].

[215] C. Gordon and O. Macias, *Dark Matter and Pulsar Model Constraints from Galactic Center Fermi-LAT Gamma Ray Observations*, *Phys.Rev.* **D88** (2013), no. 8 083521, [`arXiv:1306.5725`].

[216] W. Dehnen and A. King, *Probing dark matter with x-ray binaries*, *Mon.Not.Roy.Astron.Soc.Lett.* **367** (2006) L29–L31, [`astro-ph/0512106`].

[217] M. G. Walker, M. Mateo, E. W. Olszewski, O. Y. Gnedin, X. Wang, et al., *Velocity Dispersion Profiles of Seven Dwarf Spheroidal Galaxies*, *Astrophys.J.* **667** (2007) L53, [`arXiv:0708.0010`].

[218] A. Charbonnier, C. Combet, M. Daniel, S. Funk, J. Hinton, et al., *Dark matter profiles and annihilation in dwarf spheroidal galaxies: prospectives for present and future gamma-ray observatories - I. The classical dSphs*, *Mon.Not.Roy.Astron.Soc.* **418** (2011) 1526–1556, [`arXiv:1104.0412`].

[219] **Fermi-LAT, DES** Collaboration, A. Drlica-Wagner et al., *Search for Gamma-Ray Emission from DES Dwarf Spheroidal Galaxy Candidates with Fermi-LAT Data*, *Astrophys.J.* (2015) [`arXiv:1503.02632`].

[220] **Fermi-LAT** Collaboration, M. Ackermann et al., *Searching for Dark Matter Annihilation from Milky Way Dwarf Spheroidal Galaxies with Six Years of Fermi-LAT Data*, `arXiv:1503.02641`.

[221] D. Hooper and T. Linden, *On The Gamma-Ray Emission From Reticulum II and Other Dwarf Galaxies*, `arXiv:1503.06209`.

[222] C. Boehm, M. J. Dolan, C. McCabe, M. Spannowsky, and C. J. Wallace, *Extended gamma-ray emission from Coy Dark Matter*, *JCAP* **1405** (2014) 009, [`arXiv:1401.6458`].

[223] **CDMS Collaboration** Collaboration, R. Agnese et al., *Silicon Detector Dark Matter Results from the Final Exposure of CDMS II*, *Phys.Rev.Lett.* **111** (2013), no. 25 251301, [`arXiv:1304.4279`].

[224] **CoGeNT collaboration** Collaboration, C. Aalseth et al., *Results from a Search for Light-Mass Dark Matter with a P-type Point Contact Germanium Detector*, *Phys.Rev.Lett.* **106** (2011) 131301, [`arXiv:1002.4703`].

[225] T. Cohen, J. Kearney, A. Pierce, and D. Tucker-Smith, *Singlet-Doublet Dark Matter*, *Phys.Rev.* **D85** (2012) 075003, [`arXiv:1109.2604`].

[226] N. Arkani-Hamed, A. Delgado, and G. Giudice, *The Well-tempered neutralino*, *Nucl.Phys.* **B741** (2006) 108–130, [`hep-ph/0601041`].

[227] P. Grothaus, M. Fairbairn, and J. Monroe, *Directional Dark Matter Detection Beyond the Neutrino Bound*, *Phys.Rev.* **D90** (2014), no. 5 055018, [`arXiv:1406.5047`].

[228] P. Cushman, C. Galbiati, D. McKinsey, H. Robertson, T. Tait, et al., *Working Group Report: WIMP Dark Matter Direct Detection*, `arXiv:1310.8327`.

[229] **LUX** Collaboration, D. Akerib et al., *First results from the LUX dark matter experiment at the Sanford Underground Research Facility*, *Phys.Rev.Lett.* **112** (2014) 091303, [`arXiv:1310.8214`].

[230] M. Zaldarriaga, L. Colombo, E. Komatsu, A. Lidz, M. Mortonson, et al., *CMBPol Mission Concept Study: Reionization Science with the Cosmic Microwave Background*, `arXiv:0811.3918`.

[231] M. Cirelli and G. Giesen, *Antiprotons from Dark Matter: Current constraints and future sensitivities*, *JCAP* **1304** (2013) 015, [`arXiv:1301.7079`].

[232] **IceCube** Collaboration, M. Aartsen et al., *First observation of PeV-energy neutrinos with IceCube*, *Phys.Rev.Lett.* **111** (2013) 021103, [`arXiv:1304.5356`].

[233] **IceCube** Collaboration, A. Kappes, *Exploring the Universe with Very High Energy Neutrinos*, `arXiv:1501.07798`.

[234] **IceCube** Collaboration, M. Aartsen et al., *IceCube-Gen2: A Vision for the Future of Neutrino Astronomy in Antarctica*, `arXiv:1412.5106`.

[235] **IceCube** Collaboration, M. Aartsen et al., *Multipole analysis of IceCube data to search for dark matter accumulated in the Galactic halo*, *Eur.Phys.J.* **C75** (2015), no. 1 20, [`arXiv:1406.6868`].

[236] G. Busoni, A. De Simone, T. Jacques, E. Morgante, and A. Riotto, *Making the Most of the Relic Density for Dark Matter Searches at the LHC 14 TeV Run*, *JCAP* **1503** (2015), no. 03 022, [`arXiv:1410.7409`].

[237] R. Essig, J. A. Jaros, W. Wester, P. H. Adrian, S. Andreas, et al., *Working Group Report: New Light Weakly Coupled Particles*, `arXiv:1311.0029`.

[238] A. Gould, *Resonant Enhancements in WIMP Capture by the Earth*, *Astrophys.J.* **321** (1987) 571.

[239] A. Gould, *Cosmological density of WIMPs from solar and terrestrial annihilations*, *Astrophys.J.* **388** (1992) 338–344.

[240] J. N. Bahcall, A. M. Serenelli, and S. Basu, *New solar opacities, abundances, helioseismology, and neutrino fluxes*, *Astrophys.J.* **621** (2005) L85–L88, [`astro-ph/0412440`].

[241] **LUX Collaboration** Collaboration, D. Akerib et al., *First results from the LUX dark matter experiment at the Sanford Underground Research Facility*, *Phys.Rev.Lett.* **112** (2014) 091303, [`arXiv:1310.8214`].

[242] K. Griest and D. Seckel, *Cosmic Asymmetry, Neutrinos and the Sun*, *Nucl.Phys.* **B283** (1987) 681.

[243] A. H. G. Peter, *Dark matter in the Solar System. II. WIMP annihilation rates in the Sun*, *Phys. Rev. D* **79** (May, 2009) 103532.

[244] E. Hayashi, J. Navarro, and V. Springel, *The Shape of the Gravitational Potential in Cold Dark Matter Halos*, *Mon.Not.Roy.Astron.Soc.* **377** (2007) 50–62, [`astro-ph/0612327`].

[245] E. van Uitert, H. Hoekstra, T. Schrabback, D. G. Gilbank, M. D. Gladders, et al., *Constraints on the shapes of galaxy dark matter haloes from weak gravitational lensing*, *Astron.Astrophys.* **545** (2012) A71, [`arXiv:1206.4304`].

[246] P. Bett, V. Eke, C. S. Frenk, A. Jenkins, and T. Okamoto, *The angular momentum of cold dark matter haloes with and without baryons*, *Mon.Not.Roy.Astron.Soc.* **404** (2010) 1137, [`arXiv:0906.2785`].

[247] P. Gondolo and G. Gelmini, *Cosmic abundances of stable particles: Improved analysis*, *Nucl.Phys.* **B360** (1991) 145–179.

[248] D. Tucker-Smith and N. Weiner, *Inelastic dark matter*, *Phys.Rev.* **D64** (2001) 043502, [`hep-ph/0101138`].

[249] D. P. Finkbeiner and N. Weiner, *Exciting Dark Matter and the INTEGRAL/SPI 511 keV signal*, *Phys.Rev.* **D76** (2007) 083519, [`astro-ph/0702587`].